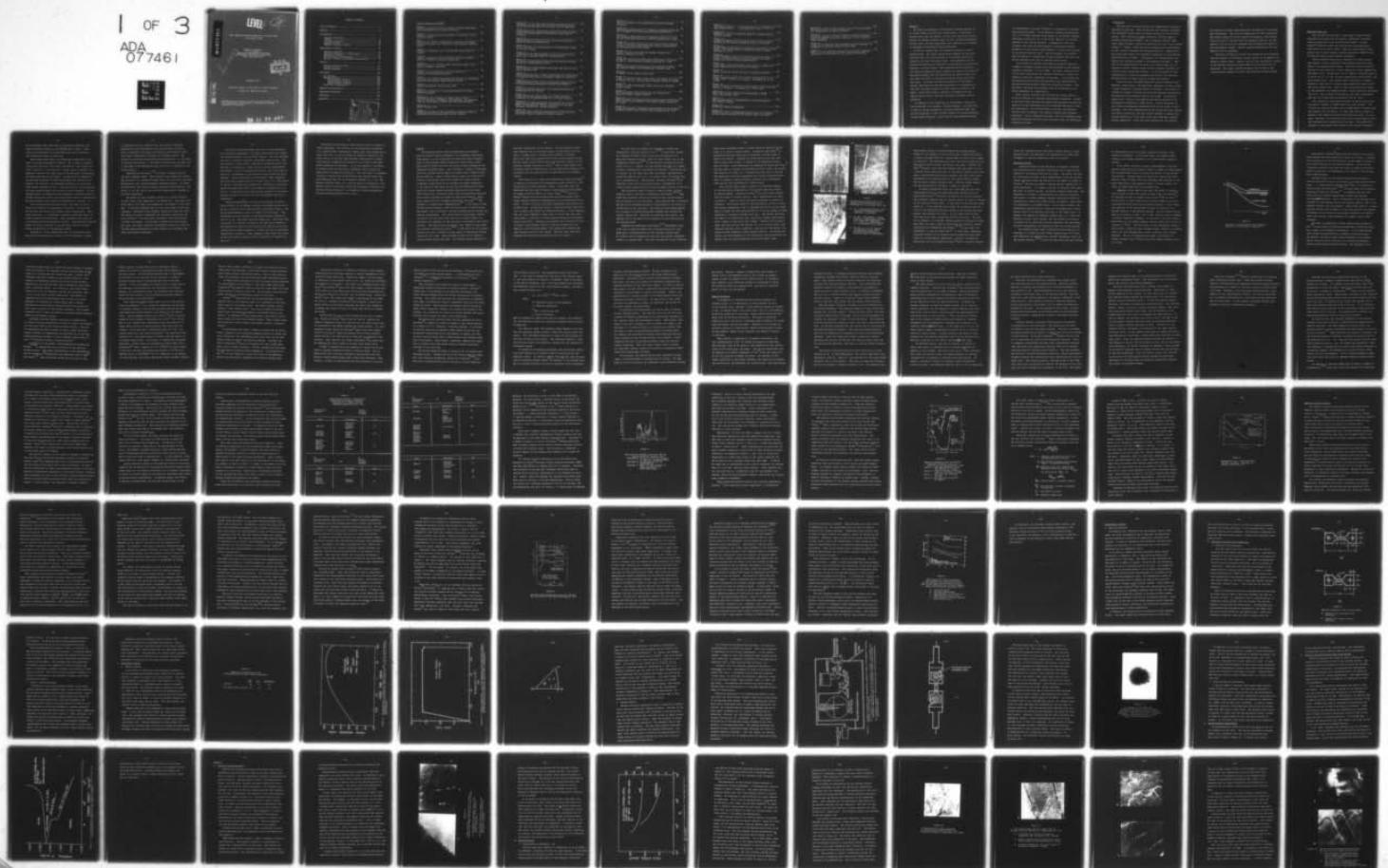


AD-A077 461 RENSSELAER POLYTECHNIC INST TROY N Y DEPT OF MATERIAL--ETC F/G 11/6  
THE CORROSION FATIGUE BEHAVIOR OF A HIGH PURITY AL-ZN-MG-CU ALLOY--ETC(U)  
NOV 79 E F SMITH, D J DUQUETTE  
N00014-75-C-0466

UNCLASSIFIED

NL

1 OF 3  
ADA  
077461



AD A 077461

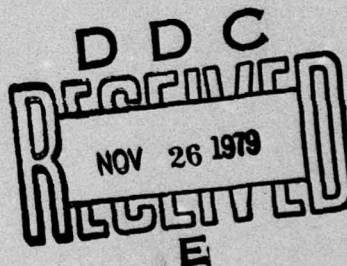
LEVEL

12

THE CORROSION FATIGUE BEHAVIOR OF A HIGH PURITY  
Al-Zn-Mg-Cu ALLOY

Edward F. Smith III  
D. J. Duquette  
Materials Engineering Department  
Rensselaer Polytechnic Institute  
Troy, New York 12181

See 1473



November 1979

DDC FILE COPY

Technical Report to the Office of Naval Research  
Project No. N00014-75-C-0466

Reproduction in whole or in part for any purpose of the  
U.S. Government is permitted. Distribution of this  
document is unlimited.

79 11 26 087

TABLE OF CONTENTS

List of Figures .....	i
Abstract .....	vi
Introduction .....	1
Physical Metallurgy .....	3
Fatigue .....	8
Corrosion Fatigue .....	14
Aqueous Fatigue .....	25
Aqueous Corrosion Fatigue .....	44
Experimental Program .....	56
Material Selection .....	56
Specimen Fabrication & Preparation .....	57
Mechanical Testing .....	60
Electrochemical Measurements .....	69
Optical & Electron Microscopy Observations .....	70
Results .....	73
Material Characterization .....	73
Fatigue Testing .....	76
Stress Relaxation .....	116
Discussion .....	126
Air Fatigue .....	129
Aqueous Fatigue .....	145
Intergranular Failure .....	149
Transgranular Cracking .....	153
Single Crystal Failures .....	173
Yield Point Experiments .....	180
Summary and Conclusions .....	184
Suggested Experiments .....	186
References .....	188
Appendix .....	193

Accession For	NTIS Grav&I
	DDC TAB
	Unannounced
Justification	
By	
Distribution/	
Availability Codes	
Dist	Avail and/or special

A

List of Figures and Tables

Figure 1 .....	12
Dislocation structure of air fatigued Al-5Zn-2.5Mg alloy as a percentage of its fatigue life ( $N_i$ )	
Figure 2 .....	16
Schematic illustration of the effect of corrosion in the fatigue response	
Table I .....	35
Relationship between intergranular corrosion and stress corrosion cracking for a number of high strength aluminum alloys	
Figure 3 .....	37
Evolution of hydrogen for an Al-7Zn-3Mg alloy pulled to failure	
Figure 4 .....	40
Hydrogen permeation rate and stress corrosion cracking rates as a function of applied potential	
Figure 5 .....	43
Susceptibility of 7075-T6 to SCC failures in mode I and mode III loading conditions	
Figure 6 .....	50
Fatigue crack propagation rates for 7075-T6 as a function of the applied potential	
Figure 7 .....	54
S/N curves for 7075-T6 aluminum illustrating the reversible nature of the hydrogen embrittlement process	
Figure 8 .....	58
Specimen geometries used in this study	
Table II .....	61
Mechanical properties of the polycrystalline T-6 heat treated specimens	
Figure 9 .....	62
The hardness as a function of aging time at 120°C. Prior to the aging treatment, the specimens were solution- ized for three hours at 465°C and cold water quenched	
Figure 10 .....	63
Single crystal data	
Figure 11 .....	66
Schematic diagrams of the experimental apparatus used in environmental testing portions of this program	

Figure 12 .....	68
An example of the Laue Back Reflection patterns used to orient the tensile axis of the single crystal specimens	
Figure 13 .....	71
An electrochemical polarization diagram for the Al-5.0Zn-2.5Mg-1.5Cu alloy tested in 3% NaCl at a scan rate of 300 mv/hr	
Figure 14 .....	75
TEM micrographs illustrating the initial metallurgical state of the heat treated alloy	
Figure 15 .....	77
The S-N behavior of polycrystalline, T-6 specimens tested in air and .5M NaCl	
Figure 16 .....	80
A characteristic SEM micrograph of the fracture surface taken from a specimen tested in laboratory air	
Figure 17 .....	81
Two stage carbon replicas taken from the fatigue fracture surface of a laboratory air test	
Figure 18 .....	83
The dislocation substructures found near the tip of an air tested fatigue crack	
Figure 19 .....	85
A TEM micrograph from a strain cycled specimen illustrating two adjacent slip bands in different stages of formation	
Figure 20 .....	86
A TEM micrograph from a strain controlled specimen illustrating the various methods of dipole loop formation	
Figure 21 .....	87
A cyclic hardening curve for a T-6 specimen fatigued in laboratory air at $.5\% \pm .25\%$	
Figure 22 .....	89
A SEM fractograph illustrating the overall fracture morphology of a specimen tested in a .5N NaCl solution	
Figure 23 .....	91
Characteristic SEM micrographs illustrating the various modes of transgranular failure encountered in the free corrosion failures in .5N NaCl solution	
Figure 24 .....	93
Two stage carbon replicas characteristic of the fracture morphology found in aqueous corrosion fatigue	

Figure 25 .....	94
The S-N response of the cathodically polarized fatigue specimens	
Figure 26 .....	96
The fracture morphology for a number of specimens tested at $207 \pm 69 \text{ MN/m}^2$ at various electrochemical potentials	
Figure 27 .....	97
The fracture morphology mix of specimens tested at -1.75v and $207 \text{ MN/m}^2$ mean stress for various applied cyclic loads	
Figure 28 .....	98
An SEM micrograph illustrating the case of caustic tunnels acting as the transition morphology between intergranular and transgranular failure modes	
Figure 29 .....	99
Caustic tunnels found near the external surface of a specimen charged at -1.75v	
Figure 30 .....	102
An optical micrograph illustrating preferential slip band attack in a pre-fatigued specimen polarized to -1.75v	
Figure 31 .....	104
Optical micrographs illustrating the interaction between the external tunnels and transgranular fatigue crack	
Table III .....	105
A summary of all single crystal data	
Figure 32 .....	106
A plot of resolved shear stress versus the number of cycles to failure for the various single crystals tested in fatigue	
Figure 33 .....	108
A series of SEM fractographs taken from an air fatigued single crystal	
Figure 34 .....	109
SEM fractographs characteristic of the cathodically polarized single crystal surfaces	
Figure 35 .....	111
SEM fractograph illustrating the brittle nature of the river lines found in the surface of the single crystal polarized to -1.75v	
Figure 36 .....	112
An SEM fractograph illustrating the structure of the surface roughened region from a single crystal polarized to -1.3v	

Figure 37 ..... 113  
The overall fatigue fracture morphology of a  $\langle 110 \rangle$  tensile axis orientation crystal polarized to -1.75v

Figure 38 ..... 114  
Examples of caustic tunnelling found on a single crystal fracture surface

Figure 39 ..... 115  
An SEM fractograph illustrating an area of pure cleavage adjacent to the caustic tunnelling shown in figure 38

Figure 40 ..... 117  
An SEM composite micrograph illustrating the various regions found in the  $\langle 110 \rangle$  tensile orientation single crystal fatigued at -1.75v

Figure 41 ..... 118  
A metallographic profile of the fracture surface shown in figure 40 illustrating approximate geometric relations between the various fracture morphologies

Figure 42 ..... 120  
A two stage carbon fractograph taken from the surface of a single crystal pulled to failure in tension

Figure 43 ..... 121  
Stress relaxation curves for the as processed material

Figure 44 ..... 124  
Stress relaxation curve for T-6 aged, polycrystalline, Al-5.0Mg-2.5Zn-1.5 tested in 1N  $H_2SO_4$  + .2N  $NaAsO_3$  at -1.75v vs SCE

Figure 45 ..... 125  
Stress relaxation curve for T-6 aged single crystal specimen tested in 1N  $H_2SO_4$  + .2N  $NaAsO_3$  at -1.75v vs SCE

Figure 46 ..... 133  
The proposed steps involved in transforming a  $\langle 112 \rangle$  kinks into sessile loops

Figure 47 ..... 134  
The proposed steps in transforming a screw dislocation into sessile dipoles

Figure 48 ..... 135  
Dislocation dipoles geometries

Figure 49 ..... 137  
Dilatation across a dislocation dipole array as a function of the relative spacing of the dipoles within the array

Figure 50 ..... 139

The normal stress on the midpoint plane of a dipole array  
as a function of the dipole geometry

Figure 51 ..... 140

The normal stress of a dipole array for various locations  
along the midpoint plane as a function of the individual  
dipole geometry

Figure 52 ..... 150

A plot of the hydrogen and deuterium pressure necessary to  
propagate a stationary crack in 4340 steel

Table IV ..... 163

Results of the hydrogen transport calculations comparing  
the relative efficiencies of the proposed mechanisms

Abstract

The effect of hydrogen on the corrosion fatigue behavior of an Al-5Zn-2.5Mg-1.5Cu alloy was investigated. In the study, a constant mean load ( $207 \text{ MN/m}^2$ ), S-N type test method was used to monitor the fatigue response under air and .5N NaCl environments. In both cases, specific experiments were conducted in an attempt to determine the operating failure mechanism.

In the air fatigue case, all specimens failed in a trans-granular mode. The cyclic stress-strain response of the alloy indicated that the alloy hardened as the fatigue process proceeded to the crack initiation stage. TEM examination of the dislocation substructure indicated a large density of dislocation dipoles in the slip bands. These observations are consistent with debris accumulation model suggested by Duquette and Swann.<sup>16</sup> The model proposes that the accumulation of dipoles within the slip band will exert an increasing cleavage stress across the slip plane. By using a conservative estimate of the dipole density (obtained from the TEM micrographs), it is possible to show that the dipole stress may reach levels in excess of  $100 \text{ MN/m}^2$ . Since this stress is thought to be additive to the applied stress levels, the model provides a plausible failure mechanism.

In addition to the laboratory air environment, tests were also performed in an aerated, .5N NaCl solution. In comparison to the air fatigue properties, the tests conducted under open circuit conditions (-.750v vs SCE) resulted in a marked decrease in the fatigue response. These failures were characterized by

an intergranular initiation leading to a transgranular cleavage type propagation mode. It was found that moderate polarization (to -1.3v vs SCE) produced little change in the fatigue response. Additional polarization to -1.75v vs SCE resulted in a further decrease in the fatigue strength. A comparison of the free corrosion rate with the electrochemical polarization diagram suggests that the observed embrittlement is linked to an increase in the surface hydrogen level. SEM fractographs also indicate that the degree of transgranular failure increases with both the surface hydrogen level and the applied cyclic stress.

In an effort to determine the hydrogen transport mechanism, a number of modified tensile tests were performed in the hydrogen charging environment (-1.75v vs SCE). The tests consisted of an initial macro yielding of the specimen followed by a stress relaxation period and a subsequent re-yielding. It was found that the specimens which failed transgranularly also demonstrated a serrated yielding behavior during the re-yielding process. This phenomenon indicated that hydrogen could be transported in the solute atmosphere of a dislocation.

These results indicated that the observed fatigue behavior could be explained by a hydrogen embrittlement mechanism. A model is developed which demonstrates quantitative agreement between the observed fracture morphology and the calculated dislocation transport efficiency. For low efficiency conditions, the observed fracture mode is thought to be hydrogen induced grain boundary separation. As the efficiency increases, the grain boundaries are depleted of hydrogen and the crack propagates along the embrittled transgranular path.

## INTRODUCTION

The 7000 series aluminum alloys were commercially introduced some thirty years ago. These alloys are high strength, precipitation hardenable metals which are based primarily on the Al-Zn-Mg system. Their excellent tensile properties (ultimate tensile strengths approaching  $650\text{MN/m}^2$ ) and low density ( $13\text{g/cm}^3$ ) made these alloys extremely attractive candidates for use in the aircraft industry. However, these attractive properties are overshadowed by poor fracture toughness and fatigue properties. Additionally, the alloys were found to be extremely susceptible to environmental embrittlement by moisture. Furthermore, this susceptibility was found to be inversely related to the mechanical strength. Some form of the embrittlement was found to be present under the influence of either a static stress (stress corrosion cracking) or a cyclic stress (corrosion fatigue). It is the purpose of this investigation to study the phenomenon involved in the corrosion fatigue process of these alloys in aqueous environments.

Since well over 600 papers have been written concerning the physical, metallurgical, and mechanical properties of these alloys, a rather extensive literature survey is provided. This survey is intended to develop a logical path from the existing literature to the materials and procedures used in this study. This section begins with a review of the physical metallurgy involved in the precipitation hardening of these alloys. A brief discussion of the various strengthening mechanisms found in the alloys is also provided. With this understanding of how and why the alloy obtains its tensile properties, the next section attempts to explain the current theories as to why these alloys have such poor inherent fatigue properties. After this brief explanation, the process

will become a bit more complicated with the addition of an aggressive environment. This will be accomplished by first introducing the effects caused by various gaseous environments. This discussion will point to the fact that the moisture content of the gas appears to be the critical parameter which measures the extent of the environmental damage. Several possible explanations for this behavior will be discussed.

With this information in hand, the situation will be complicated even further by considering various aspects of the aqueous corrosion of these alloys. Finally, with all this considered, a review of the aqueous corrosion fatigue behavior of the alloys will be presented. Once again, special attention will be paid to the various models proposed to explain the corrosion fatigue process.

Physical Metallurgy

Over the past thirty years, a great deal of work has been generated which deals with the thermal, mechanical, and metallurgical properties of the Al-Zn-Mg alloy system. Initial studies<sup>4,5</sup> centered around the solutionizing and precipitation characteristics of these alloys. These and later studies demonstrated that ultimate tensile strengths exceeding 650MN/m<sup>2</sup><sup>1</sup> could be achieved through proper thermal treatments.

Those treatments which act to maximize the tensile properties produce a finely dispersed, semi-coherent precipitate upon aging of the supersaturated matrix. The exact nature of the precipitate is very sensitive to local composition, aging temperature, and quench rate.<sup>3</sup> The  $\eta$  phase (H.C.P., MgZn<sub>2</sub>) is favored by Mg to Zn ratios of 1:2 to 1:10, low aging temperatures (below 150°C), and rapid quench rates. The T phase (Cubic, Mg<sub>3</sub>Zn<sub>3</sub>Al<sub>2</sub>) is however, favored by lower Mg to Zn ratios, aging temperatures above 150°C, and slower quench rates. Both of these precipitates are thought to form metastable intermediate phases. These phases are designated  $\eta'$  and T', and it should be pointed out that some investigators feel that the T phase may also develop from  $\eta$  nuclei.

The orientation relationship between the matrix and the precipitates is thought to change during the aging process.<sup>3</sup> The initial G.P. zones are thought to be vacancy-solute clusters which are coherent with the matrix. As such, they are not thought to produce a very effective strain field around the zones. In this state, therefore, the strength of the alloy arises primarily from the increased bond strength within the zones. Some additional strength is also gained from residual solid solution hardening.<sup>6</sup>

As the clusters grow, they begin to lose their coherency, but remain partially coherent on the  $\{111\}$  matrix planes. Since this is the slip plane, this semi-coherency acts to provide a very effective barrier to cross slip.

With longer aging times, the metastable precipitates transform to the equilibrium  $\eta$  and T phases. The T phase is reported to be cubic ( $a=14.34\text{\AA}$ ), with (100) T parallel to (112) matrix and (001) T parallel to (110) matrix.<sup>7</sup> The  $\eta$  phase is thought to be hexagonal, and thus far eight separate orientational relationships have been reported for this phase. As pointed out by Mondolfo,<sup>3</sup> the equilibrium phases of these precipitates have relatively low misfits, and therefore, the metastable particles can grow quite large before coherency is lost. Once this occurs, the precipitates no longer promote planar slip and cross slip is observed. In this overaged state, the mechanical strengthening is achieved primarily through precipitate strain field interactions with the dislocations, but some residual solid solution strengthening is also present.

As the precipitates grow very large, they begin to act in a manner very similar to intermetallic inclusions. In this case, the particle can serve as an internal stress concentrator. Under these conditions, it is possible to generate sufficient stress to cause cleavage of the particles. These cleavage cracks then act as nucleation sites for mechanical failure. Such particle initiated cracks can occur in tensile or fatigue tests, and can initiate either transgranular or intergranular cracks.

Although it is well established that the precipitate structure within the grain acts to control the slip process, a number

of investigators have suggested that the alloys' mechanical properties may be controlled by the grain boundary structure. This is especially true under environmental embrittlement conditions where intergranular failures are frequently found. The structure is generally described by three parameters: a. the types of precipitates present, b. the extent of precipitate coverage, and c. the width of the precipitate free zone (p.f.z.) adjacent to the grain boundary.

8-10

Nicholson and co-workers have made a thorough study of the grain boundary region. They conclude that both  $\eta$  and T phases may be present in a ternary Al-Zn-Mg alloy, with the exact mix being determined by the various parameters discussed earlier. It should be pointed out that various alloying additions and impurities, such as Fe, Cr, Zn, Ti, and B, may also form intermetallic compounds at the grain boundaries.

The extent of grain boundary coverage is a strong function of aging time, aging temperature, and quench rate. The longer the aging time or the higher the temperature, the greater is the coverage. It has been suggested that for very long times or high temperatures, a continuous grain boundary network may eventually form. The quench rate acts to determine the nucleation rate within the grain boundary.<sup>3</sup> For slow rates, nucleation occurs both during and after the quench. In this case a bimodal size distribution can occur, and rather extensive precipitate coverage can occur for the same aging characteristics which produce a low coverage rate under rapid quench conditions.

The width of the precipitate free zone is also determined by a nucleation phenomenon. The matrix precipitates are thought to nucleate through a vacancy-solute cluster. The grain boundary can act as a sink for vacancies and vacancy-solute pairs. This then creates a region which is denuded of nucleation sites, and therefore, precipitates. Since both the vacancy concentration and diffusion rate are temperature sensitive, the final width of the p.f.z. is dependent on the thermal history around the grain boundary. Higher solutionizing temperatures, faster quenches, and lower aging temperatures act to narrow the p.f.z. When 465°C is used as a solutionizing temperature, followed by a cold water quench and aging below 130°C, they combine to produce no p.f.z. at all. It should also be noted that the structure of the grain boundary appears to interact with the precipitation and p.f.z. phenomenon.

11

Judd and Shastry point out that the efficiency at which a grain boundary can accomodate vacancies and vacancy-solute pairs may be a function of the misorientation across the boundary. The larger misorientations lead to a higher sink efficiency. This increased attraction applies to the solute-vacancy clusters as well as to the individual vacancies themselves. This would tend to provide for a greater coverage in the high angle boundaries, and depending on how this localized alloying affects the various vacancy-solute binding energies, it could also lead to additional compositional gradients. These gradients would effect the nature of the precipitates present and also influence the formation of the p.f.z.

The physical metallurgy of these alloys involves a number of complex phenomena. Any variation in the fabrication parameters (i.e. solutionizing, temperatures, quench rate, aging temperature, aging time, etc.) is apt to change the physical structure of the alloy, and as it has just been outlined, these physical changes could manifest themselves as changes in one or more of the mechanical properties of the metal. It is very important, therefore, to clearly state the fabrication parameters before making any comparisons of mechanical properties. With the number of phenomena involved, it should also be pointed out that various alloys can yield identical data for one mechanical property (i.e. Y.S., UTS, fatigue endurance limit, etc.) and yet due to a difference in the physical state of the alloy, yield very different information concerning another parameter (i.e. elongation, fracture morphology, corrosion fatigue endurance limit, etc.).

Fatigue

As mentioned earlier, the Al-Zn-Mg based alloy systems have the highest tensile strengths of all aluminum based metals. Unfortunately, if one normalized the observed fatigue endurance limit to the ultimate tensile strength of these alloys, these same Al-Zn-Mg alloys also have the lowest fatigue strength of the commercial aluminum alloys. Over the years, a number of investigators have proposed various models to explain this inherently poor fatigue behavior. Many of these models concern the types of dislocation interactions which occur during the fatigue process. In general, these models can be divided into three categories:

1. The nature of the alloys is such that the fabrication of the metal will always produce localized precipitation free zones. These regions are, therefore, softer than the surrounding material. This provides preferential paths for dislocation motion. These paths include the grain boundary precipitate free zone and quenched in transgranular inhomogeneities. 2. The nature of the fatigue process produces a back and forth motion of dislocations. This motion acts to provide a continual shearing motion through the coherent precipitates. This cutting motion continuously reduces the size of the particles until they are no longer stable, and therefore, the remainder of the precipitate re-dissolves into solid solution. This again acts to promote a large number of easy paths for continued dislocation motion. 3. The nature of the fatigue process also acts to produce a large number of dislocation dipoles across the slip plane. The individual dipoles act to produce a tensile stress across the plane. The fatigue cycling results in a

continual accumulation of the dipoles. This accumulation therefore, provides for an increasing tensile stress across the slip plane. At some point a critical dipole density is reached. This occurs when the combined total of the applied tensile stress and the dipole tensile stress exceed the fracture strength of the material, thereby nucleating a crack. <sup>16</sup> Each of these models acts to explain specific observations, and the following discussion will illustrate that the applicability of each model may be somewhat limited.

<sup>14</sup> The inherent p.f.z. model was formulated by Laird and Thomas to explain the occurrence of transgranular crack initiation in the precipitation hardened aluminum alloys. Since that time, the same model has been used to explain intergranular failures common <sup>12,13</sup> to stress corrosion cracking in these alloys. Laird and <sup>14</sup> Thomas contend that the solutionizing and aging process would always produce localized inhomogeneities in the precipitate structures. In fact, they have thoroughly documented such behavior for Al-4%Cu alloy. As mentioned earlier, these precipitate free zones act to provide easy paths for dislocation motion. It was suggested that the local strength of these zones is so low that they could work harden to the point of failure before alternate slip systems become operational. Although this sequence may be valid for Al-4% Cu alloys, these authors failed to find any evidence for such behavior in the Al-Zn-Mg system, even though they conducted the same thorough search in both alloys. None the less, they still proposed the mechanism be operational for both alloys.

The same type of arguments are proposed to explain the intergranular failures found in S.C.C. In this case, however, the inherent soft path is due to the grain boundary p.f.z., which was discussed earlier. Proof for such a model lies in two independent observations of preferential dislocation motion within the p.f.z. However, no such behavior was seen in a number of other investigations, and DeArdo and Townshed, through the use of various over and under aging heat treatments, systematically varied the width of the p.f.z., and found little correlation with S.C.C. susceptibility. Additionally, Montgrain and Swann have used TEM to show that for Al-Zn-Mg alloys, intergranular S.C.C. cracks proceed directly along the grain boundary and not in the p.f.z.

The re-solution model is based on direct evidence of this behavior found in the work of Stubbington and Forsyth. They found that torsional fatigue of Al-Zn-Mg alloys induced precipitate re-solution in the slip bands. They suggested that re-solution was due to the continued cutting of precipitates by the motion of dislocations in the slip band. The resultant shear displacements act to reduce the effective particle diameter and increase the overall surface area. This acts to localize future strain, and thereby lead to the same type of premature failure predicted for the previous model.

Although the Stubbington and Forsyth micrographs illustrate that re-solution might occur, the applicability of this model may be limited strictly to the torsional fatigue case. No evidence for re-solution has ever been provided for specimens tested in a tensile mode. This fact even applied to the localized

areas where tremendous amounts of shear would be expected to take  
place (i.e. tips of fatigue crack). Grosskreutz and Benson in-  
vestigated the areas immediately surrounding a fatigue crack in  
2024-T3 and 7075-T6. Although re-crystallization and very high  
strain levels were evident, no change in the precipitate struc-  
ture was found. This observation was supported by Bowles and Broek,  
who were able to contrast the dislocation network within the plastic  
zone ahead of the crack tip. Although they were able to identify  
the dislocation structure associated with fatigue striation forma-  
tion, no changes in the precipitate structure were encountered.  
This work was also performed on a 7075-T6 alloy.

The critical defect model is based on the observed changes  
in the dislocation substructure of an Al-5Zn-2.5Mg alloy tested  
in reverse bending. Duquette and Swann correlated these changes  
with the extent of fatigue cycling. Their observations are shown  
in Figure 1. Figure 1a shows the typical quenched in dislocation  
structure. The helical nature of the dislocations is due to solute  
and vacancy condensation, and is characteristic of the alloy system.  
Figure 1b shows the slip band structure at 1% of the number of cycles  
necessary to initiate a fatigue crack ( $N_i$ ). The helical structure  
has begun to be replaced by long, relatively straight dislocations  
with a number of jogs along their length. Various tilting experi-  
ments show that the straight portion (B) is of a screw nature, and  
generally follows a  $\langle 110 \rangle$  direction. The jogs (A) were found to be  
primarily edge components along a  $\langle 112 \rangle$  direction. As cycling con-  
tinues, the screw portions of the dislocation tend to move from the  
sessile jog, and pinch themselves off to form dipole loops.



Figure 1

Dislocation structure of air fatigued Al-5Zn-2.5Mg alloy as a percentage of its fatigue life ( $N_i$ )

- a) 0% - illustrating helical dislocations characteristic of quenched in structure
- b) 1% ( $N_i = 10^4$  cycles) - illustrating a jogged screw dislocation where the components A 112 and B 110 were found to lie on different slip planes
- c) 67% ( $N_i = 6.7 \times 10^5$  cycles) - illustrating a slip band containing dislocation in various stages of development

These loops continue to form throughout the cycling process.

Figure 1c, for example, is at 67% of  $N_i$  and it shows that within a single slip band there are a large number of loops in all stages of formation. The completed loops were found to be primarily of an edge nature and lie across the primary slip plane. Duquette and

<sup>16</sup> Swann formulate that since edge dipoles have been shown to exert a tensile force across the plane of the dipole, fracture will occur when a critical dipole density is reached, the exact level being determined by the combined total of the applied tensile stress and the dipole induced tensile stress. When this total exceeds the fracture stress of the metal, a crack is initiated.

As these investigators point out, this model may also have limited applicability, the usefulness being determined by the <sup>22</sup> Kelly-Tyson-Cottrell criterion for ductile vs. brittle fracture. This treatment suggests that the failure mode of an alloy is related to the localized stress state. If the ratio of the resolved normal stress,  $\sigma$ , to the resolved shear stress,  $\tau$ , is greater than the ratio of the theoretical fracture stress to the theoretical shear stress, then cleavage will occur. If the local ratio is lower than this value, then a shear mode failure will occur. The role of the dipoles is to raise  $\sigma$  thereby promoting localized cleavage. This model can also be used to rationalize the torsional fatigue <sup>15,19</sup> observations of Stubbington and Forsyth. In this case, the resolved  $\sigma$  is very low, while the  $\tau$  is very large. Therefore, localized cleavage is not favored and an alternative shear mechanism (re-solution) may be operational. Finally, it should be <sup>16</sup> pointed out that the Duquette and Swann model is based on observa-

tions from reverse bending, high cycle fatigue tests on a peak hardened alloy, and therefore, the applicability to other heat treatments or testing conditions is yet to be proven.

Corrosion Fatigue

Corrosion fatigue can be defined as the dynamic, simultaneous interaction of a corrosive environment and a cyclic stress leading to the premature failure of a metal. The effect can best be illustrated by Figure 2 which schematically plots the applied fatigue strength versus the logarithm of the number of cycles to failure. The top curve shows a typical fatigue response for an inert environment. If, however, one were to corrode a test specimen prior to fatigue testing, the fatigue response would drop. The magnitude of the drop is determined by the nature of the corrosive attack; a greater geometric stress concentration effect is encountered in those cases where pitting is present. This effect is illustrated in the middle curve. In all cases, however, the simultaneous application of a corrosive environment and a cyclic stress result in the dramatic drop seen in the lowest curve. In general, the longer the interaction takes place (i.e. lower frequencies or lower cyclic stress), the more dramatic the effect. It should also be noted that the more aggressive the environment, the more pronounced is its interaction with the fatigue process.

For aluminum alloys, many investigators have shown that in reference to a relatively mild vacuum (approximately  $10^{-3}$  torr), even laboratory air demonstrates a marked, detrimental effect on the fatigue behavior.<sup>5,26</sup> It also has been shown that pure fatigue

of these metals occurs only under vacuum or ultra-dry, inert gaseous environments. In all other cases, the studies showed a drop in the fatigue resistance, or in other words, corrosion fatigue.

In an effort to obtain a clearer understanding of the phenomenon behind gaseous corrosion fatigue, a number of investigators have systematically tried to isolate the effects of the various constituents. Although there are conflicting results for other species, there is almost universal agreement that moisture is the major detrimental, environmental factor. For that reason, the effect of water vapor will be discussed first.

Depending on the type of test used, the effect of moisture can be either to lower the overall fatigue life (S-N testing)<sup>27</sup> or increase the rate of fatigue crack growth ( $da/dn$  vs.  $\Delta K$ ).<sup>28</sup> At this point in time, there exists no clear evidence as to the role moisture plays during the initiation process. In all cases, the magnitude of the embrittlement process is related to the partial pressure of the moisture present. At low pressure levels, there is virtually no effect, but as the moisture level increases, a critical pressure is reached. At this point, the alloy shows a marked drop in its fatigue response (either a decrease in  $N_f$  or an increase in  $da/dn$ ). The full extent of this degradation usually occurs over a relatively short pressure range. Beyond the critical level, the alloy demonstrates a fixed, relatively poor fatigue response. Due to its characteristic shape, the pressure vs. fatigue property ( $N_f$  or  $da/dn$ ) curves are usually referred to as "S" curves.

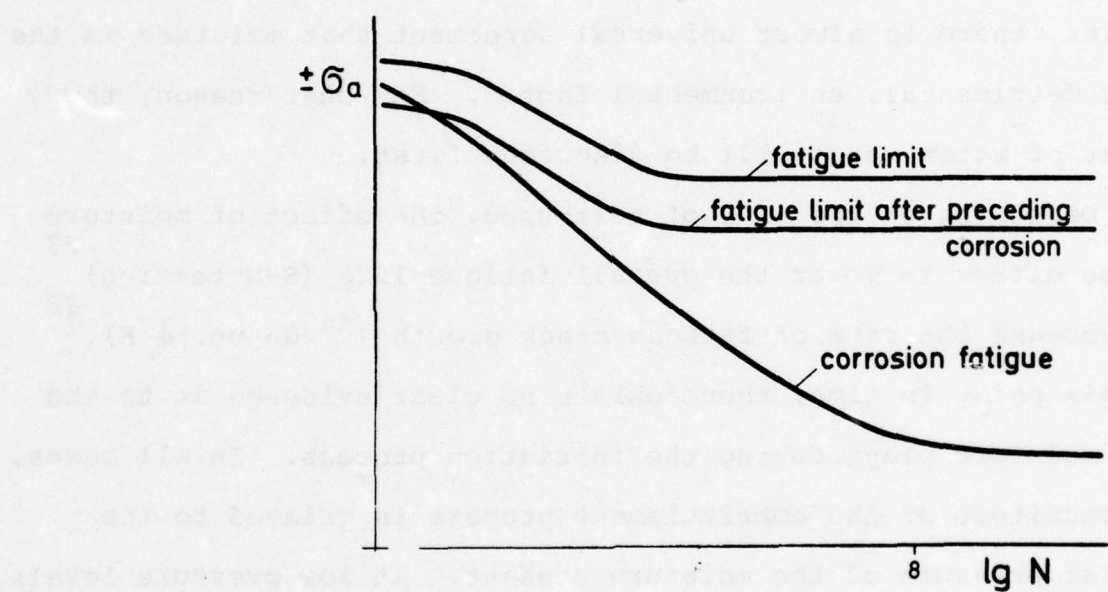


Figure 2

Schematic illustration of the effect of corrosion in the fatigue response<sup>(23)</sup>

<sup>28</sup>

Additionally, Hartman showed that the extent of the environmental damage was more pronounced at lower  $\Delta K$  values. It should also be pointed out that the corrosion fatigue damage is known to be a strong function of the testing frequency. As the testing frequency is lowered, more time per cycle is allowed for environmental interaction, and subsequently, the greater is the environmental embrittlement.

Currently there are two models proposed which attempt to strictly interpret the role of moisture in the embrittlement phenomenon: 1. a high pressure hydrogen model, and 2. an adsorption-induced oxide weakening model. The first model was originally proposed by Broom and Nicholson. It suggests that the water reacts with any freshly exposed metal through the reaction  $(2Al + 3H_2O \rightleftharpoons Al_2O_3 + 6H)$ . While the majority of the hydrogen atoms recombine to form hydrogen gas at the external surface, some of the hydrogen diffuses into the aluminum. These atoms collect at various internal defects, and re-combine to form high pressure gas pockets. The pockets act to raise the local stress intensity, and thereby reduce the external stress necessary to produce a given crack increment.

The model is supported by various observations reported by Wei. Fatigue tests on 7075-T6 were performed in distilled water and a number of dry gaseous environments. In all cases fatigue crack growth was controlled by a thermally activated process. The measured activation energy varied inversely to the applied stress intensity and for the same  $\Delta K$ , the dry environments showed a much greater activation energy. The magnitude of the

<sup>30</sup>

activation energy ruled out either the bulk diffusion of hydrogen within the metal or the transport of the corrosive media to the crack tip, as being the rate controlling step. Instead, Wei concludes mechanical breaking of the surface oxide (i.e. the exposure of fresh metal surface) to be the controlling step. Additionally, he cites the fact that environmental sensitivity shows a thickness effect. For a given  $\Delta K$  and crack growth rates up to  $2.54 \times 10^{-4}$  cm/cycle, thicker test specimens (from .13 to .64 cm) yield a faster growth rate. This effect is compatible with the high pressure model in that the thinner specimens are subjected to a plane stress mode of growth. This mode has a much larger stress-relieving ability than the plane strain situation of the thicker specimens. This plastic relaxation acts to lower the effective localized stress intensity caused by the hydrogen pockets.

Although this model appears relatively straightforward, it suffers from the experimental flaw that no sign of gas pockets has ever been found on the fatigue fracture surface. This may be contrasted with similar cases for steels, where the fractographic evidence has demonstrated the applicability of the high pressure hydrogen gas model to static hydrogen embrittlement,<sup>31</sup> S.C.C.,<sup>32</sup> and some corrosion fatigue failures.<sup>33</sup>

In addition to this model, oxide weakening was proposed by Hartman<sup>27,28</sup> to explain the role of moisture in the corrosion fatigue process. This model relied heavily on the experimental work of Grosskreutz<sup>34</sup> coupled with the theoretical work of Head<sup>35</sup> and Connors.<sup>36</sup> Head and Connors showed that the ratio of the

moduli between a surface film and the base metal acted to control the nature of the dislocation image force created at the free surface. The calculations predict that if the modulus of the oxide is less than that of the substrate, an overall attractive force exists, and dislocations move to the free surface. If the oxide modulus is greater than 1.8 times that of the substrate, the dislocations are repelled by the surface. However, for intermediate values, the attractive and repulsive forces partially cancel, and the dislocations become trapped a finite distance below the surface.

This theoretical model agrees quite well with the observations of Grosskreutz.<sup>34</sup> In a series of experiments, he was able to correlate changes in the fatigue generated substructure with environmentally induced changes in the modulus of the surface oxide. Reverse bending fatigue tests ( $\pm 1 \times 10^{-3}$  strain) were performed on pure aluminum in laboratory air and  $10^{-9}$  torr vacuum. The air test revealed well developed surface slip markings and rather dense clusters of sessile dipoles lying just below the surface. If the same test is duplicated under  $10^{-9}$  torr, the surface shows only very fine slip markings. The dislocation substructure is a very dense mixture of dipoles and what appear to be trapped dislocations. In an effort to confirm the entrapment phenomenon, tensile tests were performed on 3000 Å oxide films. Grosskreutz<sup>34</sup> found a modulus of  $5.5 \times 10^7 \text{ MN/m}^2$  for films tested at 760 torr, and when the pressure was reduced to  $10^{-6}$  torr the modulus rose to  $21.3 \times 10^7 \text{ MN/m}^2$ , that in comparison to the modulus for pure aluminum, the vacuum case should produce surface repulsion

The air case, however, would act to produce an attractive surface image force, and therefore, create much stronger surface markings and a lower internal dislocation density. Both of these observations are consistent with the theoretical model discussed earlier.

It should also be pointed out that the actual modulus observed in vacuum depends on the amount of time spent under hard vacuum.

Grosskreutz<sup>34</sup> has observed values as high as  $3.4 \times 10^8$  MN/m<sup>2</sup> for films stored nearly 20 hours at  $10^{-6}$  torr. He attributes these environmental effects to the hydroscopic nature of the oxide.

Hartman<sup>27,28</sup> suggested that the moisture dependent fatigue behavior seen in the aluminum alloys is a reflection of the mechanical state of the surface oxide. The higher moisture levels produce a lower modulus oxide. This acts to reduce the surface image force, and eventually produce an attractive force at the surface. As Grosskreutz<sup>34</sup> has already shown, this leads to dislocation runout and very large surface offsets. These offsets would act as geometric stress raisers and thereby, produce a premature failure.

In considering this model, a number of points must be raised. First, although it was originally proposed strictly to explain the role of moisture, the experimental data cannot rule out the same effect caused by another environmental species. Secondly, the work of Grosskreutz<sup>34</sup> clearly illustrates that such a model must play a role in crack initiation. However, Hartman also envisages the same model controlling crack propagation. As pointed out by Wei,<sup>30</sup> it is very difficult to carry this idea to the monolayer surface coverage usually suggested for a growing fatigue crack.

As mentioned earlier, in addition to moisture, other gaseous constituents have also been reported to cause a degradation of the observed fatigue properties. Oxygen for example, has been shown to increase the crack growth rates at low  $\Delta K$  (below 25.5  $\text{Kg/mm}^3/2$ ) and decrease it for higher  $\Delta K$  values in a DTD683(Al-Zn-Mg) alloy.

<sup>37</sup> <sup>29</sup> Broom and Nicholson report that cold trapped (-183°C) oxygen had little effect on an Al-4%Cu alloy, while the same environment produced a 50% reduction in fatigue life for DTD683 alloy. <sup>39</sup> Hordon and Wright report that oxygen was almost as detrimental as  $\text{H}_2\text{O}$  vapor <sup>24</sup> for 1100 Al. Bradshaw and Wheeler also observed a large detrimental effect on high purity aluminum, but report that oxygen environments had almost no effect on either 2024 (Al-Cu) or DTD5070 (Al-Cu-Mg).

Conflicting results can also be found for the role of hydrogen. <sup>39</sup> Wright and Hordon report that for 1100 Al, hydrogen was almost as damaging as  $\text{H}_2\text{O}$ , but indicate that the effect might also be correlated to the partial pressure of oxygen present. In a more systematic study, <sup>28</sup> Broom and Nicholson report that cold trapped (-196°C)  $\text{H}_2$  acted to reduce the fatigue life of three aluminum alloys (Al-4%Cu, L65, DTD 683) by at least 50% as compared to dry <sup>25</sup> nitrogen. This conflicts with other researchers, who report that dry hydrogen gas had no effect on fatigue crack growth rates.

A number of models have been suggested to explain the various modes of gaseous corrosion fatigue in aluminum alloys. The two models which were originally intended to specifically deal with moisture induced embrittlement have already been discussed. Additionally, a number of other models have been proposed to deal with

effects found in both wet and dry environments. These models can be grouped into three general areas: 1. interference with slip reversal,<sup>40</sup> 2. accelerated corrosion at a crack tip,<sup>41</sup> and 3. surface adsorption.<sup>42-4</sup>

The restrictive slip models are based on fractographic comparisons between vacuum and air fatigue failures. Pelloux argues that in the presence of an oxidizing environment, any fresh aluminum exposed during the fatigue process will be quickly oxidized. This oxide layer prevents the reversibility of emerging slip steps, and therefore, leaves a systematic marking of the crack growth per cycle. These markings are commonly called striations. Under vacuum conditions, however, the reverse slip process is not impeded, and in addition to leaving no surface markings, the reversibility acts to lower the cyclic crack growth rate.

The accelerated corrosion model has been suggested by Laird<sup>41</sup> and Smith to explain the effect of oxygen on the fatigue behavior of a number of f.c.c. materials, including aluminum. It is based on the fact that the non-reactive, noble metals do not show any detrimental fatigue behavior in the presence of oxygen, and that the more reactive metals show no embrittlement when fatigued under inert environments. These authors, therefore, suggest that oxygen acts to increase the crack growth rates by causing accelerated corrosion at the crack tip.

The surface adsorption model is based on the "S" shaped curve discussed earlier. Through the use of the kinetic theory of gases<sup>43,44</sup> and a few simplifying assumptions, Achter and co-workers have been able to quantitatively predict where the critical embrittle-

ment pressure should lie. The assumptions include the following: a. the crack is exposed for only part of the fatigue cycle, b. the crack advances in discrete, incremental steps of the order of the lattice parameter, and c. each step becomes fully saturated with adsorbate before the next crack extension begins. The resultant pressure equation is:

$$P_c = 2.67 (MT)^{1/2} \left( \frac{da}{dn} \right) f \text{ (torr)}$$

where

M = molecular weight of the adsorbate

T = absolute temperature

$\frac{da}{dn}$  = crack growth rate

f = cyclic frequency

When the appropriate figures are used, (for example, see reference 27), the equation predicts the saturation pressure within an order of magnitude.

In a physical sense, the absorption model depends on the fact that the absorbing species creates a weak bond with the metal substrate. This chemisorbed bond acts to lower the bond strength of the metal-to-metal surface bonds. This weakening produces a lower bond fracture stress, and therefore, accounts for the observed environmental damage.

In reviewing the proposed mechanisms, only the surface adsorption model appears to be general enough to account for all the reported results. It, however, suffers from the fact that the quantitative agreement between Achter<sup>43</sup> and Hartman<sup>27</sup> is an isolated case, and it is unknown whether this type of agreement could be expected

in other alloy-environment couples. Another drawback to the model lies in the quantification of the actual embrittlement phenomenon. The Achter model predicts when monolayer coverage will occur, but does not provide any information concerning the relative strengths of the embrittling agents. In order to qualify this aspect, one must develop a method for measuring surface bond strengths in the presence of various environments. Ideally, the method should be flexible enough to allow measurements during the fatigue-environment interactions. At this point in time, these criterion are impossible to meet, and therefore, the essence of the model remains very qualitative.

In considering the other models, no one is able to explain all the reported results. This may well be due to the fact that a number of different mechanisms may be operational; depending on the specific alloy and environmental couple. Additionally, each model relies upon a different type of evidence for support, and therefore, it is often difficult to interpret the evidence from one model in terms of the mechanism proposed by another model. For example, the accelerated corrosion model should provide corrosion products on the fracture surface, and therefore, a quick compatibility check is provided by simply noting the fracture surface morphology. Even this rather simple check is usually not performed, however, unless the particular investigators model deals with fractographic evidence.

In conclusion, the gaseous fatigue work indicates that  $H_2O$  vapor is very detrimental to aluminum and its alloys. The same might be true of  $H_2$  and  $O_2$ , but additional, more systematic studies

are needed. Finally, a number of models exist which appear to explain part of the observed results, but no model is general enough in scope to explain all the reported data. It should be said, however, until sufficient research is performed to remove the conflicts within the reported data, this partial resolution may be all that can be expected.

#### Aqueous Corrosion

In attempting to characterize the corrosion behavior of aluminum alloys, it is appropriate to first consider the role of the surface oxide. Whenever a clean aluminum surface is exposed to air, it rapidly forms a thin oxide layer, and it is the adherent, protective properties of the oxide, ( $Al_2O_3$ ) which provide the base metal with its corrosion resistance. The oxide is relatively chemically inert, and acts as a diffusion barrier between the aggressive environment and the base metal. Therefore, in reviewing the corrosion behavior of these alloys, special attention must be paid to environmental impact on the structural and chemical integrity of the oxide.

When aluminum is submerged in an aqueous environment, the thin (approximately 35 Å), air formed film begins to break down. The resultant state of the oxide is then determined by the relative rates of film dissolution and repair. The initial dissolution rate is reported to be nearly independent of pH, within the range pH 1 to 10, but increases at higher pH levels. The reaction is diffusion controlled in both cases: hydrogen ions levels act to control the low pH rates, and hydroxide ions concentrations limit the high pH

reaction kinetics. In commercially pure aluminum, grain boundary segregation provides the cathodic (electron removal) reaction sites. This reaction acts to raise the local pH, and therefore increases the local dissolution reaction. This accelerated dissolution reaction also leads to some aluminum ion removal (an anodic process) at these cathodic sites. It should be remembered that the site is termed cathodic when the net reaction provides electron removal. Vedder and Vermilyea report grain boundary attack to be four times faster than the overall anodic reaction.<sup>45</sup>

The film repair mechanism is thought to be the precipitation of aluminum hydroxide. The hydroxide appears to form a plate-like network over the metal surface. Within the first 300 Å, the oxide structure appears nearly continuous, but as the film thickness increases, the structure is found to be quite porous. The hydroxide reaction proceeds very rapidly at first, but acts to slow down with time. It has been suggested that the initial rate is controlled by the oxide dissolution kinetics. This reaction provides material which can be redeposited as hydroxide with very little diffusional transport. After the dissolution ceases, prospective reactant materials must diffuse through both the solution double layer and the pre-existing hydroxide. This acts to slow the overall reaction rate.

The overall reaction kinetics are also known to be a strong function of pH. As mentioned earlier, the initial dissolution rate increases at high pH. Below pH 4 and above pH 8.5, the newly formed hydroxide film is also soluble. This acts to remove the diffusion barrier and produces a constant corrosion rate. The hydroxide also

tends to be more porous at high pH levels. This acts to reduce the efficiency of the barrier and provides for higher corrosion rates at these levels.

The oxide integrity is also a function of the applied electro-  
chemical potential. Pourbaix and co-workers have developed potential-pH diagrams for a vast number of metals, including aluminum. Using strictly thermodynamic considerations, these investigators determined which of the possible equilibrium reactions would occur at any combination of pH and applied potential. Although the Pourbaix diagrams, as they are commonly called, do not consider kinetic phenomenon nor the effects of soluble complexes and insoluble salts, they do offer a starting point for understanding the electrochemistry of the base metal. Their calculations predict that in the presence of sufficiently acid conditions, aluminum decomposes with the generation of hydrogen gas according to the reaction  $(2\text{Al} + 6\text{H}^+ \rightleftharpoons 2\text{Al}^{+3} + 3\text{H}_2)$ . In the range pH 3.5 to 8.5, the oxide remains stable, and the metal is said to be in a corrosion resistant, passive state. At high pH levels, the oxide is again unstable and the aluminum decomposes water with the generation of hydrogen, according to the reaction  $(\text{Al} + 2\text{H}_2\text{O} \rightleftharpoons \text{AlO}_2^- + 2\text{H}_2)$ .

As mentioned earlier, the work of Pourbaix is limited to those cases where no insoluble salts or soluble complexes are capable of being formed. The work of Ito, et.al., also indicates that within the passive range, the oxide solubility is strongly influenced by the presence of specific anions and cations. For example, aluminum is known to be passive in both concentrated nitric acid (pH-1) and ammonium hydroxide (pH-13), but is vigorously

by sodium hydroxide near neutral pH levels.

Thus far, the discussion has considered the overall corrosion characteristics of the aluminum system. There are however, specific conditions which promote only a localized breakdown of the protective film. These breakdowns act to fix the corrosion processes to very small areas on the specimen surface. This promotes very large current densities, and usually, disasterous localized corrosion. This attack provides very effective geometric stress concentrators, and thereby, acts to reduce the mechanical strength of the metal. For the purpose of this review, the mechanisms behind these modes of localized attack will be discussed: pitting corrosion, intergranular corrosion, and stress corrosion cracking.

Pitting corrosion is usually associated with the presence of halide ions in the electrolyte. The halide ions are known to interfere with the film repair reaction. Thus far, two models have been proposed which attempt to explain the role of the halides in this reaction. Pryor and co-workers<sup>49,50</sup> believe that the ions act to accelerate the initial oxide dissolution reaction. Using a-c impedance measurements and TEM, these investigators formulate that the halide ions (especially chloride) first act to produce localized areas of increased ionic transport. Once the transport has produced a chloride impregnated structure, limited experimental evidence suggests that preferential oxide dissolution will occur at these sites. This action produces a localized break in the oxide film, and as will be pointed out shortly, the presence of the chloride ions acts to prevent the reformation of the film. This model

suggests two separate steps in the pitting process, an initiation period and a propagation stage. This correlates well with current versus time plots of the pitting phenomenon.

Once the localized break occurs, through either model, it exposes fresh aluminum to the electrolyte. This metal is anodic to the remainder of the surface. At this point there is a competitive reaction process between the pitting agent ( $\text{Cl}^-$ ) and the hydroxide reaction discussed earlier. If the film healing reaction dominates, the break is closed and no pitting occurs. The chloride, however, reacts to produce a soluble corrosion product. This reaction continually exposes fresh metal, and the proximity of the freshly dissolved  $\text{AlCl}_3$  acts to perpetuate the same reaction. As the pit deepens, the chloride ions tend to stay at the base of the pit and soluble aluminum ions react with any available hydroxide ions to produce aluminum hydroxide  $\text{Al(OH)}_3$ . This salt is only slightly soluble, and begins to precipitate on the upper portions of the pit walls. As the reaction continues, it removes hydroxide ions from the pit electrolyte, thereby making the remaining solution more acidic. Since the hydroxide covered surfaces are cathodic to the aluminum in contact with the acidic solution, the pit has become self sustaining. As the pit continues to propagate, lateral growth of the surface hydroxide acts to isolate the pit from any influence of the bulk electrolyte. Once this occurs, the pit will continue to grow until the precipitation process raises the electrolyte resistance to the point where the resultant polarization reduces the current to negligible levels.

51,52  
Wood and co-workers, however, contend that all aluminum oxide structures contain flaws. These flaws arise from both chemical inhomogeneities and mechanical stress-relieving processes. This porposition is based on a failure to observe unflawed films in the TEM. Therefore, since the oxide already contains a large number of flaws (approximately  $10^6/\text{cm}^2$ ), the role of the halide ion is limited to preventing the film forming process from healing the oxide break. In this respect, the model suggests that pitting is strictly a propagation phenomenon.

Although this has been a generalized treatment of the pitting process, a number of experimental observations tend to confirm its validity. For example, using this model, Pryor has calculated 2.8 to be the lowest, theoretical pH level allowable in the pit. A number of investigators report in situ measurements approaching three. Additionally, the model is also confirmed by the aluminum hydroxide modules which are often found at the opening of the pits. It should also be stated that hydrogen gas is often seen emanating from the mouth of the pit. It is theorized that the gas arises from some of the intermediate complexing reactions which occur in the pit. Its presence acts to confirm the self-sustaining acidic nature of the pitting process.

As noted earlier, the resultant morphology of the pitting process can be quite important in determining the mechanical response of the metal. For most commercial aluminum alloys, the pitting process is usually associated with the presence of an Fe or Si rich inclusion. These particles are cathodic to aluminum, and the resultant potential difference provides the driving force for the dissolution of the alloy. The particles usually have the long, narrow geometry characteristic of stinger-type inclusions. When this geometry is coupled with the locally high current densities of the pitting process, the resultant pit is found to have a deep, narrow, crevice like geometry. Standard fracture mechanics equation demonstrate this to be an extremely effective stress concentrator.

In addition to this more common mode of attack, a number of investigators report that the pitting process can demonstrate

crystallographic dissolution. Although this "tunnelling" attack (so named for the long, narrow dissolution paths) is reported for a number of different systems (304 stainless steel, Cu-Au alloys, lithium fluoride salt, and diamond), it is usually found in relatively pure aluminum ( $\geq 99\%$  Al). Additionally, even though it is currently being used on a commercial basis (Al electrolytic capacitor foils), very little is known concerning the actual mechanism involved in the tunnelling process. In general, the tunnels are reported to a square cross section ( $0.1\mu$  to  $1\mu$  wide) and a very large length to width ratio. Through the use of an etched TEM foils, Edeleanu was able to determine that in aluminum the tunnels generally follow  $\langle 100 \rangle$  crystallographic directions. It should also be noted that Diegle reports for an Al-400 ppm Fe alloy showed a marked decrease in the degree of tunnel formation if the alloy was subjected to a 350°F aging treatment prior to etching. Hunter also reports that a fully cold worked (H19) capacitor foil showed a marked increase in the tunnel density over a fully anneal sheet ("O" temper).

The specific geometry of the tunnels is thought to result from the inhibition of the lateral dissolution process for metallic systems, Swann has suggested that this is accomplished by covering the side walls of the tunnel with a noble constituent. He feels this is accomplished by either electrochemical plating of the noble species or preferential dissolution of the anodic species. Although these processes may occur in the particular system studied by Swann, they do not explain how the process might occur in a non-metallic system. In these systems, the mechanism is probably chemical

rather than electrochemical in nature.

Intergranular corrosion is a form of localized corrosion in which a long, narrow path is preferentially corroded out along the grain boundaries of a metal. Its mechanism is electrochemical in nature, and depends on the formation of local galvanic cells along the grain boundary. These cells are a direct result of the difference in electrochemical potential between the grain boundary precipitates and the adjacent metal. This theory was first suggested by Dix<sup>63,64</sup> for the Al-4Cu alloys in which both the grain boundary precipitates and the grain interiors are cathodic to the grain boundary denuded zone. The relative area difference produces very high current densities in the denuded zone, and therefore, this area is rapidly corroded away.

In the Al-Zn-Mg alloys, the  $MgZn_2$  particles are anodic to the grain interior. Once again the high cathode to anode area ratio acts to produce rapid dissolution. The severity of the reaction is therefore, controlled by the microstructure of the alloy. For example, overaging produces a large uniform distribution of second phase particles within the grain, and in so doing, acts to raise the anode to cathode ratio. In this condition, these alloys show only a very slight tendency for intergranular corrosion.

Stress corrosion cracking is the premature failure of materials caused by the interaction of a continuously maintained tensile stress (often below the .2% offset yield stress) and a corrosive environment. If either the tensile stress or the corrosive environment were absent, no failure would be encountered. In aluminum alloys, the failure is generally intergranular, and has been limited mainly to the

strong precipitation hardenable alloys of the 2000 and 7000 series.

Historically, the mechanism of stress corrosion cracking was first suggested to be an extension of the intergranular corrosion mechanism which was just discussed.<sup>64</sup> This theory was invoked because the majority of the failures were intergranular and the failures occurred in environments which were susceptible to intergranular corrosion. It was envisioned that the first stage of cracking would be the initiation of grain boundary fissures caused by intergranular corrosion. The geometric nature of these fissures would produce a stress concentration effect at the root of the tunnels, and the imposed tensile stress would produce tearing between the fissures. The tearing process would produce fresh metal, and the cycle would begin again.

This early model was attractive from two viewpoints. First, it offered an explanation for the discontinuous mode crack propagation, and secondly, it acted to explain why small amounts of cathodic protection would act to reduce the susceptibility of these alloys to the stress corrosion phenomenon. Later evidence did, however, cast some doubt as to the applicability of the model. For example, as shown in Table I, a number of environments do exist where intergranular corrosion is found without stress corrosion cracking, and vice versa. Additionally, fractograph evaluation of the intergranular facets often show no signs of the corrosion-related fissures envisioned by this model.

Since the appearance of the precipitate dissolution model some thirty years ago, at least seven other theories have been

Table I

Relationship between intergranular corrosion and stress corrosion cracking for a number of high strength aluminum alloys (64)

Intergranular Corrosion	and	Stress-Corrosion Cracking
Alloy	Environment	Ref.
7075-T651	NaCl-AlCl <sub>3</sub> solution acidified with HCl	59
7178-T651 7075-T651 7079-T651	Acidified aqueous iodide solutions	60
2024-T351 6070-T6 6066-T6 and slowly quenched 6061-T4	Alternate immersion in 3.5% NaCl solution	59

No Intergranular Corrosion	and	No Stress-Corrosion Cracking
Alloy	Environment	Ref.
7075-T73 7075-O	Chloride solutions	59
2024-T3 quenched at rates 3000 F/sec.	Chloride solutions	61

No  
Intergranular  
Corrosion

but

Stress-  
Corrosion  
Cracking

Alloy	Environment	Ref.
7039-T64	Boiling 6% NaCl solution	62
7075-T651	Hexene Engine oil Flight fuel Air, 2% RH	60
7079-T651 7039-T64 7039-T61	Air, 50% RH	60
7075-T6 & 2024-T3 re-heat- treated & rapidly quenched	Chloride solutions	59

Alloy	Environment	Ref.
6061-T6	Alternate immersion in 3.5% NaCl solution	59
Al-Mg-Si alloys	Chloride solutions	59 47
2024-T6 2024-T8	Chloride solutions	59

proposed. At this point in time, no one model is universally accepted. For that reason, a critical review of the merits and faults for six of these models is left to the review articles by 2,66,70 and Spiedel et.al., and Sprowls et.al. These reviews do an excellent job of summarizing the pertinent aspects of the following models: 1. stress activated dissolution, 2. film rupture, 3. tensile ligament instability, 4. stress induced diffusion of an embrittling species, 5. preferential slip and dissolution along the p.f.z., and 6. matrix precipitate control of the dislocation structure.

Very recent evidence, however, points toward the fact that a somewhat more universal mechanism for stress corrosion may also be applicable to the high strength aluminum alloys. According to 18 a number of papers at a recent conference, hydrogen embrittlement is widely accepted as the cause of stress corrosion cracking in steels and titanium alloys. The following is, therefore, a partial summary of the evidence which supports such a model for aluminum.

In a series of tests conducted on an Al-7%Zn-3%Mg alloy, 18 Montgrain and Swann used high voltage electron microscopy (HVEM) and mass spectrometry to evaluate the role of hydrogen. Specimens were subjected to various heat treatments which were known to produce stress corrosion susceptibility in the presence of moist air. Figure 3 shows the hydrogen gas evolution from three specimens pulled to failure in the mass spectrometer. Curve A shows the results for a specimen subjected to dry air for 28 days, and electropolished just prior to fracture. It shows almost no hydrogen

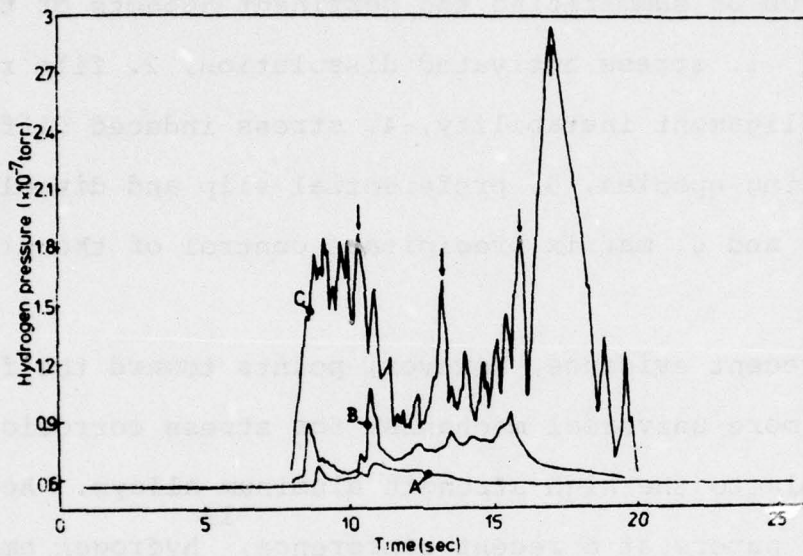


Figure 3.

Evolution of hydrogen for an Al-7Zn-3Mg alloys pulled to failure (18)

Specimen A: air cool, 25°C for 28 days in dry air, electropolished

Specimen B: as specimen A with no electropolish

Specimen C: CWQ, 25°C for 28 days in water saturated air, electropolished.

evolution. Curve B is from a specimen subjected to the same conditions as that of A, except it was not electropolished. The increased hydrogen level indicates that hydrogen either remains in the thermally formed oxide or it is trapped below the oxide at the metal interface. Curve C represents the hydrogen liberated from a specimen exposed to water saturated air for 28 days and electropolished prior to testing. In addition to the overall increase in hydrogen, these investigators also noted (by the arrows), the incidence of intergranular cracking. The correlation between grain boundary failure and hydrogen evolution is quite striking.

Additionally, by using the HVEM to examine thin foil, U-bend type specimens subjected to the same embrittling conditions, they were able to show that hydrogen induced failure occurred directly along a grain boundary and not in the p.f.z., as had been proposed in model 5 listed earlier. These investigators also noted that the grain boundary separation occurred with no local evidence of anodic dissolution (as proposed in model 1), and a lack of dislocation substructure on either side of many of the cracks indicated that the failure was of a cleavage rather than shear mode. It should be noted that an intergranular crack could be halted by the impingement of a slip band upon the grain boundary. Swann suggests that the slip band acts as a competitive sink for the hydrogen, and thereby, lowers the grain boundary hydrogen level below the critical level needed for decohesion.

This hydrogen-dislocation coupling has also been observed by  
71  
Donavan. Using radioactive tracer techniques, he followed the

tritium release rate during a tensile test of 5086 aluminum alloy. He observed a direct correlation between discontinuous yielding and the hydrogen release rate. Since the Portevin-LeChatelier effect is known to result from dislocation-solute break away, the simultaneous increase in tritium release confirms the attractive dislocation hydrogen interaction.

The hydrogen embrittlement phenomenon has also been applied to aqueous stress corrosion cracking in the work of Gest and <sup>72</sup> Troiano. These investigators were able to show that sufficient cathodic charging acted to embrittle the 7075-T6 alloy system. Although this appears to conflict with data cited earlier, Figure 4 offers an explanation for both observations. This figure correlates both the hydrogen permeation rate (curve A, as measured by Gest and Troiano) with the stress corrosion cracking <sup>70</sup> <sup>72</sup> rates (curves b,c,d as measured by Spiedel and Berggreen ) as a function of the applied potential. The figure shows a direct relationship between the permeation rate and the crack growth rate.

In addition to the permeation data, Gest and Troiano report additional data which favors a strain aging type embrittlement model. For example, under tensile loading, the degree of embrittlement increases as the strain rate decreases. Also, once the hydrogen charging is stopped, the degree of embrittlement is found to decrease a function of storage time. Finally, internal friction measurements of the hydrogen charged specimen show stress relaxation peaks characteristic of interstitial-dislocation interactions.

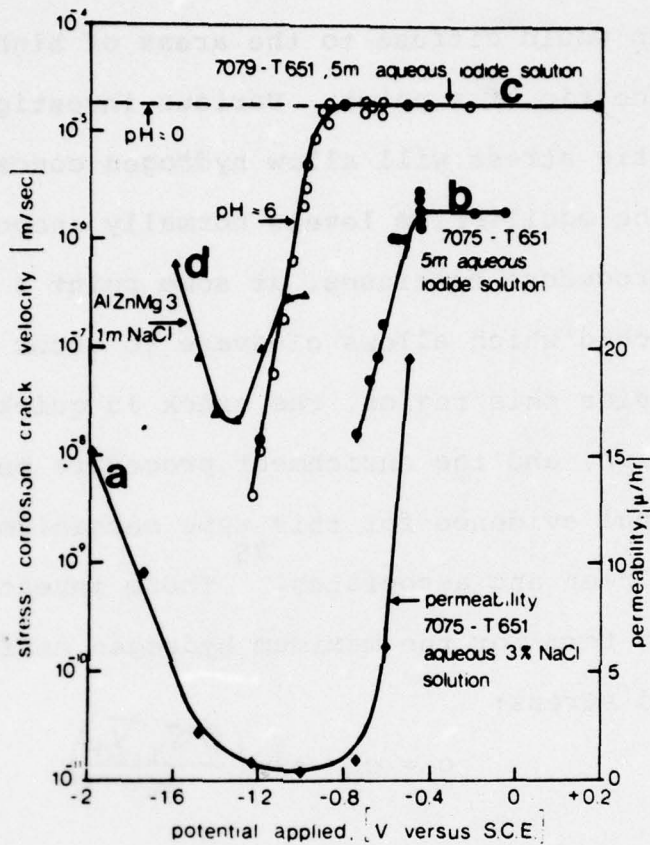


Figure 4

Hydrogen permeation rate and stress corrosion cracking rates as a function of applied potential (108)

Curve a - hydrogen permeation rate for 7075-T6 in 3% NaCl

Curve b - stress corrosion cracking rate for 7075-T651 in 5mKI

Curve c - SCC rate for 7079-T651 in 5mKI

Curve d - SCC rate for Al-Zn-Mg<sup>3</sup> in 1mNaCl

The actual model is based on parallel observations in  
73, 74  
various high strength steels. This previous work indicated  
that hydrogen would diffuse to the areas of high triaxial stresses,  
usually at the tip of a notch. Various investigators report that  
the hydrostatic stress will allow hydrogen concentration levels to  
far exceed the equilibrium levels normally encountered. As this  
enrichment procedure continues, at some point a critical hydrogen  
level is reached which allows cleavage to occur in the embrittled  
volume. Outside this region, the crack is quickly blunted by dis-  
location motion, and the enrichment procedure begins again.

Additional evidence for this type mechanism can be found in  
75  
the work of Green and associates. These investigators developed  
the following term for the maximum hydrogen enrichment value due  
to an imposed stress:

$$c = c_o \exp \left( \frac{\phi \sigma_y \bar{V}_H}{kT} \right)$$

where  $c$  = hydrogen concentration due to an  
imposed hydrostatic stress

$c_o$  = equilibrium hydrogen concentration  
under 1 atmosphere pressure

$\phi$  = geometric constant relating the  
maximum hydrostatic stress ( $\sigma_{H_{max}}$ )  
to yield stress ( $\sigma_y$ ) by:

$$\sigma_{H_{max}} = \phi \sigma_y$$

$\sigma_y$  = yield stress in uniaxial tension

$\bar{V}_H$  = partial molar volume of hydrogen  
in solution

$k$  = Boltzmann's constant

$T$  = absolute temperature

Values for  $\phi$  in type I (tensile) and type II (shear) loading for most metals are found to be 2 and .7, respectively. The value of  $\phi$  for type III (torsional) loading is zero. Therefore, a check of the strain aging model can be obtained by comparing stress corrosion results from type I and type III loading modes. This data is shown in Figure 5, where the applied stress intensity,  $K_1$ , is normalized to the respective fracture toughness values in air,  $K_x$ . (The subscripts refer to the type of loading mode.) The curves clearly show that the alloy is more susceptible to stress corrosion under the tensile loading mode.

To assure that these results were due to hydrogen, 10 ppm sodium arsenite ( $\text{NaAsO}_2$ ) was added to the solution. Arsenic is known to be a hydrogen recombination poison. It acts to slow the kinetics of the  $2\text{H}^+ + 2\text{e}^- \rightleftharpoons \text{H}_2(\text{g})$  reaction. In so doing, it not only slows the overall cathodic (and therefore anodic) reaction kinetics, but also allows for a greater hydrogen entry into the metal. Therefore, under the conditions encountered in these tests, one would expect to see a larger degree of embrittlement under those conditions where hydrogen caused the failure. Conversely, one would expect to see an increase in the stress corrosion life in those cases dependent on an anodic dissolution mechanism. Referring back to Figure 5, the type I loading mode clearly illustrates a hydrogen induced embrittlement. The type III mode failures however, appear to be controlled by one of the electro-chemical dissolution models previously mentioned.

Although the hydrogen model looks very appealing and is quite consistent within the references cited, additional verification is still required.

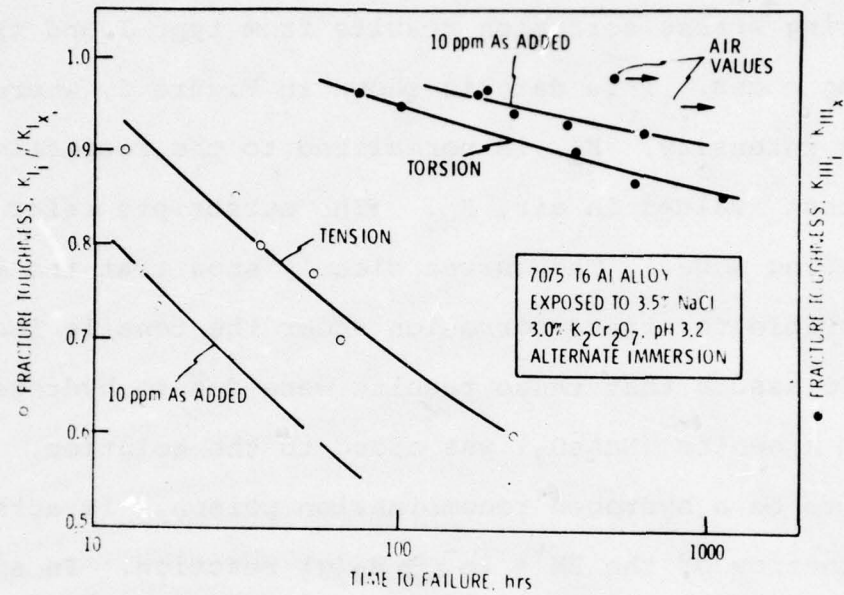


Figure 5

Susceptibility of 7075-T6 to SCC failures in mode I and mode III loading conditions (75)

Aqueous Corrosion Fatigue

The earliest aqueous fatigue work centered around the S-N behavior (applied stress versus number of cycles to failure curves) of the alloys. Pioneering work by Stubbington, Forsyth, <sup>76-79</sup> and co-workers showed that testing in 3%NaCl solutions produced a severe decrease from the air fatigue strength of DTD 683 (Al-5.8Zn-2.7Mg) and a high purity analog (Al-7,35Zn-2.55Mg). These investigators used reversed bending and torsional fatigue testing modes, and demonstrated that, the embrittlement phenomenon occurs in the solutionized, peak aged, and overaged states of the alloy. The most severe loss in strength, however, is found in the peak aged condition.

These early studies paid special attention to the fracture morphology of the alloy, and identified two distinct modes of crack propagation, the so-called type A and type B striations. The striations are characteristic markings which have been shown to delineate the length of crack extension per fatigue cycle.

<sup>76</sup> Stubbington characterized the type A, or ductile striations, as those found when the alloys are tested in air or at very high frequencies in more corrosive environments. The type B, or brittle striation, is favored by testing in the more corrosive environments or at low frequencies in laboratory air.

In an effort to formulate a model to explain the observed morphologies, Stubbington and Forsyth investigated the crystallographic relationships and slip patterns associated with both types of striations. The crystallography was identified through

the use of Laue back reflection X-ray patterns and etch pit  
76,77 techniques. Characteristic slip patterns were obtained by direct observation of the topography at the external surfaces. Additionally, the slip morphology at interior positions along the fracture surface was characterized by re-aging the specimens prior to sectioning. Using this procedure, the fatigue generated dislocation structure acted as preferential nucleation sites. After the application of a light etch, the newly formed precipitates acted to decorate the dislocation structure.

The type A striations were found to lie approximately normal to the tensile axis, and in general did not change this orientation as they crossed grain boundaries. They are, therefore, thought not to favor any specific crystal plane. Slip trace analysis showed that these striations were composed of nearly equal portions of shear mode and quasi-cleavage failures. It was formulated that the striation is formed by a combination of initial easy glide, followed by cross-slip generated quasi-cleavage.

21 This formulation was further extended by Bowles and Broek. These investigators used TEM and two stage carbon replication techniques to study the fracture morphology of air fatigued 7075-T6. The transmission foils were taken from the fracture surface and showed alternating sections of sparse and dense dislocation networks. Additionally, replicas taken from etch pitted portions of the fracture surface showed segments of  $\{111\}$ ,  $\{110\}$ , and  $\{100\}$  planes. It should be noted, however, that the majority of the etch pits were quite irregular in appearance. This would indicate that the majority of the fracture surface was not aligned parallel to a low

index face.

21

Bowles and Broek suggest that these findings may be interpreted in terms of slip plane shear. Initially only the most favorably oriented slip plane operates, giving rise to failure along  $\{111\}$  planes with a sparse dislocation sub-structure. As the crack grows, the resultant stress intensity rises, and additional slip systems become operational. The cross-slip leads to a dense dislocation network, and a fracture plane which is dependent on the specific orientations of the operating slip systems. For example, if the tensile axis was oriented such that two slip systems were equally favorable, and equal shear offsets occurred on both systems, then the resultant fracture surface must be symmetrically oriented between the slip planes. Simple geometric arguments show that this would be the  $\{100\}$  and  $\{110\}$  planes.

If, however, the orientation was such to provide unequal shear offsets on the slip planes, then the resultant fracture surface is no longer of the low index variety. Instead, the resultant fracture plane is determined by the geometric addition of the offsets from the operating slip systems. This results in a high index fracture plane which is dependent only on the net slip which occurs on the slip system, and therefore, of itself, is not characteristic of the fracture process. The fact that segments of all three low index planes were sighted, and that the majority of the fracture surface was of the high index variety, gives credibility to the model.

The type B striation, on the other hand, has been shown to lie

approximately on  $\{100\}$  planes. The four-fold symmetry of a  $\{100\}$  plane was found on a Laue back reflection pattern taken from a type B structure. In addition to this x-ray data, and the fact that Stubbington and Forsyth report  $\{100\}$  etch pits on the type B striations, the crystallographic nature of these striations is enforced by the fact that the fracture surface has a highly faceted morphology. The fatigue crack also shows definite changes in orientation as it crosses a grain boundary. (It is interesting to note that for 7075-T6 fatigued in liquid mercury, Wanhill reports that such crystallographic orientation changes can occur within a single grain.)

In addition to defining the crystallinity, the clarity of the individual Laue spots in the x-ray pattern also suggested that the striations are caused by a cleavage mechanism. Since cold work (i.e. dislocation motion) acts to diffuse the intensity of individual spots, patterns of such clarity are usually seen only in single crystals with very limited plasticity. The cleavage nature of the failure is also supported by the appearance of river lines along with the striations. These markings are usually taken to indicate a brittle failure mode. Finally, the slip pattern analysis done by Stubbington and Forsyth indicated that the striations were actually composed of large cleavage portions and rather small shear portions.

The type B striation is believed formed due to an environmentally induced cleavage, which becomes plastically blunted as the sharp cleavage crack runs out of the influence of the environment. Stubbington points out that Ryder has reported similar structures in hydrogen charged Armco iron (with the uncharged iron

76 showing ductile, type A striations). For that reason, Stubbington favored hydrogen adsorption as the cleavage producing phenomenon. He suggested that the hydrogen might act to either lower the surface energy for cleavage or promote dislocation pinning. The pinning would act to provide additional resistance to dislocation motion, and this could act to delay the onset of a shear mode failure.

In order to critically evaluate the crack morphology models, one should consider their implications concerning crack propagation rates. For example, the models discussed thus far indicate that brittle striations are caused by hydrogen induced cleavage, and therefore, ductile striations should form in the absence of the hydrogen. Since the crack growth rate of ductile striations is known to be less than that of brittle striations, one would expect increased growth rates under those considerations where appreciable hydrogen entry into the matrix is found.

81 The work of Spiedel and co-workers offers partial support for a hydrogen model. They investigated the role of electrolyte composition and electrochemical potential on the crack growth rates for a number of the 7000 series aluminum alloys. Using argon as a reference state, they found that aqueous environments do markedly increase the crack growth rates, and halide additions act to increase the rate over that found in distilled water. It should be mentioned that similar tests with ions that do not damage the oxide layer (i.e.  $\text{SO}_4^{=}$ ) showed no increase over the distilled water tests. This would support a hydrogen model since the presence of the oxide 69 is thought to reduce the hydrogen permeation rate.

In addition to varying the electrolyte content, these workers used a 5m KI solution to investigate the effects of electrochemical potential on the crack growth rate of 7079-T651. (Rest potential approximately -.9v vs SCE.) Using a  $\Delta K$  of  $3$   $20 \text{ Kg/mm}^2/2$ , they found that cathodic polarization to  $-1.65$  vs SCE acted to inhibit crack growth. Anodic polarization, however, acted to accelerate the rate until the pitting potential was reached (approximately  $-.6$ v vs SCE). Once pitting commenced, the crack growth rate became independent of the applied potential.

Additional crack growth versus potential behavior can be found in the work of Stolz and Pelloux. This work was performed on 7075-T6 in a 3%NaCl solution. The results of this study are in Figure 6. The figure suggests that the cathodic protection reported by Spiedel may only be applicable for low  $\Delta K$  levels (less than  $53 \text{ Kg/mm}^3/2$ ). For the larger  $\Delta K$  levels, the crack growth rate appears to be almost independent of the applied potential. At these levels, however, it should be noted that there does appear to be an increase in the crack velocity for potentials more cathodic than  $-1.4$ v.

When this increase at  $-1.4$ v is combined with the results of Troiano and Kaesche, it suggests that at these higher  $\Delta K$  levels, the corrosion fatigue response may be controlled by a hydrogen embrittlement phenomenon. Gest and Troiano report (see curve A, Figure 4) that for 7075-T6 under cathodic polarization conditions, appreciable hydrogen permeation does not occur until the polarization level exceeds the  $-1.4$ v level. Secondly, Berggreen and Kaesche (see curve d, Figure 4) have shown that for a similar

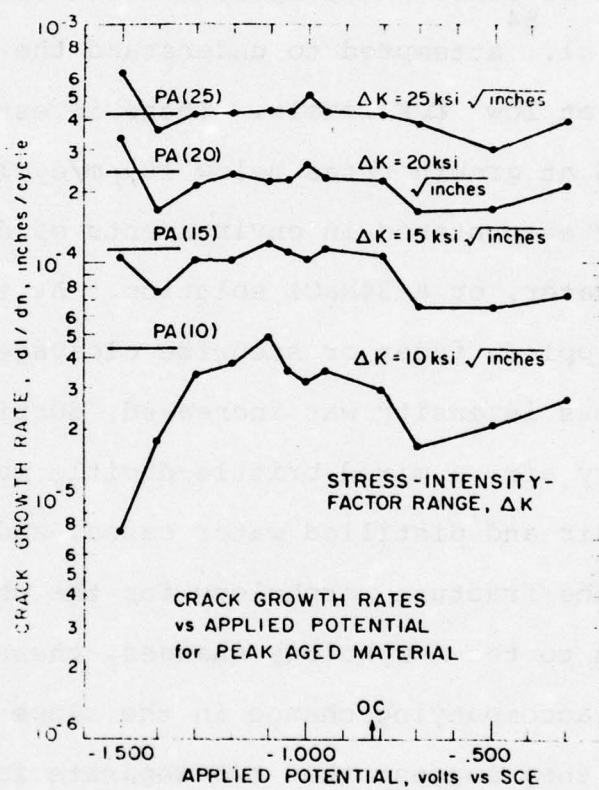


Figure 6

Fatigue crack propagation rates for 7075-T6 as a function of the applied potential (82).

alloy this rise in permeation correlates quite well with an increase in the stress corrosion velocity. Since Pelloux's work points towards a similar response, the hydrogen embrittlement model discussed earlier may also be applicable to the corrosion fatigue case.

Qualitative agreement with this supposition can be found in the work of other investigators. For example, the work of <sup>84</sup> Feeney, et.al. attempted to understand the corrosion fatigue phenomenon at low  $\Delta K$  levels. These investigators report that for 7075-T6 at growth rates below  $10\mu\text{m}/\text{cycle}$ , no fatigue striations were encountered in environments of dry air, moist air, distilled water, or a 3%NaCl solution. At these low growth rates, either a rippled, facet or stepwise cleavage appearance was found. As the stress intensity was increased, ductile striations were found in dry air; a mixed brittle-ductile morphology was seen in the moist air and distilled water cases, and brittle striations dominated the fracture morphology for the chloride environment. In addition to the morphology changes, these investigators also noticed an accompanying change in the slope of the  $da/dn$  curves. Therefore, they suggest that two separate failure modes are operational. In the low  $\Delta K$  range the fracture results from a strictly mechanical failure of the metal and no striational features were observed. For the high  $\Delta K$  levels, however, both the crack morphology and velocity are strongly affected by the environment. For the aqueous environments, activation energy considerations favor hydrogen as the embrittling species.

Additional support for a hydrogen mechanism can be found in  
51,85  
the corrosion fatigue studies of Duquette and co-workers.

In an investigation of the crack initiation process for 7075  
57  
aluminum tested in a 3% NaCl solution, Corsetti and Duquette  
found that the cracks always emanated from the base of a pit.  
By the nature of its topography, the pit would act as a very  
effective stress concentrator. Additionally, from an electro-  
chemical standpoint, the acidic nature (pH  $\approx$  3) of the electrolyte  
within the pit would provide a very effective source of hydrogen.  
Although this observation could not indicate the relative impor-  
tance of either effects, these investigators did suggest that the  
initiation process was the result of the joint effect of both the  
stress concentration and the hydrogen environment of the pit.

85  
In an attempt to verify the model, Jacko and Duquette per-  
formed a series of fatigue tests aimed at separating the relative  
importance of the two factors. The results of these tests are  
shown in Figure 7. Curve A represents the air fatigue results,  
and curve B represents the corrosion fatigue response in 3%NaCl.  
These curves can serve as reference states. In this sense, either  
the vertical (in terms of stress) or the horizontal (number of  
cycles) distance between the curves can be used as a qualitative  
measure of the embrittlement process. Curve C is obtained from  
specimens which were corroded for twenty-four hours (unstressed)  
and immediately fatigued in air. Therefore, this curve represents  
both the stress concentration and hydrogen embrittled case. Curve D  
represents specimens which were re-heat treated to a T6 temper  
(3 hours at 465°C, water quench, 24 hours at 120°C) after the same

24 hour pre-corrosion treatment. These specimens were also tested in laboratory air. The intermediate bake out acts to remove a portion of the internal hydrogen. (Additional tests indicate that at least 24 hours at 465°C are needed to remove all effects of the hydrogen). Therefore, since the pits act as stress concentrators in both curves C and D, the displacement of these curves can be taken as embrittlement due to the hydrogen removed during the bake out process. These tests indicate that a substantial degree of hydrogen embrittlement can occur during corrosion fatigue of these alloys in halide solutions.

This conclusion, however, is not held universally. For as indicated earlier, a number of other mechanisms have been proposed. These models vary from preferential dissolution of the crack tip to preferential ionic absorption. The preferential dissolution model was suggested to explain the observed increase in crack growth velocity during anodic polarization. It is difficult, however, to imagine how a dissolution process would be limited to specific crystallographic planes (i.e. {100}). The dissolution model also fails to explain the increased fatigue lives found in the bake out experiments.

The time dependent nature of the recovery process also acts to rule out any strictly adsorption models. Adsorption is a surface related phenomenon, and as such, the embrittlement process would be expected to disappear almost immediately upon heating to 465°C. Instead, the embrittlement process is seen to be partially reversible up to time periods approaching 24 hours. This behavior is, however, consistent with the hydrogen embrittlement phenomenon.

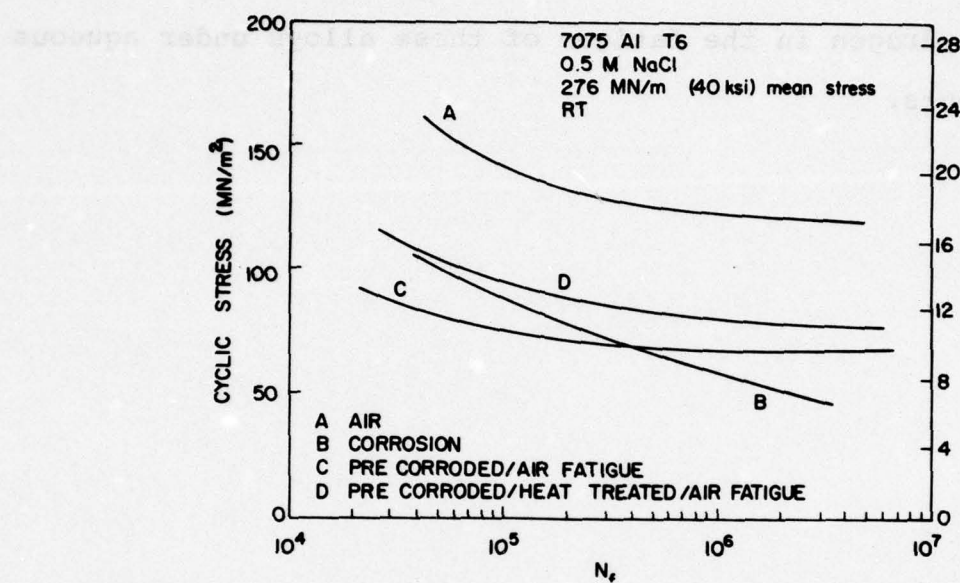


Figure 7

S/N curves for 7075-T6 aluminum illustrating the reversible nature of the hydrogen embrittlement process. The curves represent the fatigue response under the following conditions. (85)

- a. air environment
- b. .5N NaCl environment
- c. pre-corroded in .5N NaCl and immediately cycled in air
- d. pre-corroded, re-heat treated, and cycled in air.

In conclusion, the available evidence points toward a substantial role of the hydrogen embrittlement phenomenon in the corrosion fatigue failures of the 7075 type aluminum alloys. It is, therefore, the purpose of this investigation to study the role of hydrogen in the fatigue of these alloys under aqueous environments.

Experimental Program

A. Material Selection

In selecting the composition for the material used in this study, the prime consideration was to duplicate the mechanical and electrochemical properties of commercially available 7075 aluminum. In order to accomplish this objective, the four major elements (Al-Zn-Mg-Cu) of the system were used in the amounts prescribed for the commercial alloy.

In an effort to remove the large inclusion levels usually encountered in commercial 7075, a high purity analogue alloy was prepared for this study. The removal of the inclusions was desirable for a number of reasons. First of all, the inclusions are known to serve as nucleation sites for pits. In a mechanical sense, the pits have been shown to act as stress concentrators, the magnitude of which would vary dependent on the length of the test. In an electrochemical sense, the autocatalytic nature of the pitting process acts to isolate the base of the pits from electrochemical changes on the external surface. Along these same lines, Ateya and Pickering<sup>86</sup> have shown that depolarization occurs as one progresses into geometric defects, such as pits, and therefore, the electrochemical potential at the base of such a defect can be markedly different from that of the external surface. Since a great deal of the work in this study concerns testing specimens under potential control conditions, the uncertainty introduced by this depolarization is quite undesirable.

In addition, the inclusions act as barriers to grain boundary motion. This would impede any recrystallization of the alloy.

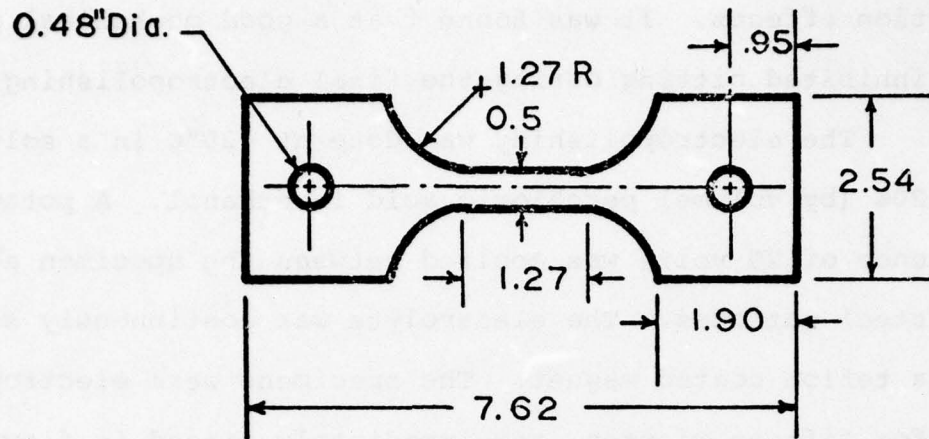
The recrystallization is used to provide an equiaxed structure, and under the proper conditions, (to be discussed later), secondary grain growth can be promoted. This provides a mechanism for obtaining specimens which contain a single grain throughout their gauge section.

B. Specimen Fabrication and Preparation

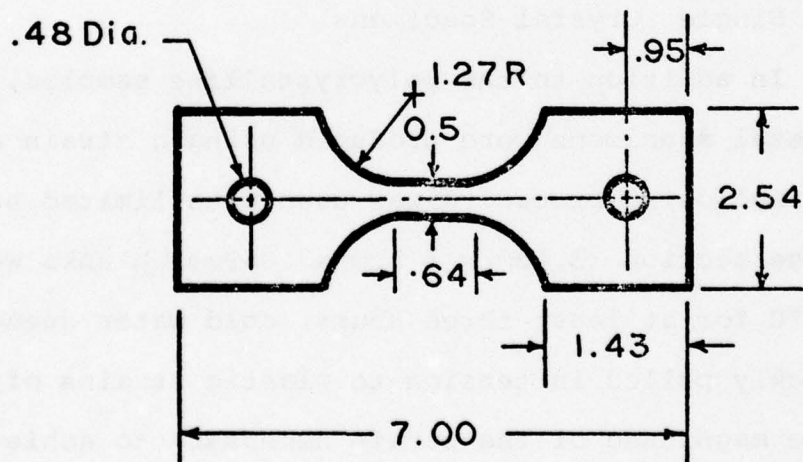
1. Polycrystalline Specimens

The high purity ingot of Al-5.5Zn-2.5Mg-1.5Cu was prepared by the Olin Metals Research Laboratories. Spectroscopic analysis of the ingot was performed to assure the desired composition of Al-5.5Zn-2.5Mg-1.5Cu. The ingot was homogenized and hot rolled by standard procedures, and was received as .25cm sheet. Additional cold rolling was performed at the General Electric Research and Development Center to produce sheet thicknesses of .089cm and .191cm. These sheets were cut longitudinally into specimens with a guage length of 1.27cm and a guage width of .5cm with a Tensilekut machine (Seiberg Industries, Danbury, Conn.). (See Figure 8a for the exact geometry.)

After the machining operation, specimens were solutionized for three hours at 465°C, cold water quenched, and aged for 24 hours at 120°C. In accordance with T-6 specifications, no substantial delay (greater than two minutes) was incurred between the quenching and aging process. The specimens were then mechanically polished on sequentially finer media from 400 grit silicon carbide to  $3\frac{1}{4}$  diamond paste. During the mechanical polishing, care was taken to gently round the



(a)



(b)

Figure 8

Specimen geometries used in this study

- a) Geometry for polycrystalline specimens.
- b) Geometry for single crystal specimens.

specimen corners. This was done to reduce stress concentration effects. It was found that a good mechanical polish inhibited pitting during the final electropolishing step.

The electropolishing was done at -20°C in a solution of 20% (by volume) perchloric acid in ethanol. A potential difference of 20 volts was applied between the specimen and stainless steel cathodes. The electrolyte was continuously stirred with a teflon coated magnet. The specimens were electropolished for fifteen minutes, and immediately rinsed in flowing tap water, ultrasonically cleaned in ethanol, and forced air dried prior to storage. The entire polishing procedure removed 5 to 8 mils in cross-section, and provided a uniform, stress-free reproducible surface.

## 2. Single Crystal Specimens

In addition to the polycrystalline samples, some single crystal specimens were produced using a strain anneal technique. The following procedure was used with limited success. Large gauge section (3.8cm x 5.1cm x .089cm) blanks were heated to 470°C for at least three hours, cold water quenched, and quickly pulled in tension to plastic strains of from 2% to 4%. (The magnitude of the strain necessary to achieve successful grain growth varied from master sheet to master sheet, apparently dependent upon the exact prior history.) After straining, the blanks were quickly resolutionized to 470°C for periods long enough to allow full grain growth. On successful attempts, (approximately one of four) the resultant grain size was quite large, with the grains measuring at least .65cm at their narrowest dimension.

Specimens were then tensilkut from the area of the blank which allowed for a reasonable grip section. Due to geometric constraints, the guage length of the single crystal specimen was .64cm and the width was .5cm (see Figure 86 for exact dimensions). Once machined, the single crystal specimens were subjected to the identical heat treatment and polishing procedures as outlined for the polycrystalline specimens.

C. Mechanical Testing

1. Tensile Testing

In an effort to assure that the mechanical properties of the polycrystalline specimens were within the T-6 specifications, a number of tensile tests were performed. The tests were conducted on specimens with a guage length of 1.27cm. Cross head speeds of .025cm/minute were used on a standard Instron machine. The resultant tensile properties are shown in Table II. As an additional check on the mechanical and metallurgical state of the alloy, an aging curve was developed. The curve, shown in Figure 9, plots the Vickers Hardness as a function of the aging time at 120°C. This curve agrees with similar curves of other investigators.

Tensile tests were also conducted on single crystal specimens. In this case the guage length was .64cm with the width .5cm. Two specimens were pulled to failure and both yielded stress-strain behavior characteristics of single slip behavior (see Figure 11a). Optical examination of the surface slip marking also indicated that only one slip system was operational. Although attempts were made to determine the tensile axis through

Table II  
Mechanical properties of the  
polycrystalline T-6 heat treated specimens

	<u>UTS</u>	<u>Y.S.</u>	<u>Elongation</u>
7075-T6	83	73	11
Al-5.5Zn-2.5Mg-1.5Cu-T6	82	72	12

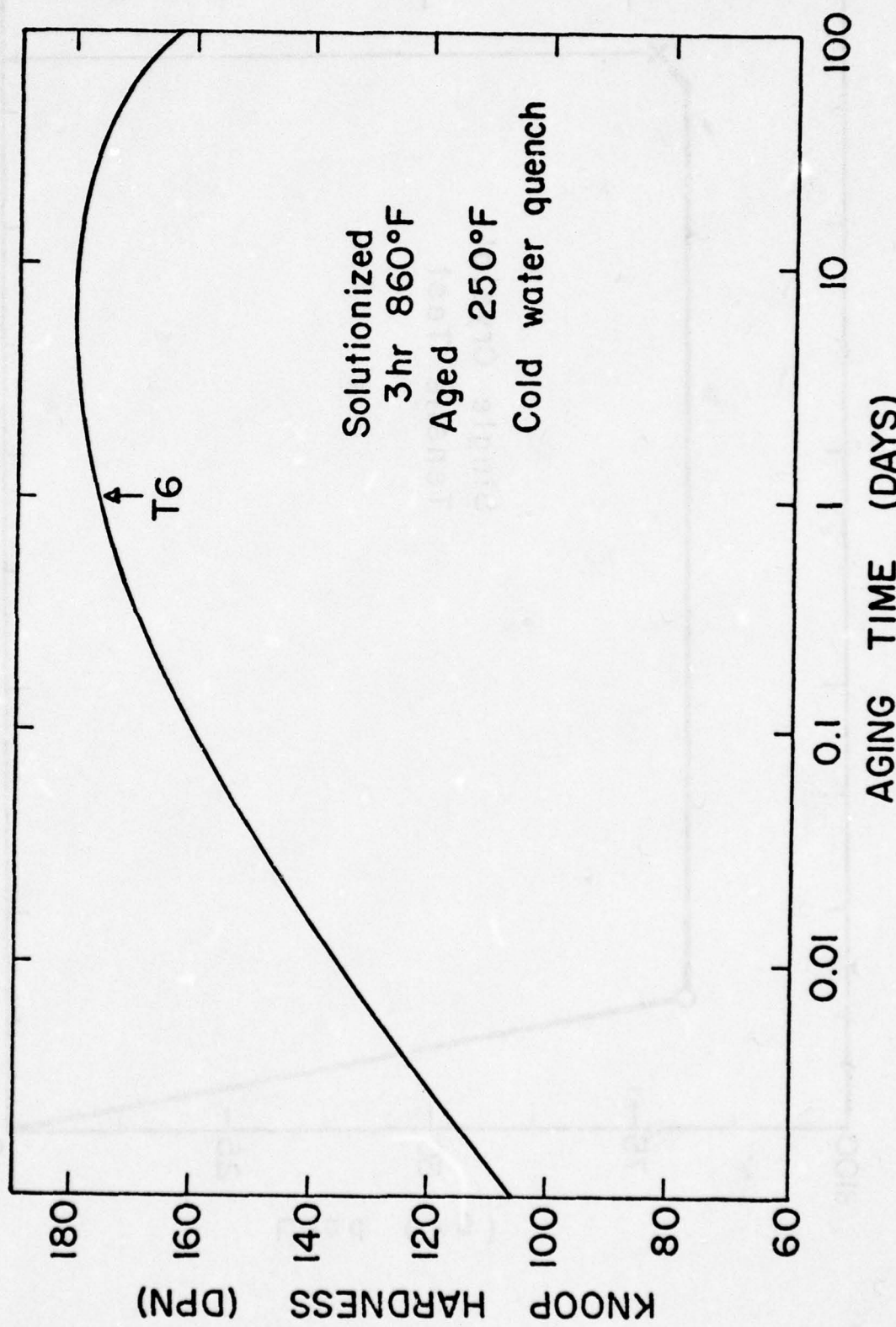


Figure 9. The hardness as a function of aging time at 120°C. Prior to the aging treatment, the specimens were solutionized for 3 hours at 465°C and cold water quenched.

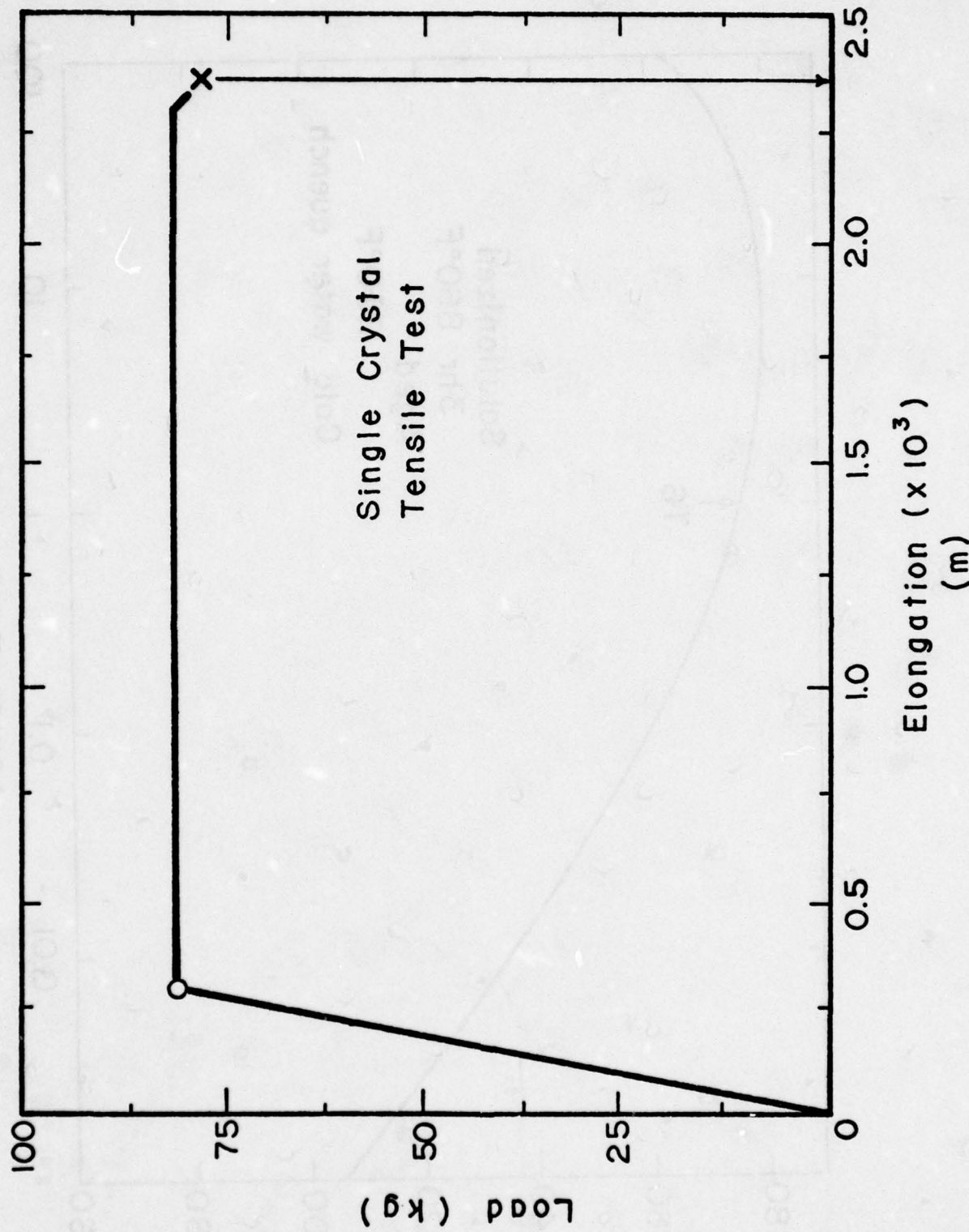
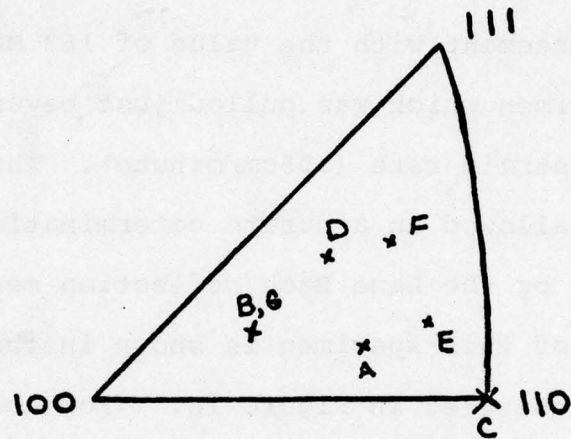


Figure 10. Single crystal data. (a) Load elongation curve for single crystal specimen pulled to failure; (b) Stereographic triangle orientations of all single crystal specimens used in this investigation.



(b)

Laue Back reflection techniques, the amount of deformation made both the individual spot intensity and its location too diffuse for accurate determination. If, however, one assumes a single slip tensile orientation of  $\langle 321 \rangle$ , then the critical resolved shear stress for these specimens is found to be 134.4 MN/m<sup>2</sup>. (An average of 141.1 MN/m<sup>2</sup> and 127.8 MN/m<sup>2</sup> for two tests at a cross head speed of .025cm/minute.) This is in excellent agreement with the value of 163 MN/m<sup>2</sup> determined for a third specimen which was pulled just beyond its yield point at a higher strain rate (.05cm/minute). This small amount of deformation allowed an accurate determination of a  $\langle 521 \rangle$  tensile axis by the Laue Back reflection method. The tensile orientation of this specimen is shown in the stereographic triangle illustrated in Figure 10. (For completeness, the tensile orientations of all the single crystals used in this study have also been included in this Figure.)

## 2. Fatigue Testing

Fatigue tests were conducted on both a Sontag SF-IU machine and an Instron closed loop, hydraulic machine. The bulk of the tests were tension-tension tests conducted on the Sontag unit. In this type of testing mode, the mean stress is always greater than the applied cyclic stress. Since the specimen is always under tensile loading conditions, thin specimens may be used without fear of buckling. The thin sheet geometry described earlier was used to maximize the exposed surface area. The small cross section acted to minimize any depolarization by always making the distance between the crack front and the bulk electrolyte relatively short.

In testing the polycrystalline specimens, all tests were performed with a 207 MN/m<sup>2</sup> mean stress. Tests were conducted in laboratory air and 3% NaCl environments. In the aqueous medium, a number of tests were conducted under constant potential conditions. A schematic illustration of the experimental apparatus used in these tests is shown in Figure 11a.

Initially, the re-circulation system was powered by a compressed air lift, (the details of which are described elsewhere), but later, a non-metallic drive pump was installed. In both cases, the flow rate was adjusted to empty the volume of the plexiglass chamber (approximately 500ml) at least once per minute. The potential was fixed by the use of either a Duffers Model 600 potentiostat or a Princeton Applied Research Model 173 Potentiostat.

Electrical connection to the specimen was made by a thin wire which was wound tightly through a small hole in the corner of the specimen grip section. The wire wrappings were coated with silver conductance paint to assure a good electrical connection, and isolated from the electrolyte through the use of Duco cement (trademark for E.I. duPont de Nemours and Co., Wilmington, Delaware) and Microshield, an acetone soluble lacquer (the Lea Mfg. Co., Waterbury, Conn.). The counter electrode was a platinum mesh screen attached to the inner diameter of the plexiglass cell. The specimen potential was measured against a saturated calomel electrode (E=-.2415v vs standard hydrogen electrode). (For that reason, all electrochemical potentials will be stated versus the saturated calomel electrode.)

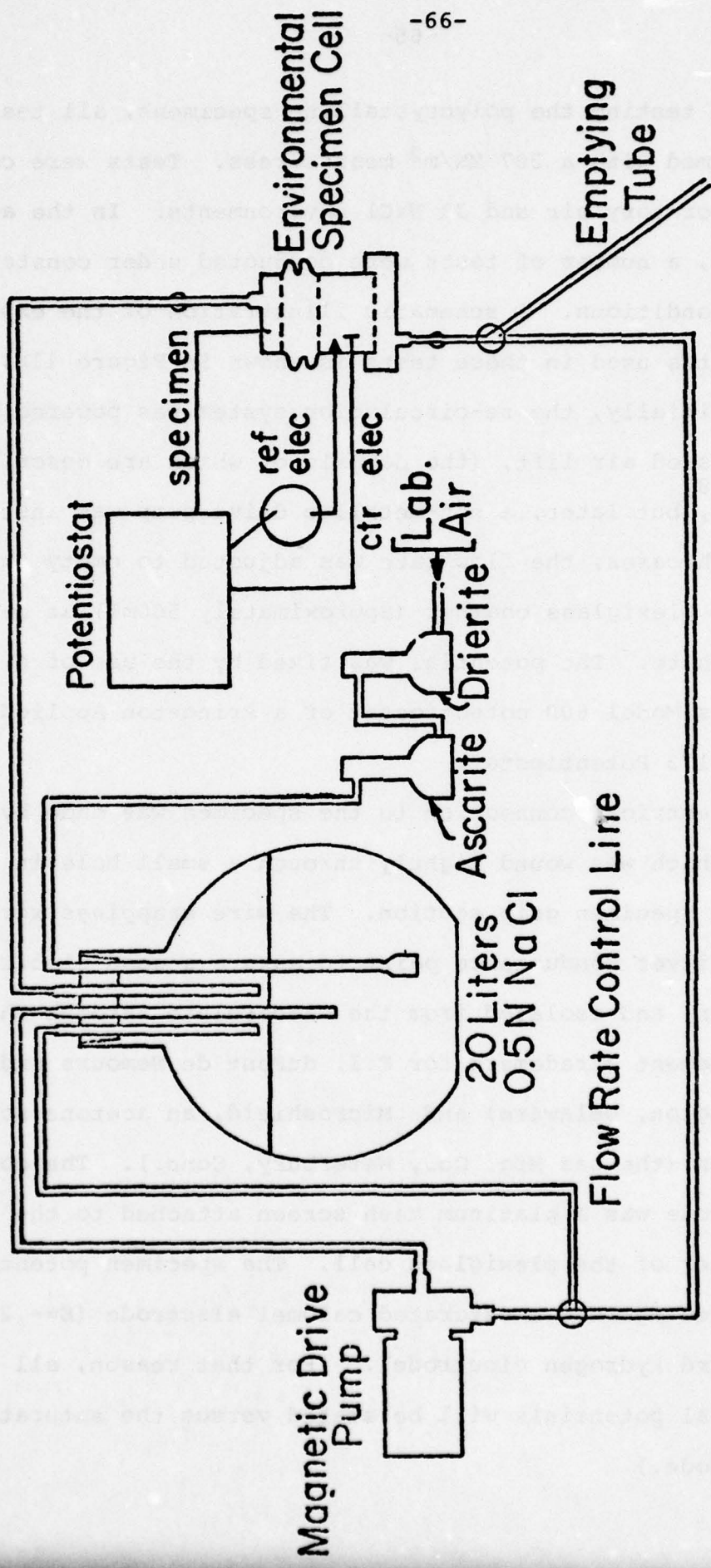
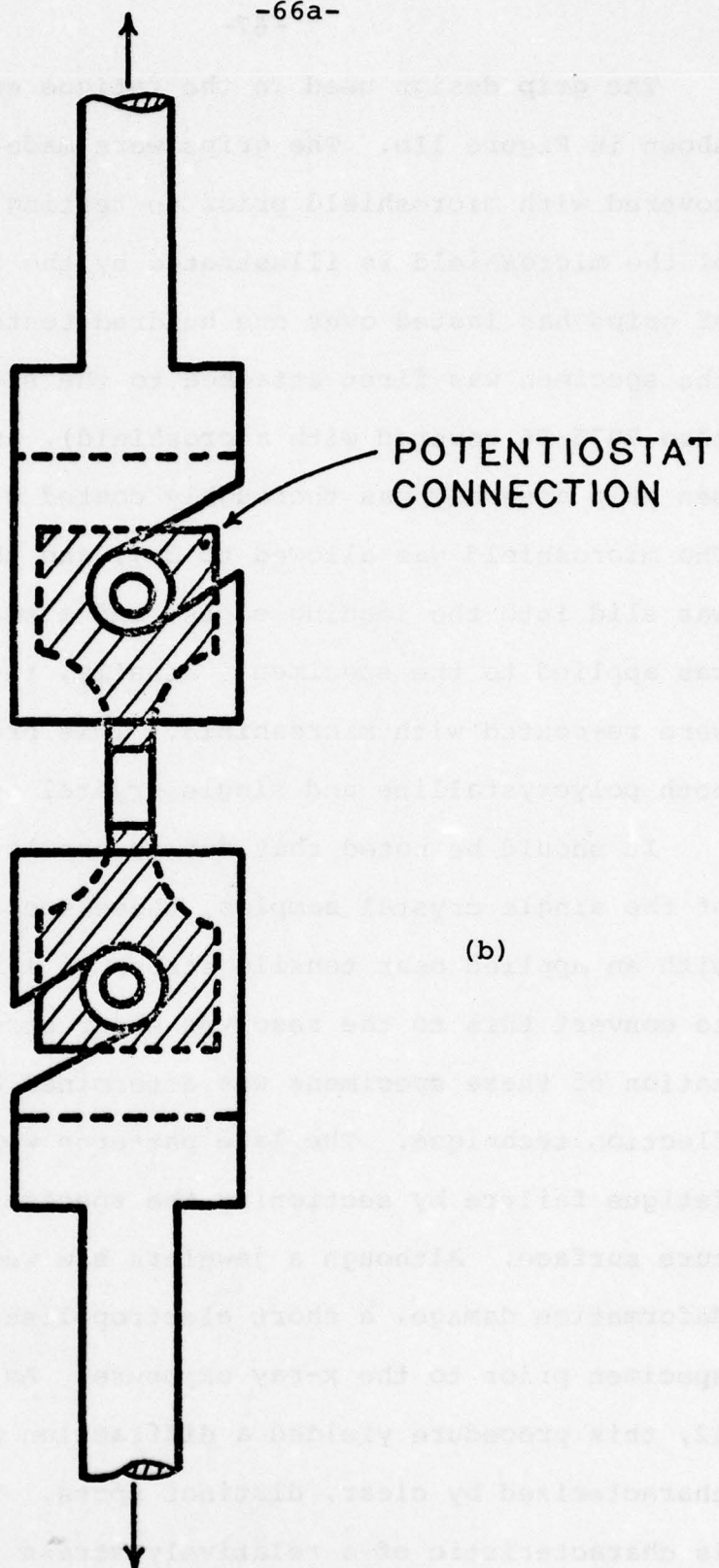


Figure 11. Schematic diagrams of the experimental apparatus used in environmental testing portions of this program.

- A schematic illustration of the environmental chamber, flow system, and electrical connections used in the corrosion fatigue testing program.
- A schematic diagram of the grip system used in the various mechanical testing procedures.



The grip design used in the fatigue experiments is shown in Figure 11b. The grips were made of 7075-T6 and covered with microshield prior to testing. The integrity of the microshield is illustrated by the fact that one set of grips has lasted over one hundred tests. Before loading the specimen was first attached to the sleeves (which were also 7075-T6 covered with microshield), and then the specimen grip assembly was thoroughly coated with microshield. The microshield was allowed to dry, and then the assembly was slid into the loading slots, and a small tensile load was applied to the specimen. Finally, the slot and sleeves were re-coated with microshield. This procedure was used for both polycrystalline and single crystal specimens.

It should be noted that due to the lower yield strengths of the single crystal samples, these specimens were tested with an applied near tensile stress of  $172 \text{ MN/m}^2$ . In an effort to convert this to the resolved shear stress, the tensile orientation of these specimens was determined by the Laue Back reflection technique. The laue patterns were obtained after the fatigue failure by sectioning the specimens just below the fracture surface. Although a jewelers saw was used to minimize the deformation damage, a short electropolish was given to each specimen prior to the x-ray exposure. As illustrated in Figure 12, this procedure yielded a diffraction pattern which was characterized by clear, distinct spots. This type of pattern is characteristic of a relatively strain free metal. As noted earlier, the individual tensile orientations are shown in Figure 10b.



Figure 12

An example of the Laue Back Reflection patterns used to orient the tensile axis of the single crystal specimens. The clarity of the individual spots is characteristic of a metal with very little deformation.

In addition to the stress controlled tests, an Instron closed loop machine was used for a number of strain controlled tests. Using a clip-on extensometer to monitor the strain, the tests were conducted in a tension-tension mode (.5%  $\pm$  .25% strain) on a specimen with a guage length of 1.27cm. In addition to noting the S-N behavior of this alloy, cyclic hardening curves were generated by following the stress-strain hysteresis curves as a function of the number of cycles. A single specimen was also tested in strain control prior to a stress relaxation test.

### 3. Stress Relaxation Measurements

A limited number of specimens were tested under modified stress relaxation conditions. The tests were performed on a standard Instron machine utilizing the grip and environmental systems just described. Tests were conducted on polycrystalline and single crystal specimens under environments of laboratory air, 3%NaCl, and 1N  $H_2SO_4$  plus .2N NaAsO<sub>3</sub>. In order to assure electrical isolation, the precautions outlined for the fatigue tests were also used in these tests. The specimens were pulled in tension to a point just over the macroyield stress, allowed to relax for a given length of time, and then re-pulled in tension. In all cases, load versus time curves were generated.

### D. Electrochemical Measurements

An electrochemical polarization curve was obtained for the T-6 condition of the alloy. The test was performed on aerated 3%NaCl, and a potential scan rate of 300 mv/hour was used. This curve is shown in Figure 13. It agrees with similar

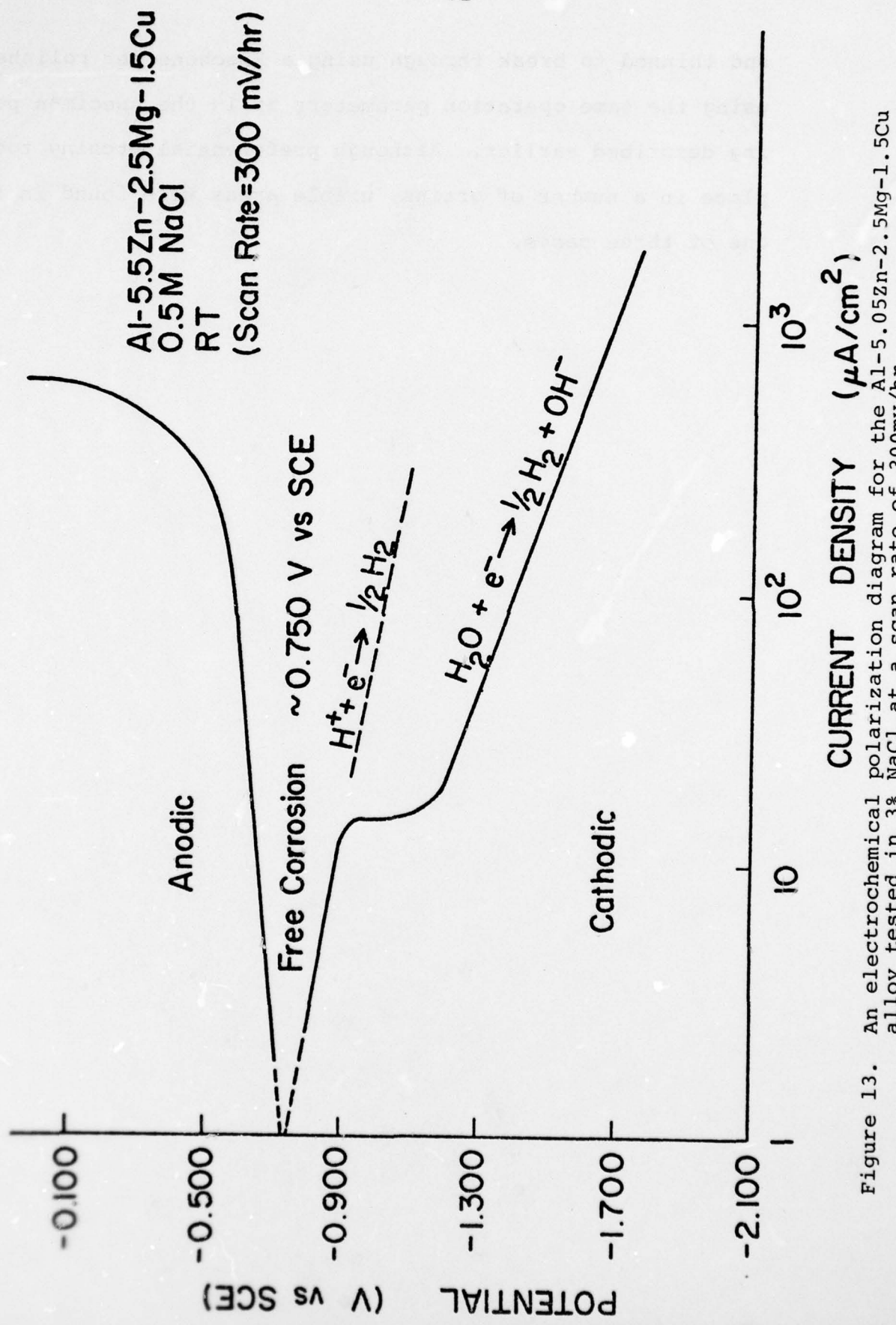
curves generated by other investigators. This experiment was performed using a Wenking model 66 TS-10 potentiostat.

E. Optical and Electron Microscopy Observations

Optical microscopy was primarily used to monitor the nature of the corrosive attack on the external surface. The scanning electron microscope was used to record the fracture morphologies of the alloy. Low magnification observations were used to quantify (on a percentage basis) the extent of penetration for the various morphologies. High magnification observations were used in attempting to understand the fracture phenomenon.

The transmission electron microscope was used in a two-fold manner. Two-stage carbon replicas of the fracture surface were used as additional verification of the fracture morphologies found in the SEM. Additionally, the TEM was used to observe the grain boundary and deformation structure of the alloy. Attempts were made to correlate the deformation substructure with the various environmental parameters. Under load control, the deformation was apparently very localized and no fatigue generated substructure could be found in the gauge sections of fractured specimens. To overcome this problem, TEM observations were made ahead of the crack tip for an air and cathodically charged specimen.

In all cases, specimens were thinned using the following technique. The sections were first mechanically polished to a thickness of .1mm, with the final mechanical polish being a  $3\mu$  diamond paste. Discs were then punched from these sections



and thinned to break through using a Fischone jet polisher, using the same operation parameters as in the specimen polishing described earlier. Although preferential etching took place in a number of grains, usable areas were found in about one of three cases.

## Results

### A. Material Characterization

Optical and transmission electron microscopy were used to characterize the metallurgical state of the heat treated alloy prior to testing. Optical examination revealed a re-crystallized grain structure. Equiaxed grains of about .1mm diameter were found. Both the grain boundary and matrix precipitate structure were too fine for optical resolution. To alleviate this problem, thin foils of the heat treated material were prepared for the TEM. A micrograph characteristic of the grain boundary structure is shown in Figure 14a. The figure clearly illustrates discrete, non-continuous particles of nearly uniform size. It should also be pointed out that no precipitate free zone is found. Extensive examination of all foils failed to produce any evidence of a p.f.z. This observation is consistent with the data of Embury and Nicholson cited earlier.<sup>10</sup> Additionally, the matrix precipitate structure is found to be too fine for accurate characterization. This is consistent with the dimensions reported from various x-ray studies.

Although the particle size is small, no quenched in precipitate inhomogeneities, as suggested by Laird and Thomas were ever observed.

TEM examination did, however, reveal a quenched in dislocation structure. This helical structure, as illustrated in Figure 14b is characteristic of the alloy. The helices are thought to arise due to a supersaturation of vacancies along screw dislocations. The supersaturation arises due to a change

in the equilibrium concentration of vacancies caused by the quenching process.

Electrochemical characterization experiments were also conducted on the heat treated (T6) alloy. A polarization curve (applied potential versus current density) was developed for the aerated .5N NaCl solution used in the fatigue portion of the experimental program. The curve, which was presented in Figure 13, represents the kinetic response of the alloy.

In this sense, the shape of the curve can be used to gain information concerning the reactions which occur at the specimen surface. For example, in the anodic portion of the curve (potentials more positive than the rest potential of -.75v), a single anodic dissolution reaction is seen to take place. The overall anodic reaction is thought to be  $\text{Al} \rightleftharpoons \text{Al}^{+++} + 3 e^-$ . On the cathodic portion of the curve (potentials more negative than the rest potential), two separate reactions are present. From the rest potential to potentials near - .95v, a linear increase in log (current density) is found with the increasing cathodic potentials. This is thought to be the Tafel-like behavior associated with the reduction of the hydrogen reaction. Low current densities are encountered in this portion of the curve, and the only noticeable reaction is a slight tarnishing of the specimen surface. In the range from -.95v to -1.3v, the reaction becomes diffusion limited, and a limiting current density of 15 a/cm<sup>2</sup> is approached.

Cathodic polarization beyond the -1.3v level initiates the reduction of water. This reaction is accompanied by profuse



Figure 14

TEM micrographs illustrating the initial metallurgical state of the heat treated alloy.

- a) An electron micrograph showing the structure of the grain boundary region (50,000x)
- b) An electron micrograph showing the quenched-in, helical dislocation structure. (20,000x)

amounts of hydrogen gas bubbling off the specimen surface, and hydroxide attack of the specimen surface. The caustic attack rapidly produces a porous, black reaction product on the metal surface. The porosity of the film was confirmed by polarizing a specimen to -1.75v for twenty-four hours, and noting that no change occurred in the resultant current. This indicated that the increasing thickness of the film offered no diffusion barrier to the electrochemical reactions at the electrode.

In an effort to determine the corrosion rate under open circuit conditions, both linear polarization and weight loss measurements were used. The linear polarization adopted was that suggested by Oldham and Mansfield. Polatization levels of  $\pm 5$  mv and  $\pm 10$  mv were used, and a free corrosion rate of approximately  $10 \mu\text{a}/\text{cm}^2$  was found. Weight loss measurements were conducted for 24 and 168 hours, and they indicate a free corrosion rate equivalent to  $20 \mu\text{a}/\text{cm}^2$ . It should be noted that the free corrosion rate indicates the magnitude of both the anodic and cathodic current during open circuit conditions. In contrast, the magnitude of the polarization curve indicates the overall net current flow in the circuit.

**B. Fatigue Testing**

1. Polycrystalline Specimens - Air

Initial tests were conducted in laboratory air in an effort to establish a baseline S-N curve for this material. A  $207 \text{ MN/m}^2$  mean stress was selected in order to alloy the tension-tension testing mode to be used under all environmental conditions.

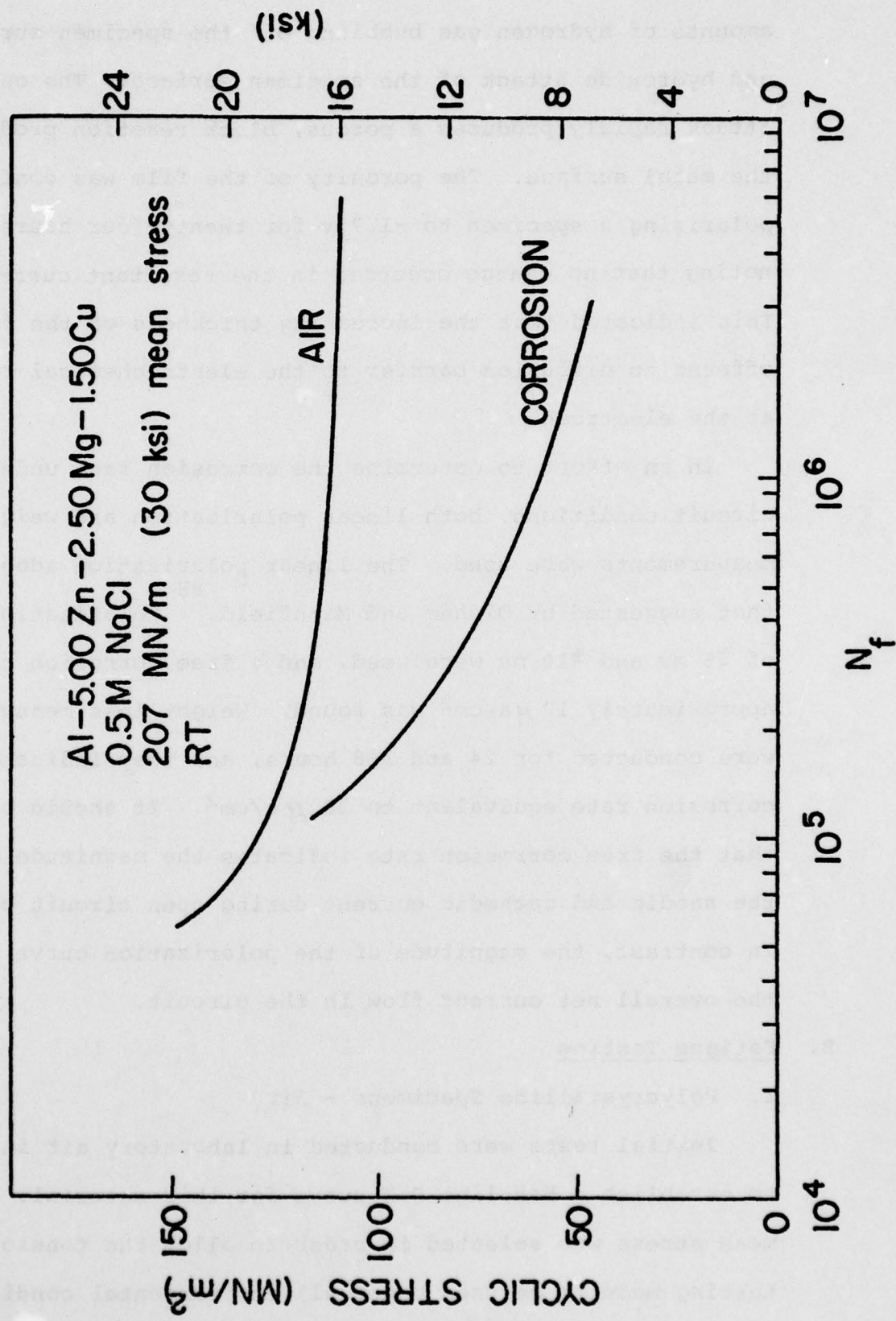


Figure 15. The S-N behavior of polycrystalline, T-6 specimens test in air and .5M NaCl.

The results of these load controlled tests are shown in Figure 15. (The aqueous results will be discussed later.) The air curve shows a  $10^7$  air endurance limit of approximately  $207 \pm 110$  MN/m<sup>2</sup>.

SEM examination of the fracture surface revealed a transgranular failure morphology. A characteristic fracture surface is shown in Figure 16. The crack initiates at an external surface and river lines emanate inward in a radial fashion. The markings on these surfaces are rather feathery in appearance. This is due to multiplication, or branching of individual river lines, and has been suggested to represent a "ductile" failure mode for this alloy. (It should be noted that the term ductile is used in a relative sense, and "less brittle" is probably more appropriate.)

A more detailed view of the fracture surface is provided through the use of two-stage carbon replicas. Using this technique, the two characteristic fracture features were found. Figure 17 is representative of the markings found close to the initiation site. The wavy markings running perpendicular to the river lines have been characterized by Feeney, et.al.,<sup>84</sup> as rippled type fracture morphology. As in their study, these markings were only found in low stress intensity areas (near the initiation site) and are thought to result from a mechanical rather than environmental type failure. As one progresses further into the specimen, the slip markings replaced markings similar to the ductile, type A striations seen by Stubbington and Forsyth. These markings are shown in Figure 17, and are

characteristic of air fatigue failures in these alloys.

Figure 17c illustrates a region with very narrow striation spacings. This structure is thought to characteristic of a transition between 17a and 17b.

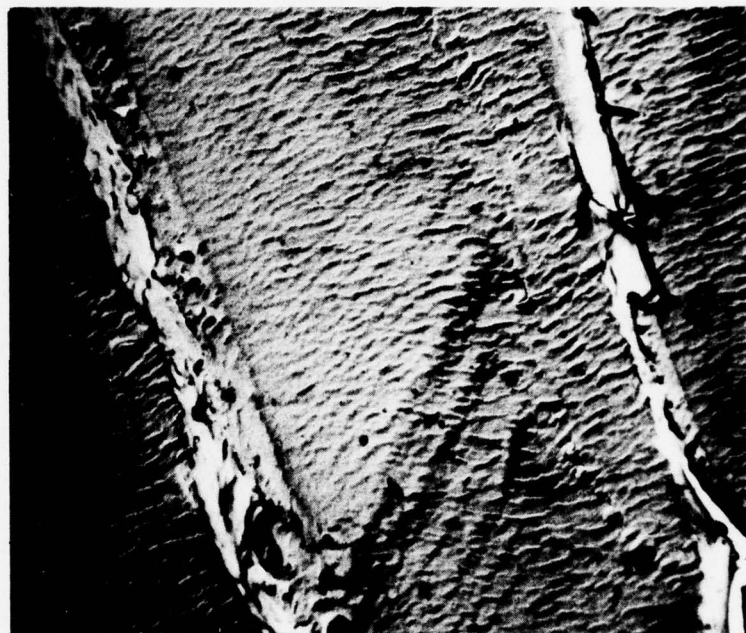
In an effort to characterize the air fatigue process, attempts were made to obtain the dislocation substructure associated with the phenomenon. TEM examination of thin foils taken from the guage sections of fatigue fractured specimens revealed only the helices characteristic of the undeformed metal. This indicated that the deformation associated with the fatigue structure was very localized. This fact was supported by the fact that fracture in these specimens was associated with a single crack. No secondary cracking was observed in the air fatigue case.

In an effort to overcome these obstacles, a pre-notched specimen was fatigued until a crack had propagated partially across the guage section. The fatigue process was stopped and a thin foil was taken containing the crack tip. TEM examination of this foil revealed the characteristic fatigue substructure shown in Figure 18. The planar slip bands are seen to interact with grain boundaries in two ways. Most boundaries act as effective barriers to dislocation motion. Therefore, whenever a slip band intersects such a boundary, it produces a large strain field across the boundary and into the next grain. This process is clearly illustrated in Figure 18. Occasionally, boundaries were found which offered little resistance to the dislocations. This is shown in Figure 18b.



Figure 16

A characteristic SEM micrograph  
of the fracture surface taken from  
a specimen tested in laboratory air (100x)



a

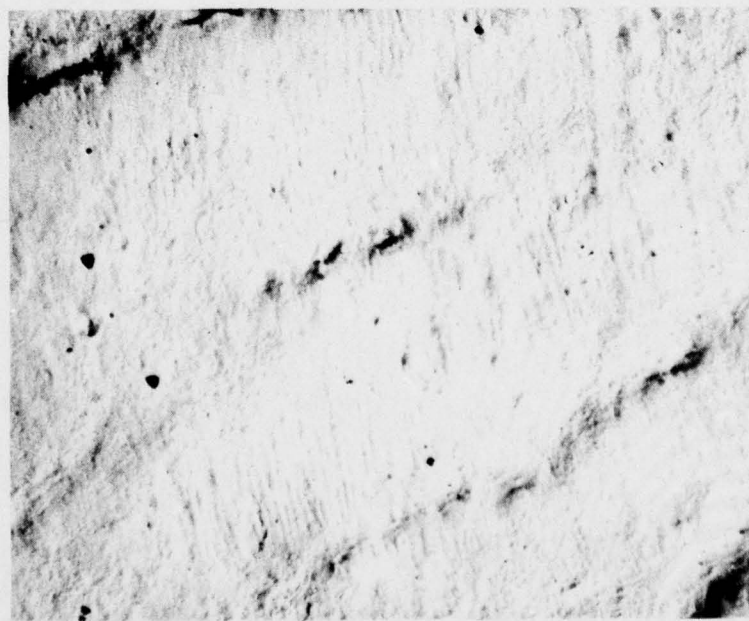
Figure 17

Two stage carbon replicas taken from the fatigue fracture surface of a laboratory air test.

- a) A rippled type fracture morphology found near the initiation site. (8500x)
- b) Ductile striations characteristic of the later stages of crack propagation (5000x)
- c) An area illustrating the early stages of striation formation. (8500x)



**b**



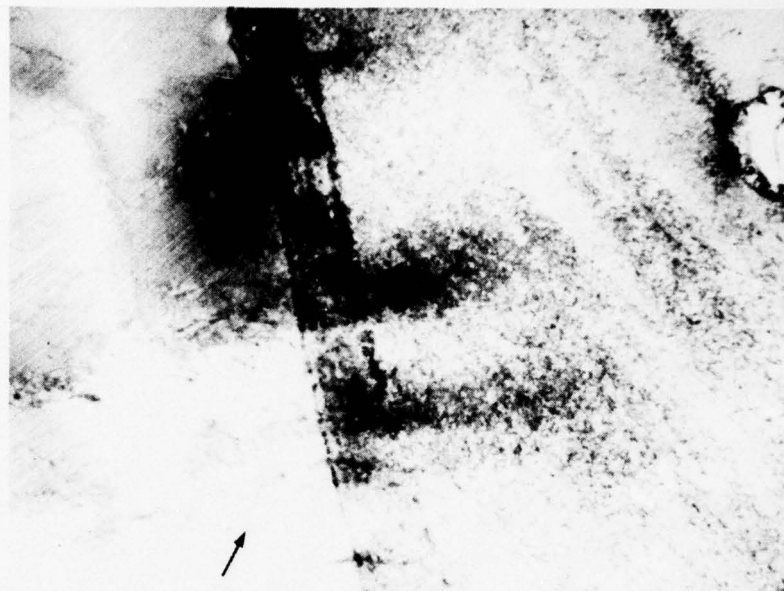
**c**

Note the slight angular change as the boundary is crossed. In this case, the intersecting slip band initiates only a small degree of dislocation motion in the adjacent grain. Although no quantitative measurements were taken, it is suggested that the type of dislocation interaction may be controlled by the degree of misorientation across the boundary.

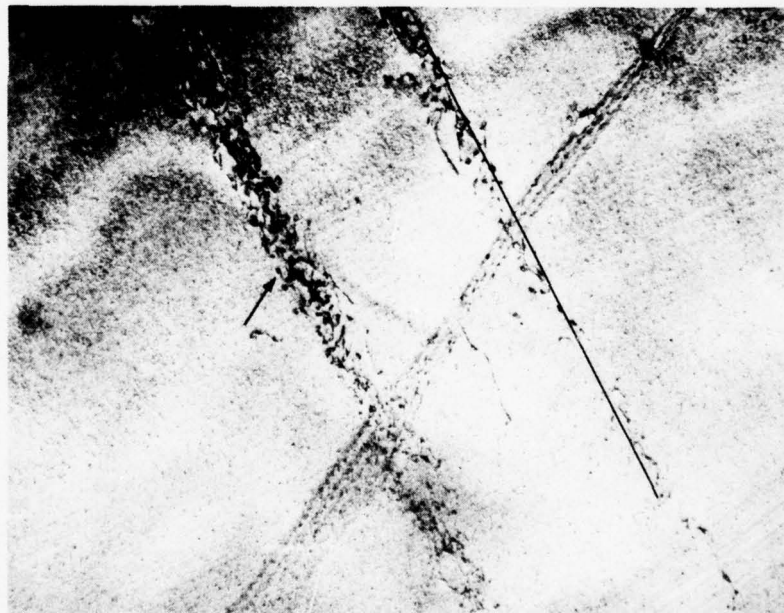
In addition to noting the grain boundary interactions, it was hoped to clarify the dislocation structure within the slip band. The high degree of deformation in the crack tip foils made resolution of specific features within the slip band quite difficult. Some individual dislocation loops were visible, however, and these are marked with arrows in Figure 18.

Although these isolated loops were observed within the slip band structure, it was felt that more definitive evidence should be found to characterize the slip band structure. In an effort to provide uniform deformation throughout the guage section, (and thereby make characteristic slip bands easier to locate) a series of strain-controlled fatigue tests were conducted. Using a clip-on extensometer to control the ram location of the hydraulic machine, specimens were cycled at strains of  $.5\% \pm .25\%$ . This produced a fatigue life of 15,000 cycles.

Thin foils were taken from the guage section of a fractured specimen and examined in the TEM. In contrast to the crack tip foil, these foils produced slip bands in various stages of formation. Figure 19 shows adjacent slip bands in different stages. The slip band labeled A is near saturation. In this condition



**a**



**b**

Figure 18. The dislocation substructures found near the tip of an air tested fatigue crack

(a) The dislocation interaction with a grain boundary showing the large strain field associated with each slip band (10,000x)

(b) The dislocation interaction with a grain boundary illustrating the relatively strain free passage of a slip band into an adjacent grain (16,000x)

AD-A077 461

RENSSELAER POLYTECHNIC INST TROY N Y DEPT OF MATERIALS--ETC F/G 11/6  
THE CORROSION FATIGUE BEHAVIOR OF A HIGH PURITY AL-ZN-MG-CU ALLOY--ETC(U)  
NOV 79 E F SMITH, D J DUQUETTE

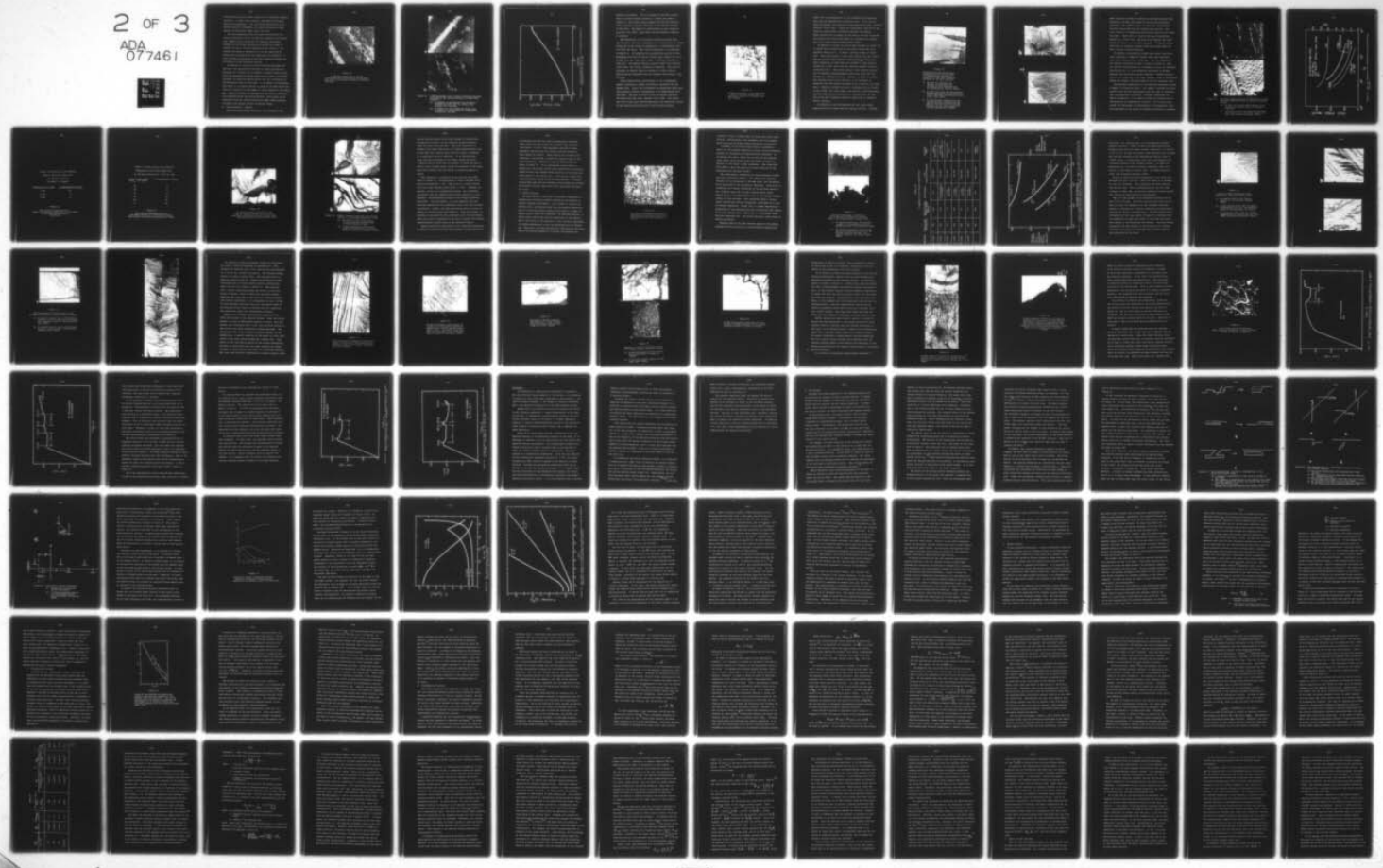
N00014-75-C-0466

NL

UNCLASSIFIED

2 OF 3  
ADA  
077461

12



the accumulated strain makes resolution of individual features difficult. In some areas, however, individual dislocation loops are recognizable. The slip bands labeled B are at an earlier stage of development and clearly illustrate a high density of dislocation loops within the band.

The loops apparently form by either the pinch-off of a single dislocation line or through the interaction of dislocation segments which are pinned on different slip planes. Examples of the single dislocation pinch-off are shown in Figures 20a and b, and are indicated by the letter S. The multiple dislocation interaction is clearly supported by Figure 20b and examples of this phenomenon are labeled M. A more thorough presentation of the loop formation process will be deferred to the discussion section.

In addition to using the strain-controlled specimens for TEM work, the stress-strain behavior of these specimens was monitored as a function of the number of applied strain cycles. Since the specimen was tested under strain control, the stress necessary to reach the desired strain acts as a reflection of the mechanical state of the alloy. In an effort to consolidate this data, it is usually plotted in terms of the peak stress per cycle as a function of the number of cycles applied to the specimen. Figure 21 clearly illustrates that the alloy is mechanically hardened during the fatigue process. This result is inconsistent with the various precipitate shear models proposed to explain the fatigue failure of similar alloys.

## 2. Polycrystalline - Aqueous

Load controlled fatigue tests were also conducted under

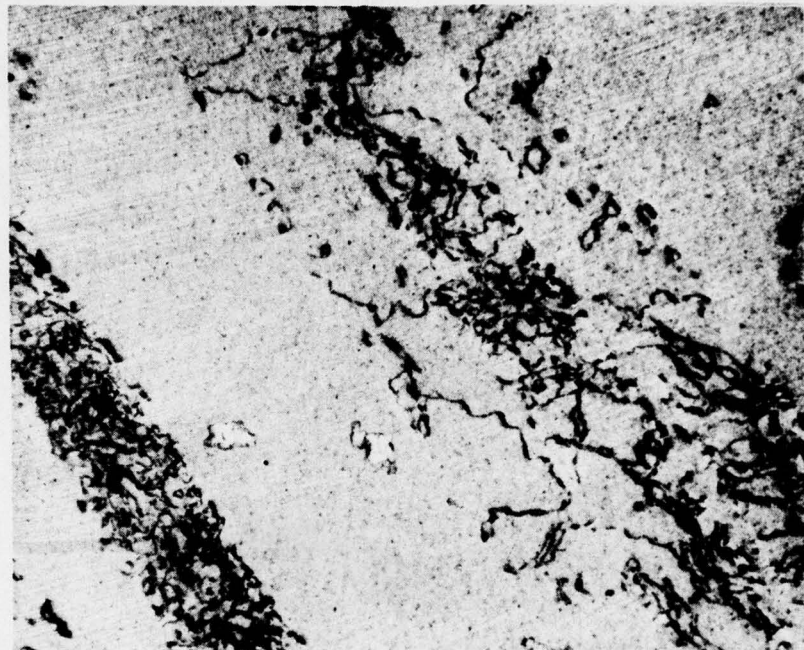


Figure 19

A TEM micrograph from a strain cycled specimen illustrating two adjacent slip bands in different stages of formation (20,000x)

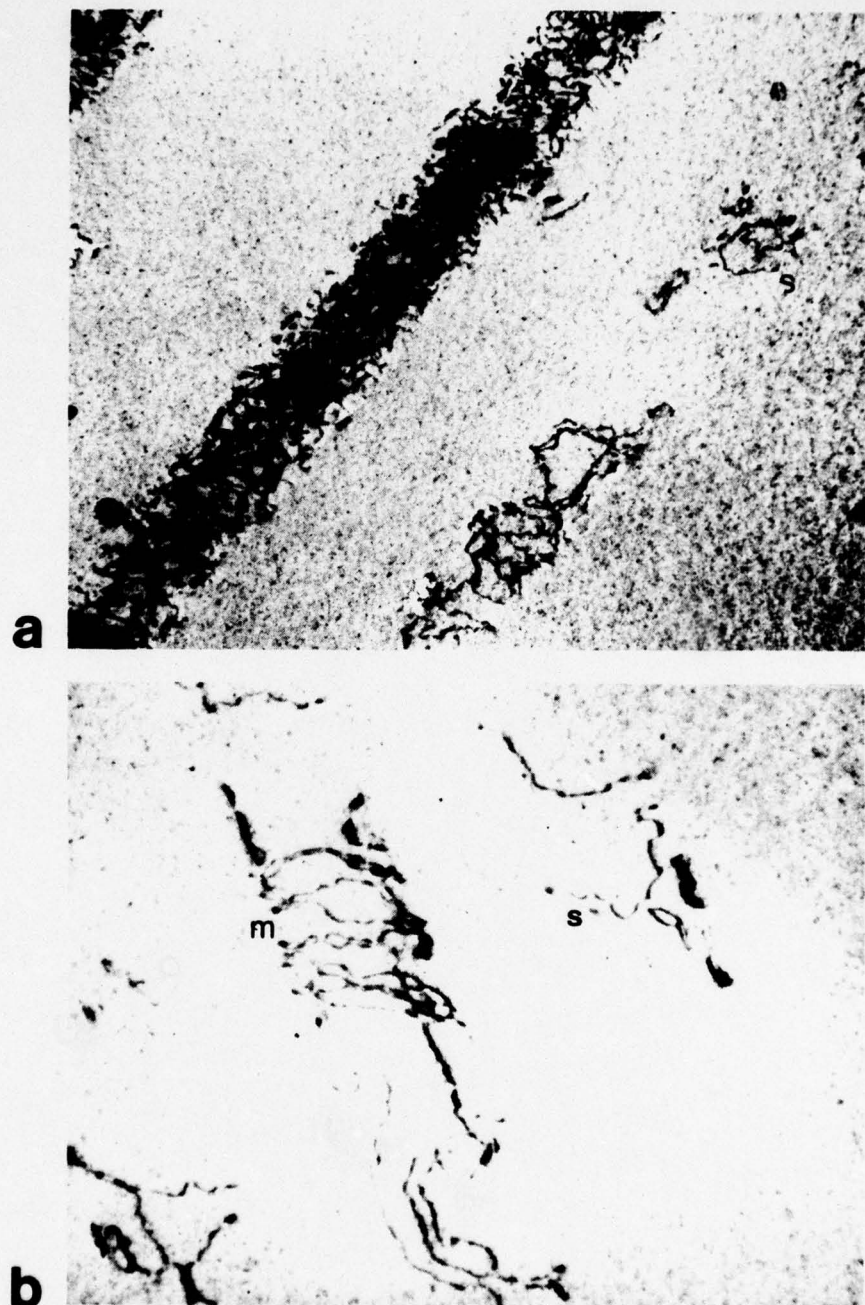


Figure 20. A TEM micrograph from a strain controlled specimen illustrating the various methods of dipole loop formation.

(a) An example of dislocation loop formation through the pinch off of a single dislocation (S) (15,000x)

(b) An example of loop formation though both a single (S) and multiple (M) dislocation interaction (26,000x)

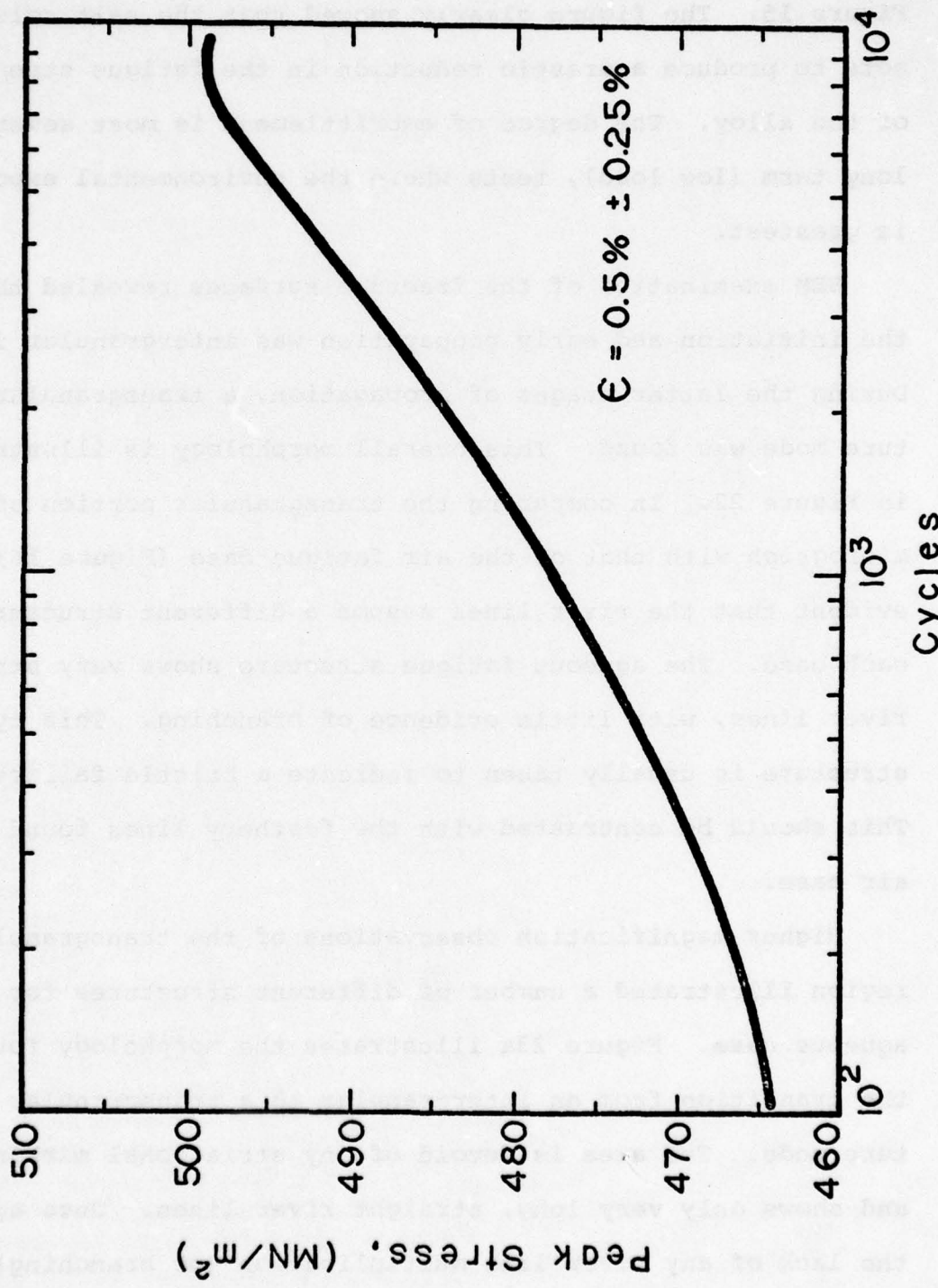


Figure 21. A cyclic hardening curve for a T-6 specimen fatigued in laboratory air at  $.58 \pm .25\%$ .

aqueous environments. The S-N response of the heat treated alloy to tension-tension fatigue in .5N NaCl was shown in Figure 15. The figure clearly showed that the salt solution acts to produce a drastic reduction in the fatigue strength of the alloy. The degree of embrittlement is most severe in long term (low load), tests where the environmental exposure is greatest.

SEM examination of the fracture surfaces revealed that the initiation and early propagation was intergranular in nature. During the latter stages of propagation, a transgranular fracture mode was found. This overall morphology is illustrated in Figure 22. In comparing the transgranular portion of this micrograph with that of the air fatigue case (Figure 16) it is evident that the river lines assume a different structure in each case. The aqueous fatigue structure shows very straight river lines, with little evidence of branching. This type of structure is usually taken to indicate a brittle failure. This should be contrasted with the feathery lines found in the air case.

Higher magnification observations of the transgranular region illustrated a number of different structures for the aqueous case. Figure 23a illustrates the morphology found near the transition from an intergranular to a transgranular fracture mode. The area is devoid of any striational markings, and shows only very long, straight river lines. Once again, the lack of any river line multiplication (or branching) points to the severely brittle nature of the fracture process.



Figure 22

An SEM fractograph illustrating the overall fracture morphology of a specimen tested in a .5N NaCl solution (100x).

Figure 23b is characteristic of the transgranular morphology away from the intergranular initiation site. As in the previous micrograph, the fracture is characterized by long, straight, "brittle" river lines. Figure 23c illustrates a portion of the fracture surface where striational markings are present. These markings are an example of the type B, brittle striations, and usually occur after some degree of transgranular propagation (i.e. higher stress concentration areas.)

In addition to noting the striational markings of Figure 23c, it should also be noted that as the crack crosses the grain boundary (marked g.b.), it shows a distinct change of direction. This sharp change in crack path implies that the cracking process may follow specific crystallographic directions.

77

(This assumption is consistent with Forsyth's Laue patterns indicating a (100) crack path for corrosion fatigue cracks in a similar alloy). The brittle nature of the fracture process and the apparent crystallographic crack path imply that the failure is a cleavage fracture. However, in order to confirm the cleavage nature of the fracture, it is necessary to establish that the fracture proceeds along a specific low index plane. Empirical evidence for such a statement was not found in this study. For that reason, this brittle, crystallographic fracture mode will be referred to as cleavage-like, and any use of the work "cleavage" should be taken only to signify a brittle fracture.

In addition to the SEM examinations, two stage carbon replicas were also taken from the fracture surface. Although

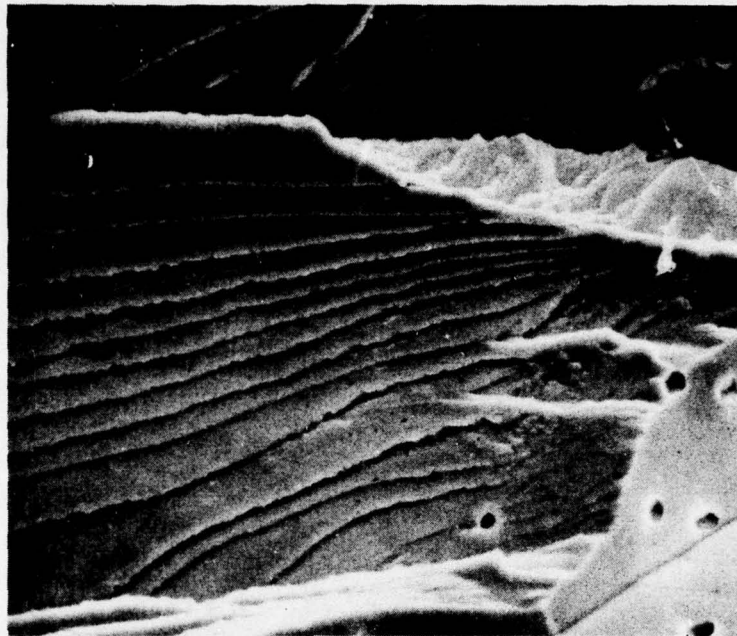


Figure 23

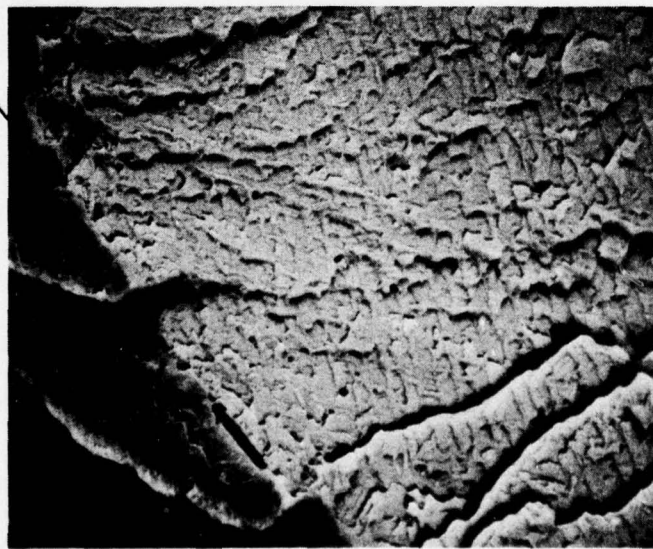
Characteristic SEM micrographs illustrating the various modes of transgranular failure encountered in the free corrosion failures in .5N NaCl solution.

- a) An area of cleavage-like failure illustrating the transition from intergranular to transgranular failure (500x)
- b) An area away from the intergranular initiation region devoid of striational markings and exhibiting only river lines (500x)
- c) An area further removed from the initiation site illustrating the Type B, brittle striation characteristic of the later stages of fatigue propagation (1000x).



**b**

**GB**



**c**

these replicas provided no additional information beyond that obtained by the SEM, they acted to confirm the structures presented. For example, Figure 24 shows the striationless structure associated with the cleavage type failure. The river lines act to demonstrate the brittle nature of this fracture mode. Figure 24b is a view of the type B striations adjacent to a river line. The back lines indicate the crack growth per cycle (i.e. striation spacing). It should also be noted that no secondary fatigue cracks were found under the free corrosion testing condition.

In addition to performing fatigue tests under free corrosion conditions, a number of fatigue tests were performed under controlled potential conditions. The S-N response of the cathodic polarization tests is shown in Figure 25. (The air and free corrosion data is included as a point of reference). Polarization at -1.3 volts showed no difference in fatigue behavior from the free corrosion condition. Further polarization to -1.5 volts and -1.75 volts, however, acted to drastically reduce the fatigue life below that of the free corrosion case.

Fractographic examination of the polarized specimens yielded a number of interesting facts. For example, although the polarization level did not appreciably alter the type of structures seen (intergranular initiation, "cleavage" morphology and type B striations), it did tend to change the relative mix of intergranular to transgranular fracture. For a given cyclic stress, the percentage of intergranular to transgranular fracture decreased as the amount of cathodic polarization increased.

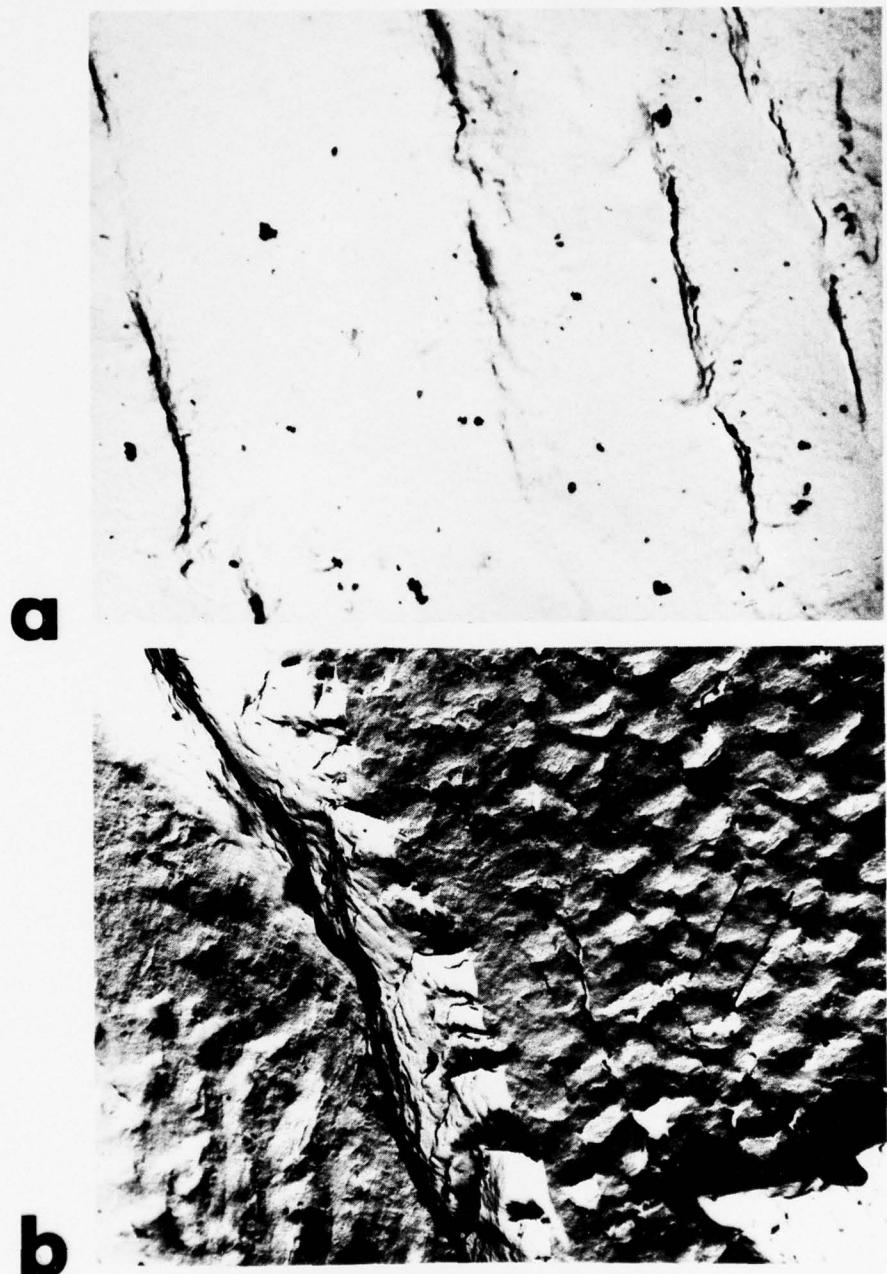


Figure 24. Two stage carbon replicas characteristic of the fracture morphology found in aqueous corrosion fatigue.

(a) An area of striationless fracture illustrating the brittle nature of failure (10,000x)

(b) A view of the type B striations adjacent to a river line. The black lines illustrate the striation spacing (8500x)

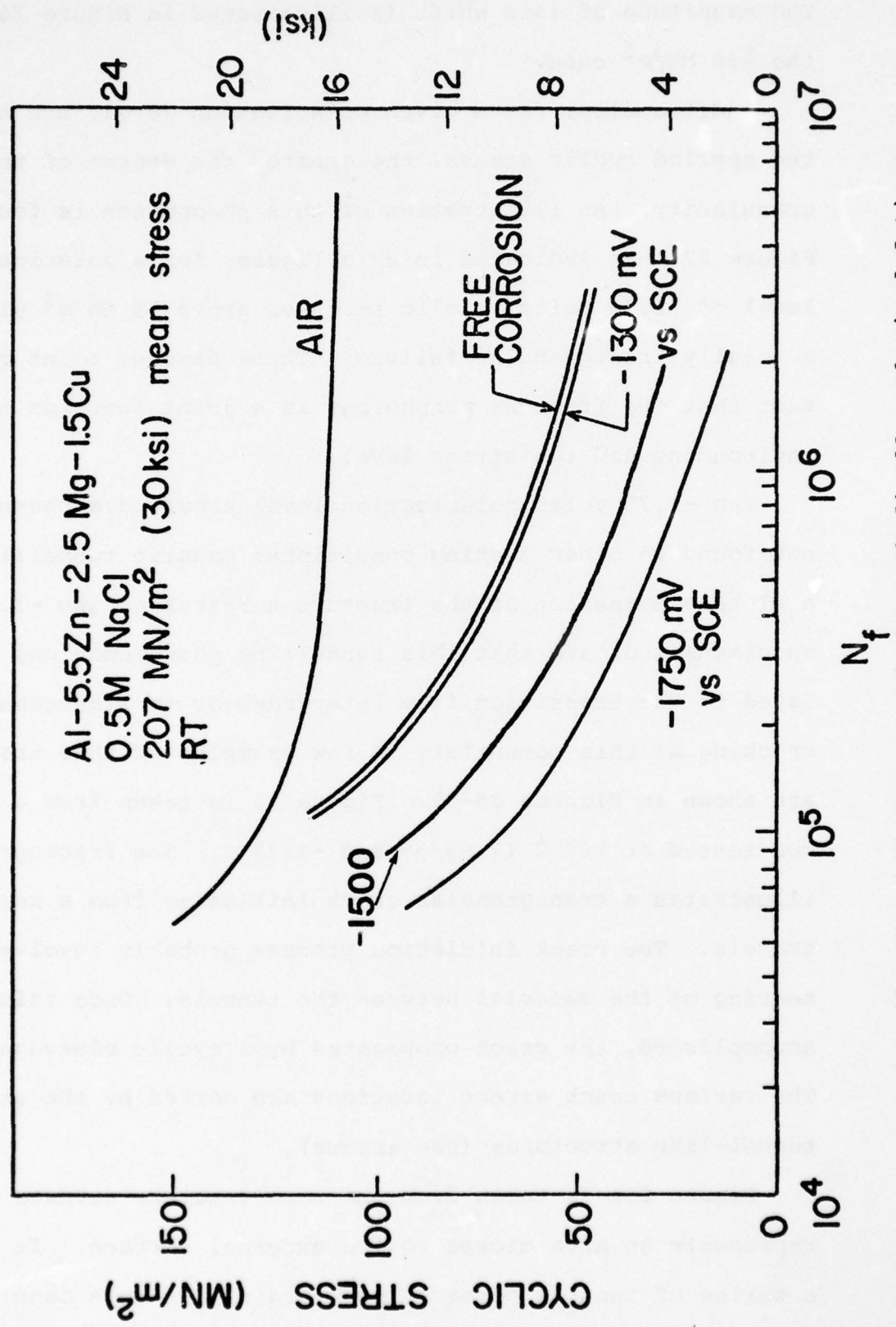


Figure 25. The S-N response of the cathodically polarized fatigue specimen.

Effect of Potential on the Fracture

Mode of Al-5.5Zn-2.5Mg-1.5Cu

in .5M NaCl tested at

207 MN/m<sup>2</sup>  $\pm$  69 MN/m<sup>2</sup>

<u>Potential (V vs. SCE)</u>	<u>% Intergranular Failure</u>
-.780	23
-1.300	5
-1.750	0

Figure 26

The fracture morphology for a number of specimens tested at 207  $\pm$  69 MN/m<sup>2</sup> at various electrochemical potentials

Effect of Cyclic Load on the Fracture

Morphology of Al-5.5Zn-2.5Mg-1.5Cu

in .5M NaCl Polarized to -1.75V vs. SCE

Cyclic Stress MN/m <sup>2</sup> at $\sigma_m$ = 207 MN/m <sup>2</sup>	% Intergranular Failure
76	0
69	0
55	0
41	10
28	26
17	35

Figure 27

The fracture morphology mix of  
specimens tested at -1.75v and 207 MN/m<sup>2</sup>  
mean stress for various applied cyclic loads



Figure 28

An SEM micrograph illustrating the case of caustic tunnels acting as the transition morphology between intergranular and transgranular failure modes (500x)

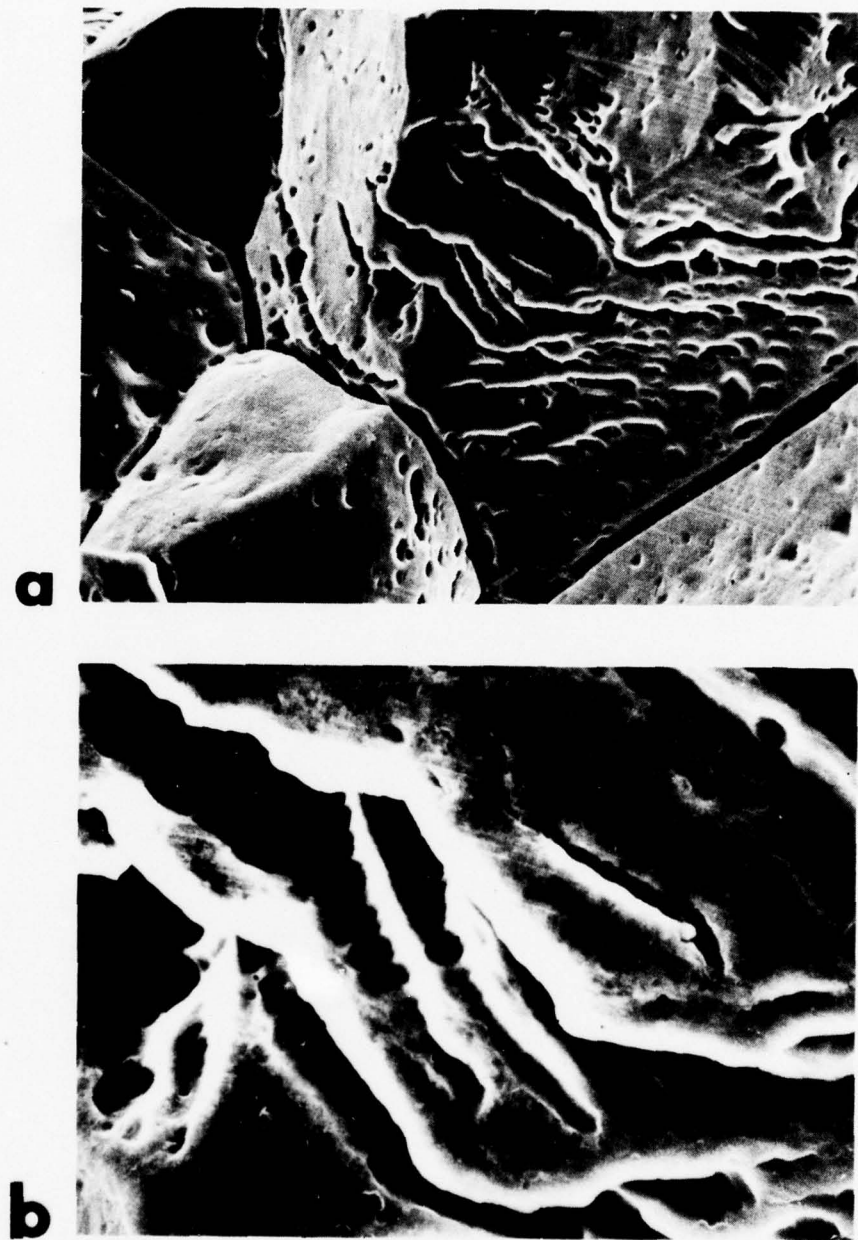


Figure 29. Caustic tunnels found near the external surface of a specimen charged at -1.75v

- (a) An overall view of the tunnels illustrating the parallel paths of their formation (500x)
- (b) A high magnification SEM fractograph illustrating the repetitive markings inside the tunnels (2,000x)

the net section stress is not large enough to initiate the transgranular failure, or the tunneling process occurred after the crack front had past. The first contention is favored since Figure 29b which is a higher magnification view of the same area, clearly shows that the tunnel is composed of a repetitive series of markings. It is believed that these markings correspond to the tunnel growth per cycle. It should also be noted that the tunnels in Figure 29 tend to follow rather straight paths around the perimeter of the grain. This would indicate that the attack is crystallographic in nature.

This assumption is supported by the optical micrograph shown in Figure 30. The micrograph is from a specimen which was pre-fatigued ( $\epsilon = .5\% \pm .25\%$ ) prior to a stress relaxation test under cathodic polarization (-1.75v). Although the specimen failed in an intergranular manner, the micrograph illustrates that the cathodic polarization resulted in a preferential, crystallographic attack of the fatigue generated slip bands. For such attack, it is not necessary that the slip band material be more chemically active than the surrounding material. Rather, the slip band merely serves to break or weaken the surface oxide layer above it. Once this occurs, it provides an easy path for the interaction with the environment. (This same line of reasoning can be used to explain the apparent crystallographic attack found in the previous figure.)

Before leaving this discussion of the tunnelling phenomenon, it should be pointed out that metallographic evidence points to

its interaction with the totally transgranular failures found under the high stress, ( $> 69 \text{ MN/m}^2$ ) high polarization levels. (-1.75v) Metallographic sections of these specimens indicate that the external surface contains a great number of tunnels. These tunnels act as stress concentrators, and provide a competitive fracture path to the grain boundaries. Examples of some of these cracks are shown in Figure 31. It is interesting to note that in Figure 31b, the fatigue cracks which extend from the severely etched surface have assumed paths which do not lie along the plane normal to the tensile axis. This acts to enforce the crystallographic nature of the cracking process. It should be mentioned that the only specimens which showed any evidence of secondary fatigue cracks were those which were polarized to -1.75v.

### 3. Single Crystals

As noted earlier, this alloy is extremely susceptible to intergranular corrosion fatigue cracking in the presence of aqueous chloride environments. In an effort to remove this cracking mode, and thereby study the environmental embrittlement of the precipitation hardened alloy matrix, a number of single crystal tests were conducted. As described earlier, a strain anneal method was used in preparation of the samples. Due to the nature of this process, it was virtually impossible to crystallographically orient the specimens prior to machining. Therefore, only one orientational consideration was used, and it was strictly geometric in nature; the specimen was

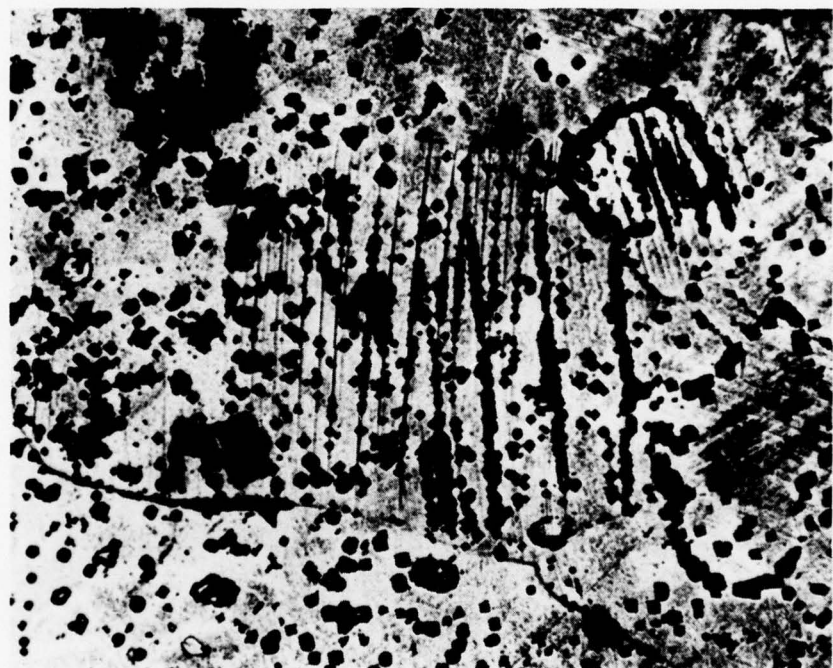


Figure 30

An optical micrograph illustrating preferential slip band attack in a pre-fatigued specimen polarized to -1.75v.

oriented to allow a single grain to occupy the entire gauge section. Unfortunately, this procedure led to an unsystematic selection of stress levels and tensile orientation.

A summary of the single crystal data is provided in Table III. The fatigue properties of these crystals generally parallel the properties of polycrystalline specimens. To illustrate this fact, Figure 32 is a plot of the resolved shear stress (peak value) versus the number of cycles to failure for the single crystal specimens. (The lines have been added to show the shape and relative position of the polycrystalline specimen curves.)

The fractographic examination of these specimens yielded some very interesting results. For comparative purposes, the data will be presented in the same order (air  $\rightarrow$  cathodically polarized) as the polycrystal specimens. Figures 33 a-c illustrate the fracture morphology of the specimen tested in air, slightly above the critical resolved shear stress. Figure 33a is a low magnification view of the fatigue fracture surface of this specimen. This micrograph shows a central nearly featureless fracture morphology, surrounded by an area of surface roughening. Figure 33b is a higher magnification observation of the cleavage-like area illustrating what appears to be slip intersections. Figure 33c is a micrograph taken from the roughened area. The arrow indicates a small patch of ductile striations.

Although some of the same features appear on the aqueous fatigued fracture surfaces, as the environment becomes more

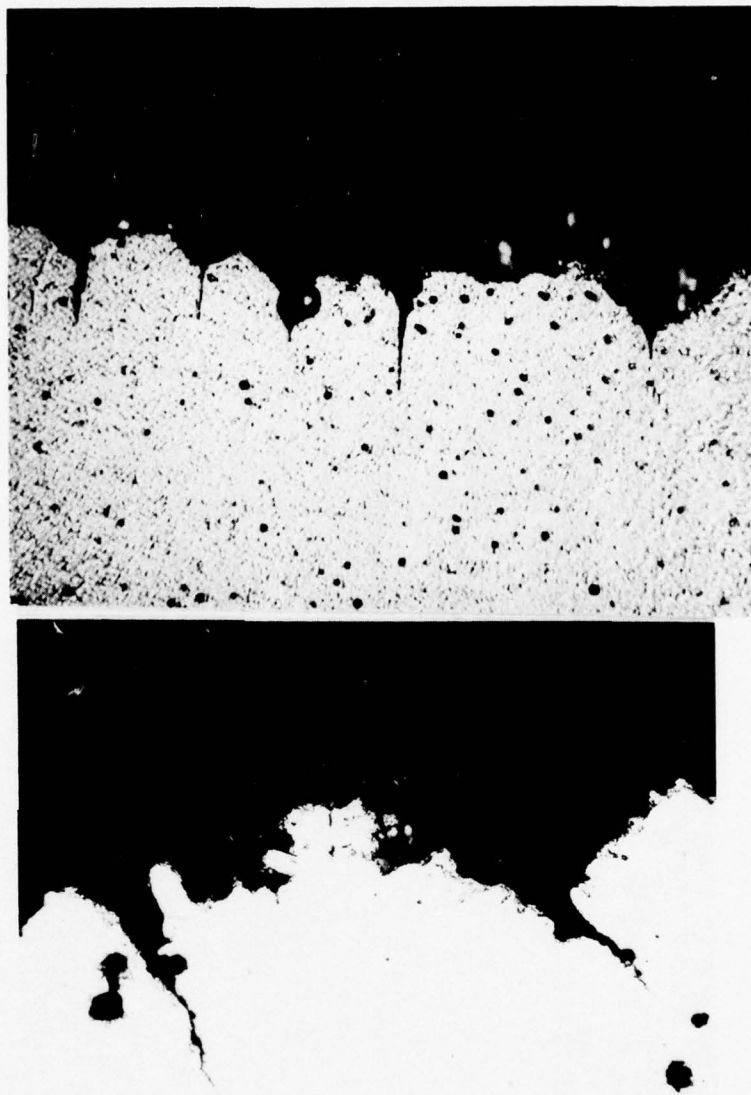


Figure 31

Optical micrographs illustrating the interaction between the external tunnels and transgranular fatigue crack

- a. An optical micrograph illustrating a number of transgranular cracks emanating from surface defects (100x)
- b. An optical micrograph illustrating the crystallographic nature of the fatigue cracking process. The arrows designate the tensile axis. (500x)

Table III  
A summary of all single crystal data

Specimen	Tensile axis orientation	Resolved Shear Stress (peak) (MN/m <sup>2</sup> )	Environment	Life (cycles to failure)	Fracture Mode
A (120)	751	149	air	430,000	quasi-cleavage (Q.C.)
B (131)	521	118	free corrosion (.5N NaCl)	326,000	corroded-appear to be Q.C.
C (132)	110	93	-1.750V (.5N NaCl)	201,000	extreme tunnel Q.C.
D (134)	532	118	-1.300V (.5N NaCl)	156.000	Q.C.
E (138)	661	91	-1.750V (.5N NaCl)	1,055,000	Q.C.
F (139)	542	97	-1.750V (.5N NaCl)	150,000	Q.C.
G	521	164	air	tensile test	dimple rupture

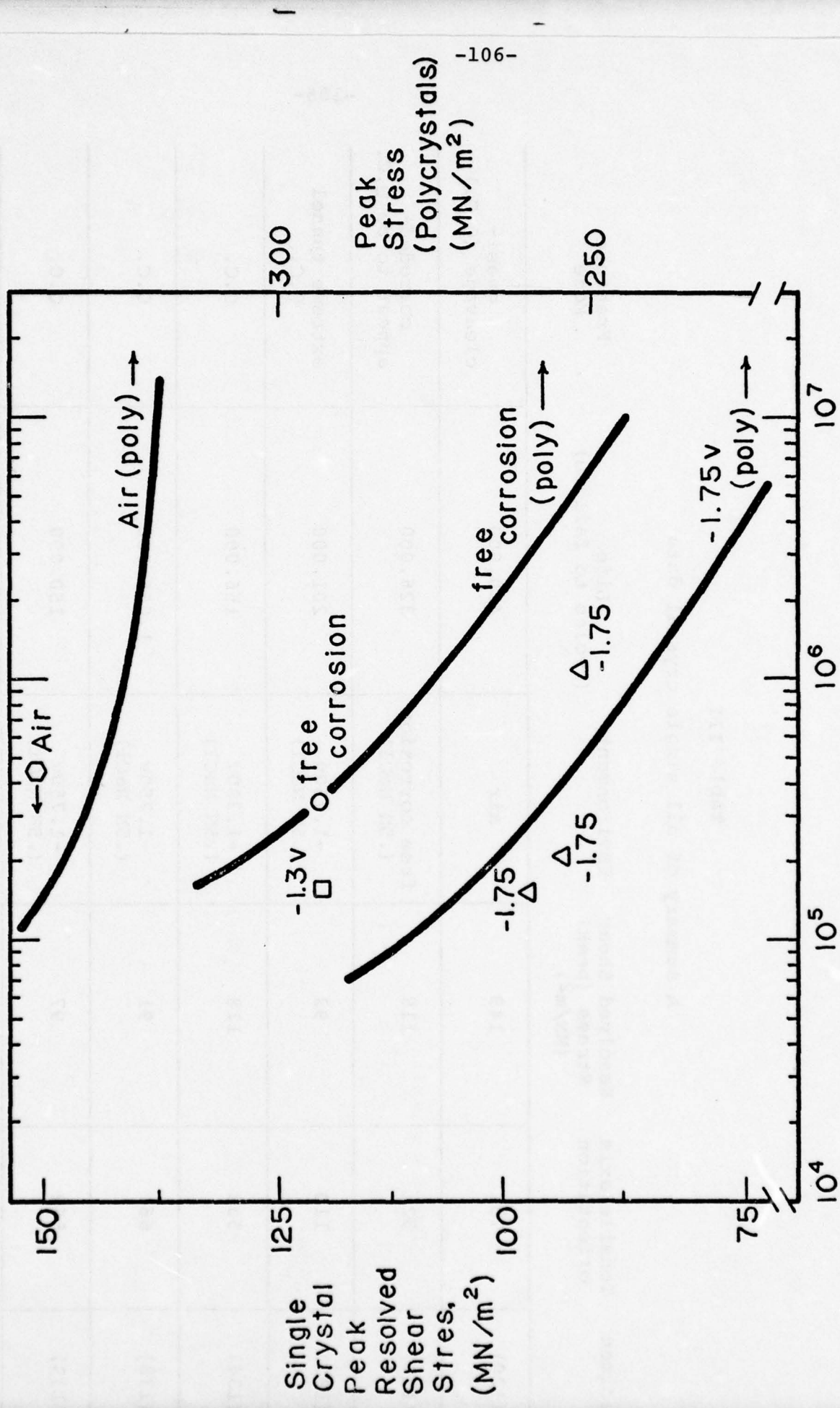


Figure 32. A plot of resolved shear stress versus the number of cycles to failure for the various single crystals tested in fatigue. (The reference lines illustrate the manner and manner of the polycrystalline behavior.)

aggressive, the markings take on a progressively stronger cleavage character. Figure 34 shows low magnification fractographs taken from the single crystals polarized to -1.3v and -1.75v in the .5N NaCl environment. Both specimens were oriented near the same orientation and demonstrated fatigue lives of  $1.5 \times 10^5$  cycles. In both cases, the river lines emanate from a corrosion defect on the surface (arrows). At these low magnifications, the overall cleavage morphology looks very similar to that found in the air case. At higher magnifications, some divergence becomes evident.

Figure 35 shows the brittle morphology of the river line markings from the -1.75 case. Note that there is no evidence of slip line emergence. This signifies a brittler fracture than the air case. This is substantiated by the fact that as shown in Figure 34b, the brittle cleavage structure extends over the entire cross-section of the specimen.

The 1.3v case appears to be intermediate between the air and -1.75v fractures. The river lines are free from any evidence of slip line emergence, but the cleavage morphology appears to transform to a surface roughening structure before reaching the tensile overload region. The high magnification fractograph of this area, shown in Figure 36, indicates that the roughening is simply the result of the river line structure running in two directions (see arrows). The most logical explanation for this feature is the activation of a second cleavage plane due to the increased local stress caused by the propagation of the crack.

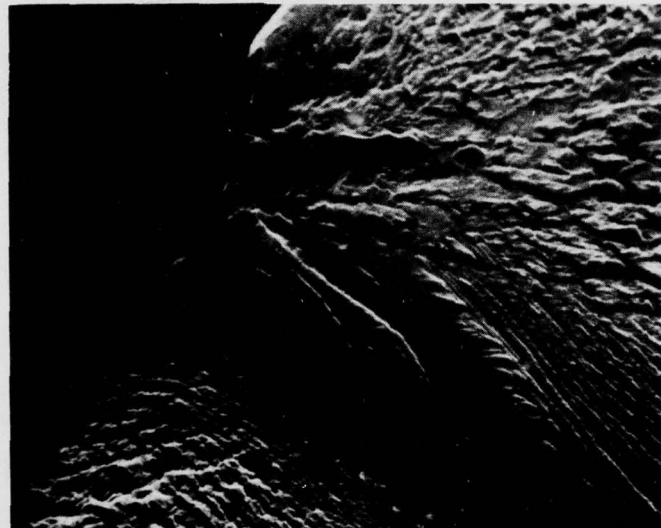


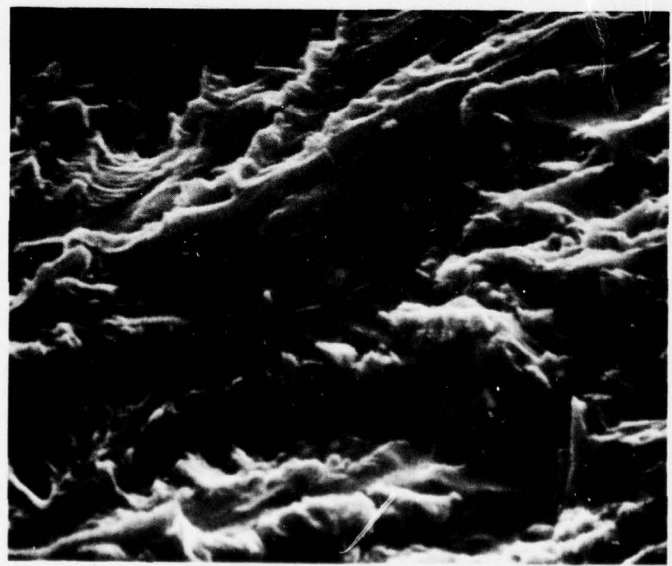
Figure 33

A series of SEM fractographs taken from an air fatigued single crystal

- a) An overall view of the fatigue portion of the fracture surface (500x)
- b) A high magnification SEM micrograph illustrating slip line intersections found in the cleavage area (5000x)
- c) A micrograph taken from the surface roughened area illustrating two small areas of ductile striations (2000x).



**b**



**c**

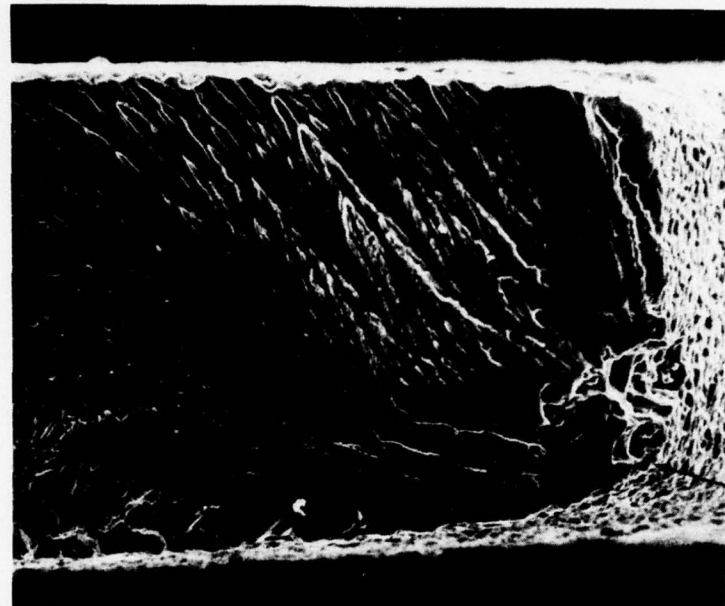


Figure 34

SEM fractographs characteristic of the cathodically polarized single crystal surfaces

- a) An overall view of the -1.3v fracture surface, with the arrow pointing toward the corrosive attack at the initiation site (200x)
- b) An overall view of the -1.75v fracture surface, with the arrows illustrating surface attack (250x)



In contrast to these micrographs, Figure 37 illustrates the overall fracture morphology of specimen #132. This specimen was oriented with a (110) tensile axis and polarized to -1.75v in the .5N NaCl electrolyte. The fracture surface appears to contain various zones. The initiation area is shown in Figures 38 and 39. Figures 38 and 38b are an SEM fractograph and a two-stage carbon replica, respectively, taken from the left plateau in Figure 37. They indicate that a caustic tunnelling process was active in this area. Figure 39 however, which is taken from the right plateau, indicates that this area is the result of a nearly featureless fracture morphology. It is impossible to say if either of these plateaus initiated first, but the overall shape of the fracture surface tends to indicate that the tunnelling and featureless region were simultaneous processes.

Figure 40 is a higher magnification composite of the right hand portion of the fracture surface. After the initial plateau, an area of featureless cleavage is found. This morphology then alternates with a river line structure similar to that seen on the other cathodically charged specimens. One should note that as the fracture alternates between the two morphologies, a drastic reduction in the number of river lines occurs as the crack passes through the cleavage area. This points to the very brittle nature of the cleavage morphology, and acts to confirm the fact that these features are indeed cleavage in origin and not the result of a corrosion reaction. The river line structure transforms to a general surface rough-

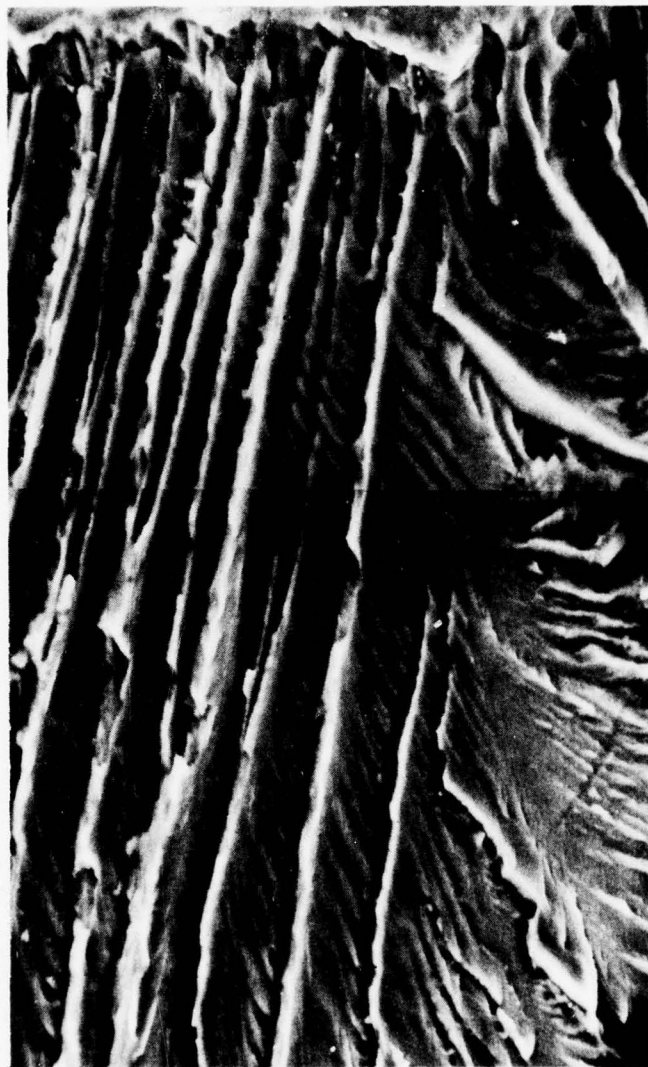


Figure 35

SEM fractograph illustrating the brittle nature of the river lines found on the surface of the single crystal polarized to -1.75v (2000x).

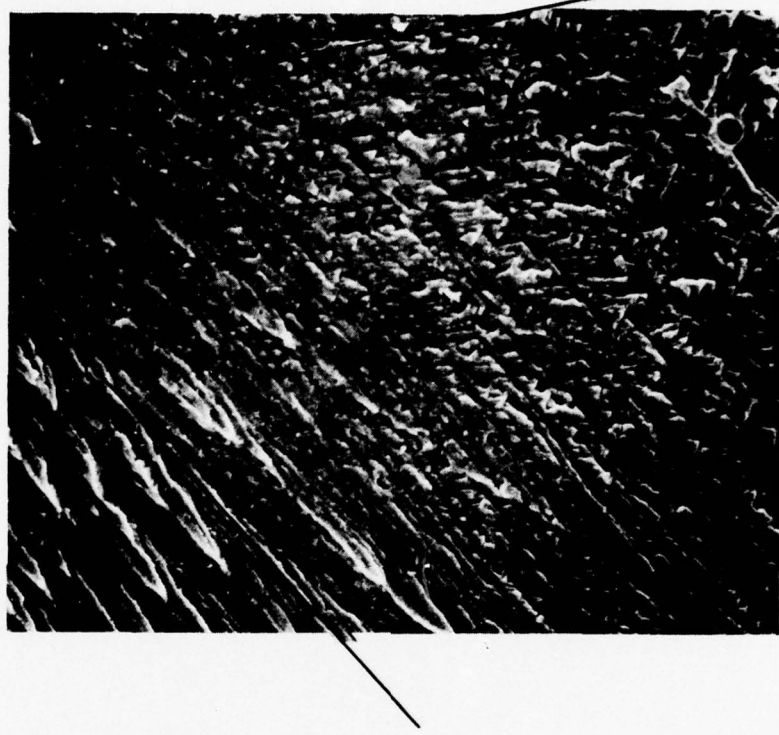


Figure 36

An SEM fractograph illustrating the structure of the surface roughened region from a single crystal polarized to -1.3v. The black lines indicate the direction of the intersection of river line patterns (1000x).

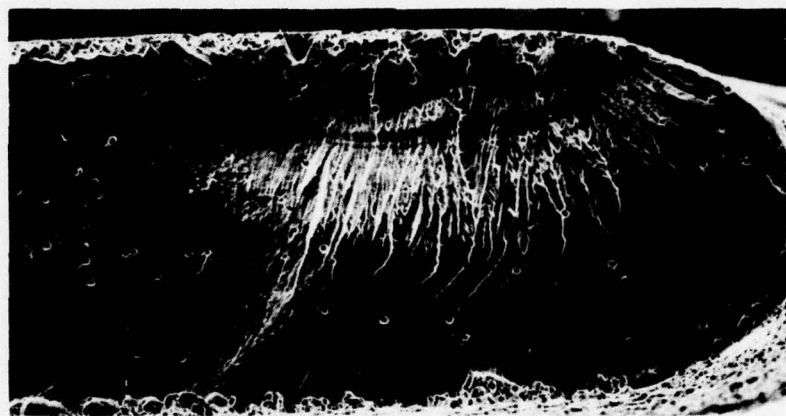


Figure 37

The overall fatigue fracture morphology of a (110) tensile axis orientation crystal polarized to -1.75v. (100x)

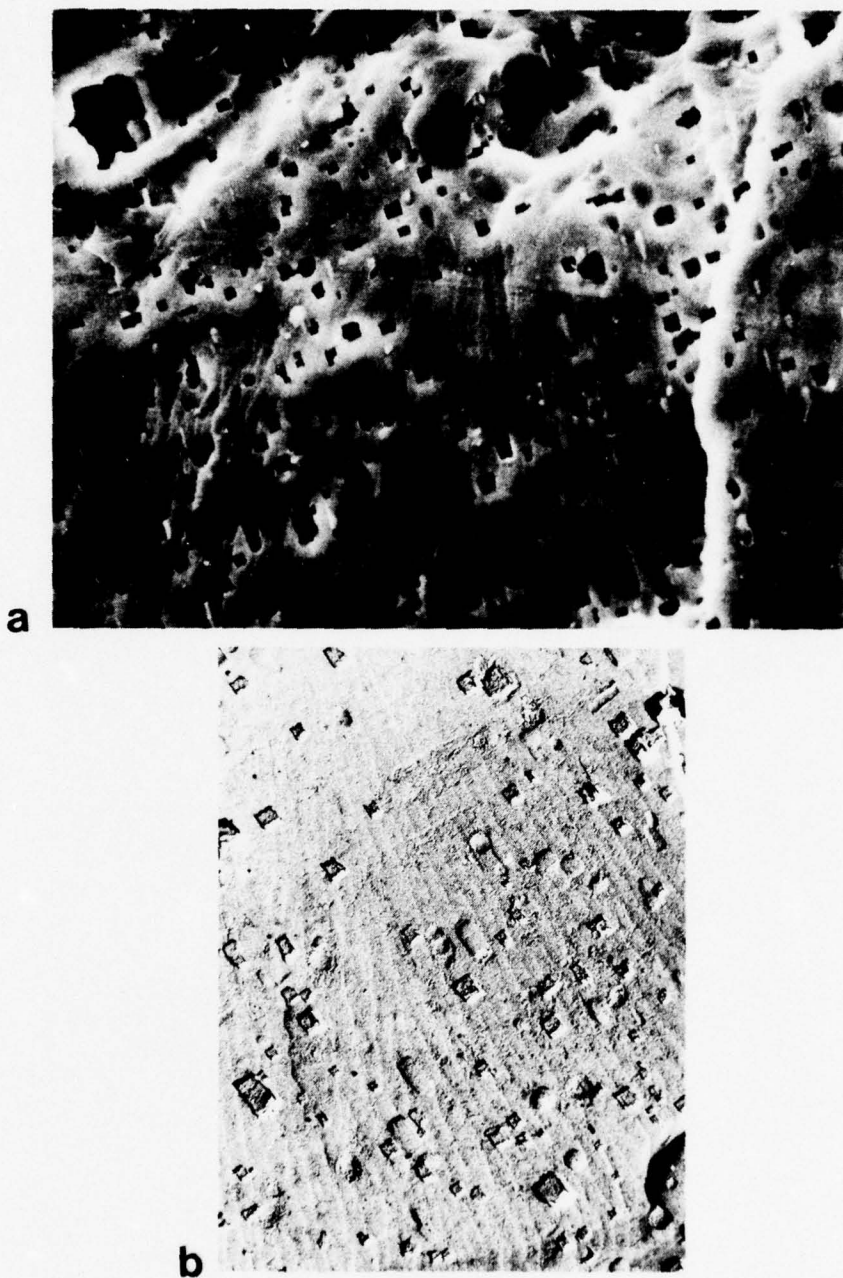


Figure 38

Examples of caustic tunnelling found on a single crystal fracture surface

- a) An SEM fractograph of the initiation sites shown in Figure 37. (2000x)
- b) A two-stage carbon replica of the same area. (2000x)

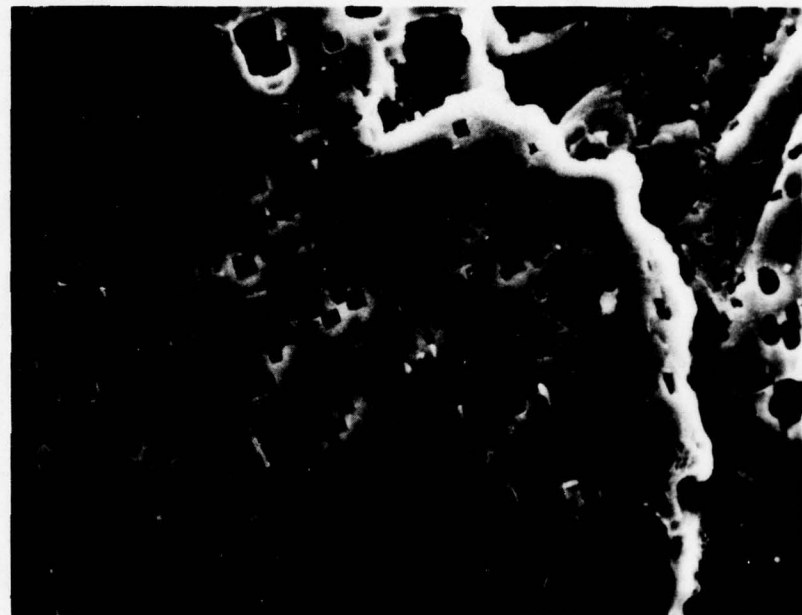


Figure 39

An SEM fractograph illustrating an area of pure cleavage adjacent to the caustic tunnelling shown in Figure 38 (2000x)

ening prior to tensile overload. This roughening is similar to that found in the -1.3v specimen, and appears to be the result of two overlapping, river line systems.

In an effort to clarify the crystallography of the various fracture morphologies, specimen #132 was metallographically sectioned transverse to the fracture surface. The resultant profile is shown in Figure 41. Although this does not provide the exact crystallographic relationships between the morphologies, it does provide valuable relative geometric information. It shows that after the initial plateau region, all the cleavage areas are parallel. Although this is not conclusive evidence, it does suggest that the featureless fracture areas are crystallographic. Both the topographical clarity and the parallel propagation paths tend to rule out a strictly corrosion related process. The figure also shows that both the river line and roughening morphology lie along parallel paths.

Before leaving the single crystal results, it should be stated that SEM examination of the tensile failures of these crystals clearly illustrate that the cleavage morphology is the result of the fatigue process. Figure 42 is a fractograph taken from a two-stage carbon replica of a tensile failure. It clearly illustrates a dimple-rupture fracture morphology. This is a ductile failure process and illustrates that the cleavage markings shown in this section are particular to the fatigue process and not the inherent fracture mode of the alloy.

#### C. Stress Relaxation

In an effort to clarify the embrittlement mechanism, a



Figure 40

An SEM composite micrograph illustrating the various regions found on the  $\langle 110 \rangle$  tensile orientation single crystal fatigued at -1.75v. (500x)

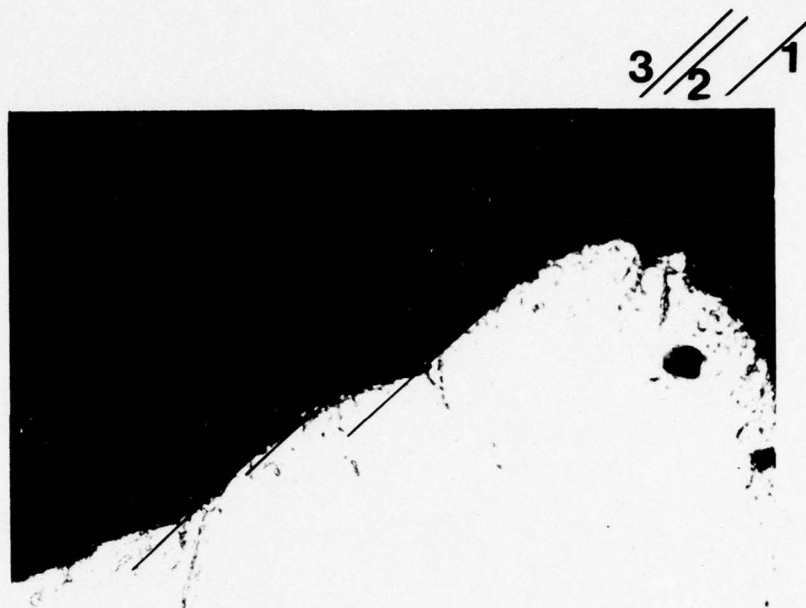


Figure 41

A metallographic profile of the fracture surface shown in Figure 40 illustrating approximate geometric relations between the various fracture morphologies. (The numbered lines illustrate the parallel crack path of the cleavage type fracture.)  
(750x)

number of stress relaxation experiments were performed. In an effort to provide a basis for comparison, a number of tests were performed in laboratory air and under hydrogen charging conditions. In all cases, the specimens were first pulled beyond the macro-yield point. This initiated a significant amount of dislocation motion, and also acted to crack the air formed oxide. After a small amount of plastic deformation, the specimens were held at a constant elongation position. The specimens were then re-pulled, and the resultant load-elongation behavior was monitored.

In an effort to establish the experimental parameters, the initial tests were conducted on the as processed material. The results of an air test for this material are shown in Figure 43. The air curve shows an initial yield point of  $381 \text{ MN/m}^2$ . The specimen was pulled to a peak stress of  $393 \text{ MN/m}^2$  and allowed to stress relax for 24 hours. Upon the re-straining, a small yield point drop was detected prior to failure.

A similar experiment was conducted under the hydrogen charging conditions, but in this test the relaxation time was shortened to three hours. (Since for longer charging times, the specimens failed before the re-straining could be performed.) As is shown in Figure 42b, after this shorter charging period, the re-straining produces a much larger yield point drop. Since the original strain hardening characteristics were reached prior to failure, the specimen was again relaxed, but only for 30 minutes this time. Upon re-straining for a second time,



Figure 42

A two stage carbon fractograph  
taken from the surface of a single crystal  
pulled to failure in tension.

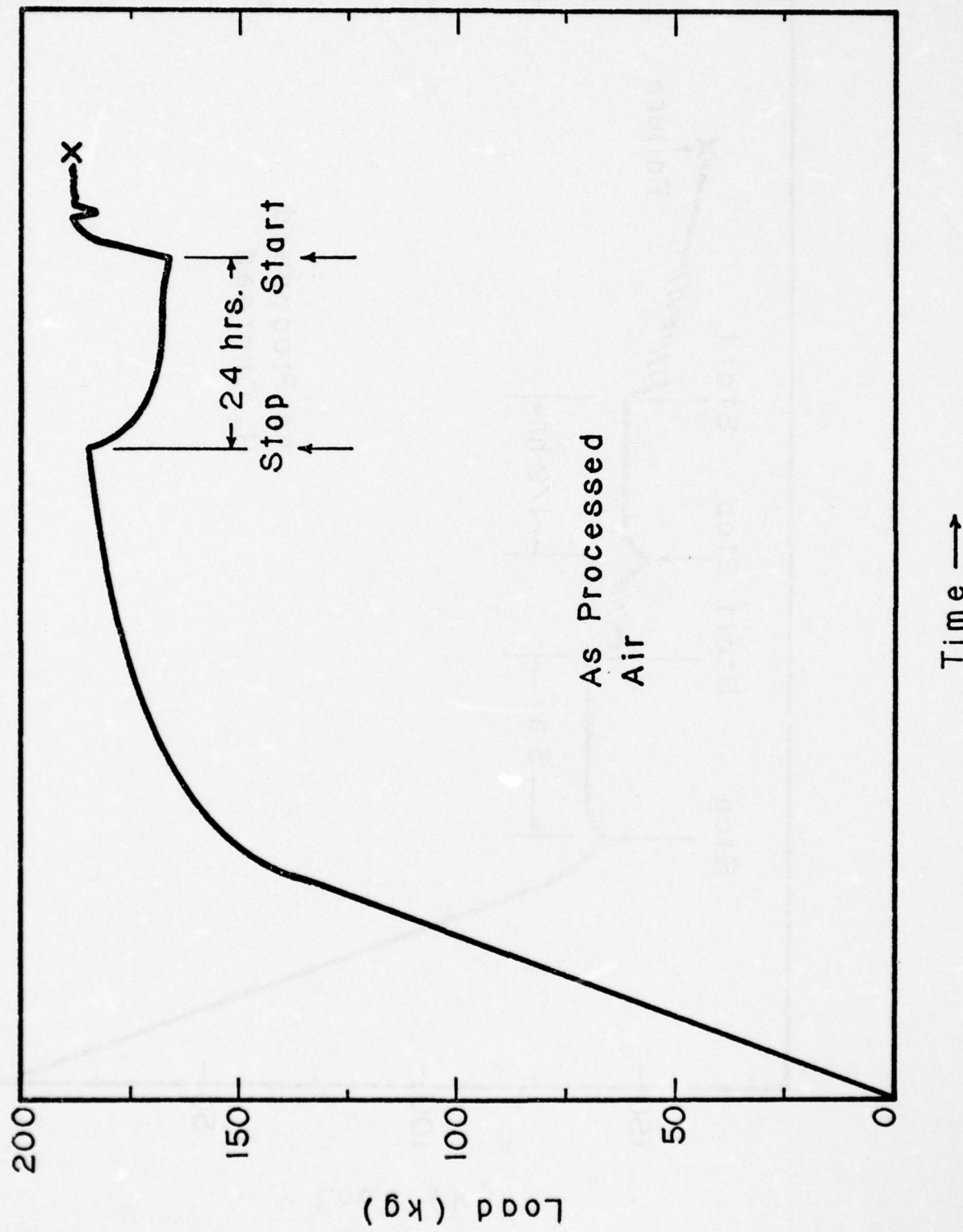
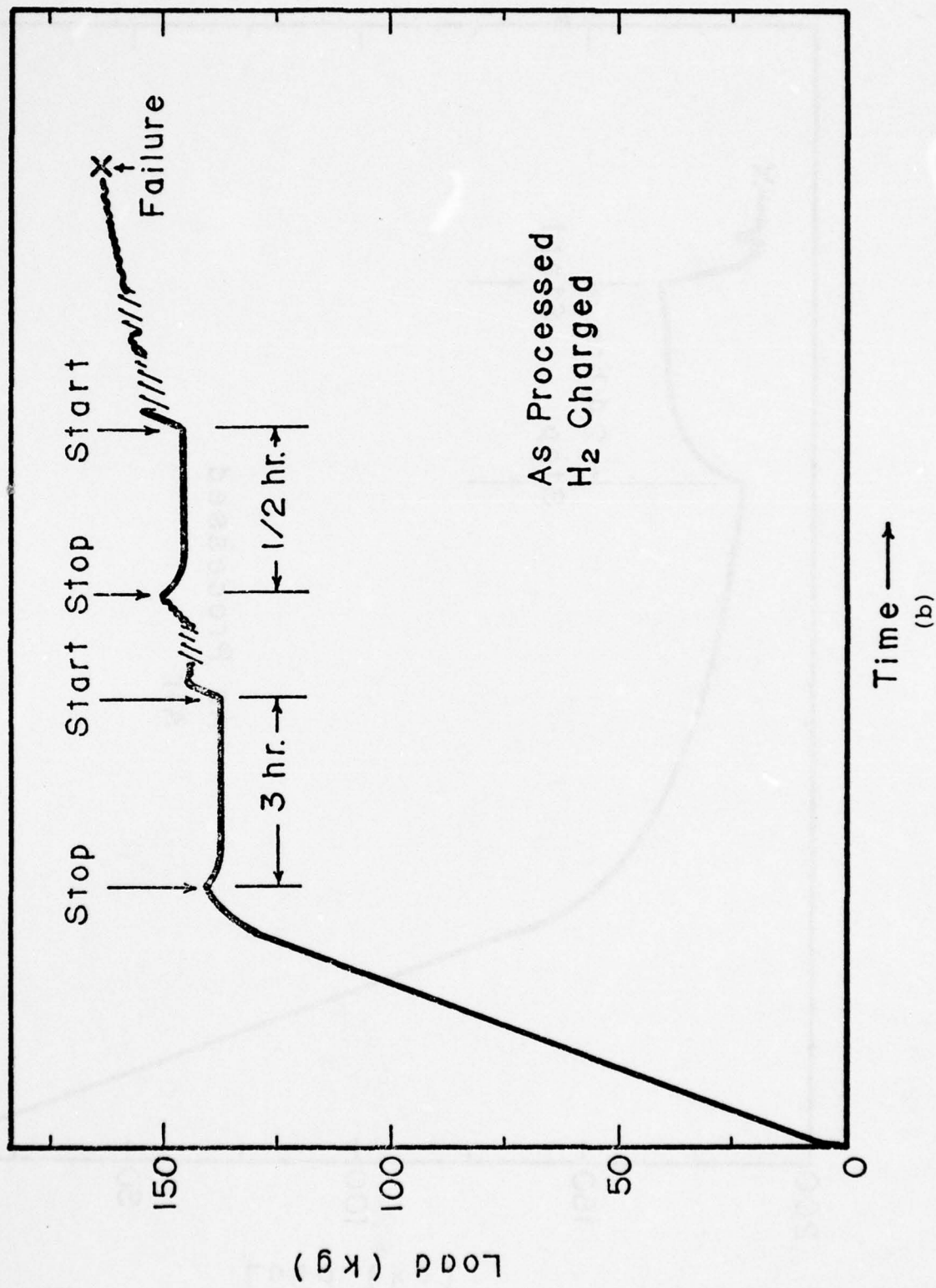


Figure 43. Stress relaxation curves for the as process material (a) Tested in air; (b) Tested in 1N  $\text{H}_2\text{SO}_4 + .2\text{N NaAsO}_3$  at  $-1.75\text{v}$  vs. SCE.



even larger yield drops were encountered. Since this yield point phenomenon is caused by interstitial pinning of dislocations, this data gives direct evidence for a hydrogen dislocation interaction in aluminum.

It is recognized, however, that the metallurgical state of the as processed material is not easily definable or reproducible. TEM examination revealed that this material had a very high initial dislocation density. The dislocations were arranged in a continuous tangle. The resultant strain contrast made it impossible to resolve individual dislocation segments. This is certainly much different than the planar slip found in the T-6 specimens tested throughout the rest of this study. Therefore, a number of tests were conducted to reproduce the results found in the as processed material with the more metallurgically reproducible T-6 condition.

The initial tests were performed on polycrystalline T-6 specimens tested at -1.75v in both .5% NaCl and the arsenite solution previously mentioned. The tests were also repeated with cold rolled (up to 40% reduction in area), T-6 specimens in the arsenite solution. All these attempts resulted in intergranular failures occurring upon the re-stressing. Some of the specimens tested in the arsenite even failed intergranularly before the three hour charging period had elapsed. A characteristic load-time curve for this type of test is shown in Figure 44.

Since the intergranular failure mode had been encountered in most of the aqueous fatigue tests, these tests act to confirm

the role of hydrogen in the intergranular failure of these alloys.

In a future effort to reproduce the yield point drop in a T-6 tempered alloy, single crystal specimens were tested under the hydrogen charging conditions (-1.75v in a 1N  $H_2SO_4$  + .2N  $NaAsO_3$  solution). The results for one of these tests is shown in Figure 4: As with the polycrystalline specimens, the sample was elongated to slightly beyond its yield point. It was then allowed to relax (while being charged under constant elongation conditions) for three hours. Upon re-straining, a yield drop was detected. The straining continued until the original strain hardening characteristics returned. The experiment was then repeated, and after the three hour charging period, a second yield point was detected prior to failure.

It should be noted that a few other single crystal tests were attempted. In these cases, the specimens failed outside the guage section. The failures were intergranular in nature, and occurred under the protective lacquer at the boundary between the guage section grain and the remaining grains in the grip section. Since no defects could be found in the lacquer, it is suggested that the failure was caused by dislocation induced hydrogen transport to the grain boundary.

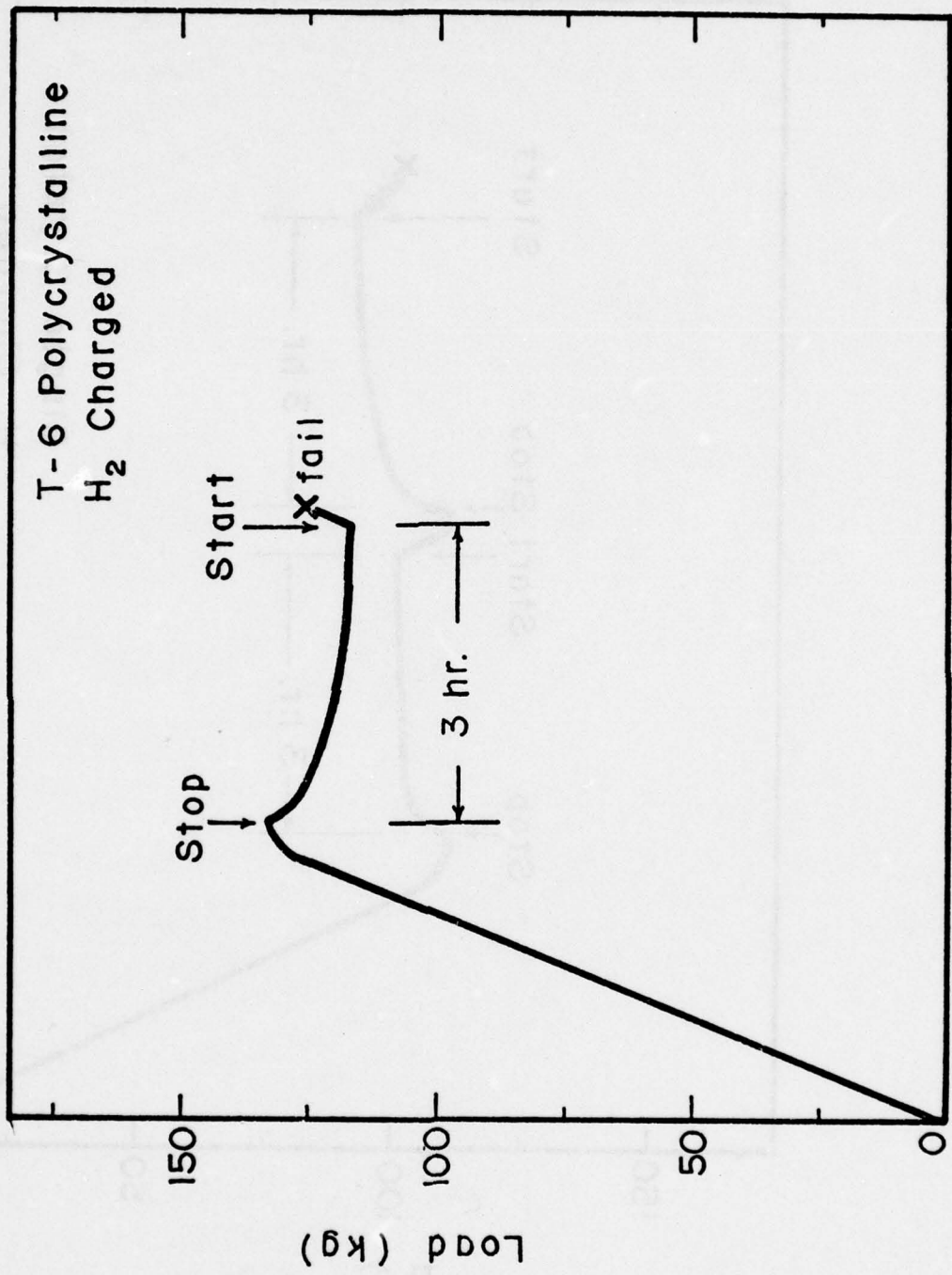


Figure 44. Stress relaxation curve for T-6 aged, polycrystalline, Al-5.0Mg-2.5Zn-1.5 tested in 1N  $H_2SO_4$  + .2N  $NaAsO_3$  at -1.75v vs. SCE.

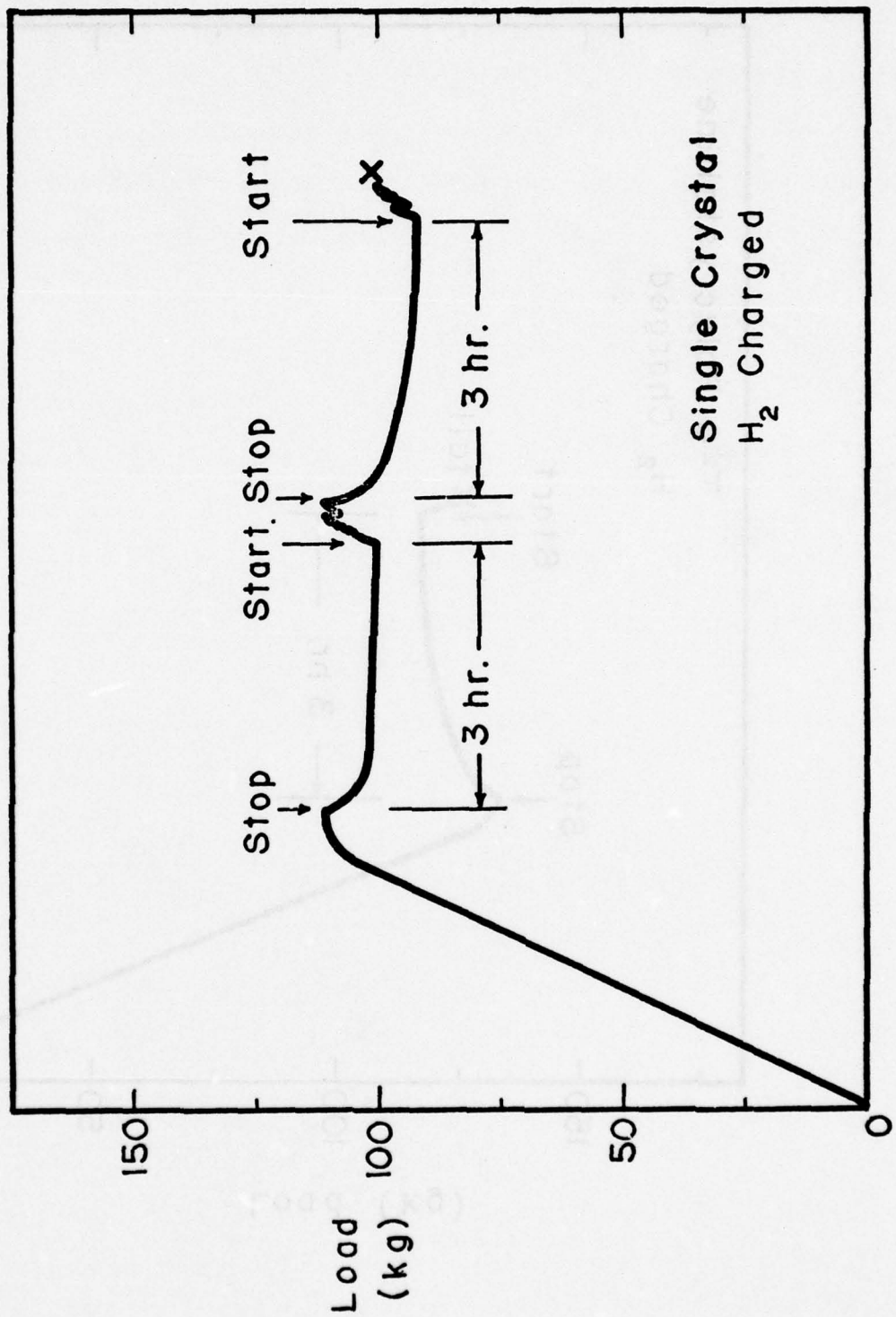


Figure 45. Stress relaxation curve for T-6 aged single crystal specimen tested in 1N  $H_2SO_4$  + .2N  $NaAsO_3$  at -1.75v vs. SCE.

Discussion

In attempting to understand the mechanism(s) responsible for the corrosion fatigue behavior of this alloy, it is necessary to explain at least three major experimental observations: 1. the loss of fatigue strength, 2. the changes in fracture morphology, and 3. the reported reversibility of the embrittlement process.

Historically, the theories of corrosion fatigue have relied on the following mechanism: 1. stress concentration at the base of the pits, 2. preferential electrochemical attack at the plastically deformed regions of the metal, 3. surface adsorption effects, 4. fatigue induced mechanical failure of the protective oxide leading to accelerated local attack, and 5. hydrogen induced separation.

Since all of these models provide a justification for the observed decrease in the mechanical strength of the alloy, it is necessary to consider if any of these models can also explain the observed fracture morphologies. The fractographic evidence tabulated in Figures 26 and 27 indicates that in the majority of cases the fracture resulted from an intergranular initiation leading to a transgranular propagation. Since the only observed pitting (tunnelling) phenomenon occurred at  $-1.75v$ , the stress concentration model cannot be applied to the majority of these failures. Although the preferential dissolution model may be related to the observed tunnelling response, it is highly doubtful that proponents of this mechanism could explain the transition from intergranular to transgranular cracking at the higher cathodic polarization levels. It is also doubtful that an electro-

chemical process could produce areas of nearly featureless, apparently crystallographic fracture and leave no evidence of a corrosion product.

Although the fatigue induced rupture of the protective oxide may be important in the crack initiation process, it is difficult to understand how this model could be used to explain the observed change in the fracture path. It is also difficult to envision the model explaining the formation of a featureless fracture region. One would expect to see evidence of the oxide formation process.

This leaves only the surface adsorption and the hydrogen induced separation models. Although some might argue that these are in the same mechanism, the separation is used to distinguish between 1) a model which suggests that the observed behavior is due to the adsorption of the embrittling species from the electrolyte to the crack tip causing a reduction in the surface energy needed for crack propagation, and 2) a model which suggests that the observed embrittlement is due to an internal enrichment of hydrogen leading to a weakening of the metal ahead of (not at) the crack tip.

In considering the surface adsorption model, it is difficult to understand how a model which is based on the external adsorption of an embrittling species would produce a change in fracture path which is dependent on both the applied potential (see Figure 26) and the applied stress (Figure 27). Additionally, the surface adsorption model cannot explain how the recovery process illustrated would have a time dependent component. Since this

model envisions a surface interaction, the desorption process should occur almost instantaneously (especially at the 465°C temperatures used in reference 89).

The hydrogen separation model can however, be used to explain all the observed results. The shift in fracture morphology can be related to a shift in the enrichment process, and the time dependent recovery process is the result of hydrogen diffusion away from its enrichment sites (a time dependent process). The bulk of this discussion will, therefore, consider the various enrichment processes and develop a semi-quantitative model to explain the observed fracture morphology. In addition, a short discussion of the air fatigue process will be presented. It is felt that a firm understanding of this process will aid in understanding the aqueous fatigue model.

#### A. Air Fatigue

Although the primary emphasis of this program concerns the investigation of aqueous corrosion fatigue behavior, it became evident that any attempt to understand this complex phenomenon should begin by defining the air fatigue mechanism. In other words, before trying to understand the effect of corrosion on the fatigue process, one should understand the fatigue process.

As mentioned earlier, the fatigue models tend to center around three general concepts: a precipitate cutting model, a quenched in inhomogeneities model, and a critical dipole density model. Unfortunately, the precipitate size for the T-6 aging condition is too small ( $35-45\text{\AA}$ ) to allow the direct observation of the dislocation particle interactions. Therefore, one must use somewhat more indirect evidence to assess the applicability of the various models.

For example, the prime requisite of the precipitate cutting and inhomogeneities model is the formation of an easy path for dislocation motion. In a mechanical sense, this would result in a cyclic softening behavior. As was shown in Figure 21, the T-6 heat treatment shows a cyclic hardening response. This would indicate that the fatigue process acts to increase the resistance of the slip band to dislocation motion. This is the essence of the dipole model formulated by Duquette and Swann.  
16

Before beginning a more detailed discussion of the model, it should be pointed out that the observed slip band structure favors the dipole model. The various TEM observations of the slip bands shown in Figures 18-20 clearly show the very high

density of loops necessitated for the Duquette and Swann model. The figures show that the loops are present throughout the various stages of slip band formation. The loops, which have been interpreted as dipoles, would act as obstacles to further dislocation motion, and as pointed out by Feltner,<sup>88</sup> each loop could act to initiate additional loop production. Therefore, even if the fatigue process did act to cause reversion of the local precipitate structure, the prismatic nature of the dipoles would preclude the slip band from becoming an easy path for dislocation motion. From a phenomenological viewpoint, therefore, the structure of the slip band would act to rule out the easy path dependent models, and instead, would act to favor a dislocation debris model.

The initial state of the T-6 alloy is a combination of finely dispersed  $\eta$  and  $\eta'$  precipitates and a low density of helical dislocations. The majority of the precipitates are believed to be partially coherent (along the (111) slip plane of the alloy) with the matrix. This structure acts to promote planar slip. With the application of a cyclic stress, the helical dislocations are transformed to long straight dislocations which lie along  $\langle 110 \rangle$  directions.<sup>16</sup> These screw dislocations bow along the slip plane, and through some type of precipitate or dislocation interaction, portions of dislocation lines become pinned. It is the pinning process which leads to the dipole formation.

The nature of the pinning process determines whether the elongated portion of the dipole lies parallel or perpendicular to the original dislocation line. Since the micrographs shown

in Figure 20 clearly illustrate both types of loop, a brief review of the dipole formation process is presented. The case for loops lying along the  $\langle 110 \rangle$  direction has been described by Ryum to explain a similar phenomenon found in the tensile deformation of a similar Al-Zn-Mg alloy. The model analyzes the various dislocation-precipitate interactions for a tetrahedral precipitate which is coherent on the (111) planes. The tetrahedral geometry is assumed to allow the precipitate to take a shape which is consistent with the symmetry of the (111) plane. The analysis indicates that a dislocation can move relatively easy in all directions except the  $\langle 110 \rangle$ . For this reason, dislocations are thought to move forward by the lateral motion of  $\langle 112 \rangle$  kinks in the slip plane. As long as they remain in the slip plane, the lateral annihilation of the kinks produces a forward motion parallel to the  $\langle 110 \rangle$  direction. This type of motion is quite evident from Figure 1b taken from the work of Duquette and Swann.

If however, the original dislocation segment has cross-slipped, the kink would no longer be annihilated by its lateral motion, and an open ended dipole would be formed. The dotted portion of the dislocation line in Figure 46a illustrates the dipole. Two possible mechanisms for transforming the open ended dipoles to a closed loop are shown in Figures 46b-c. Figure 46b illustrates the case where the cross-slip is short enough to allow interaction between the dipole and the original dislocation line. Figure 46c illustrates a dipole pinch off due to a greater distance between the dislocations. This model explains the forma-

tion of dislocation loops similar to those labeled "S" in Figure 20.

If one considers the geometry illustrated in Figure 47, a similar process can also be used to explain the M type dipoles of Figure 20. In this case, the interaction of two perpendicular screw dislocations has resulted in the formation of an edge jog (see Figure 47b). As pointed out by Cottrell,<sup>90</sup> the jog can only move along the original screw dislocation, and therefore, prevents any further motion of the dislocation line in the original slip plane. In order for the dislocation to move, either the jog must be annihilated by combining with a jog of equal magnitude but opposite sign, or else, the original screw segments must bow out across two new parallel slip planes. As illustrated in Figure 47c, this second alternative would create a prismatic edge dipole. The dipole could then be transformed into a dislocation loop through either cross slip or another dislocation intersection. The resultant structure, which is shown in Figure 47d agrees with the observed structure of Figure 20b.

Upon their formation, the dipoles would be expected to assume the relative position which would balance the applied shear stresses. If for the sake of argument, we assume the initial state to be stress free, then in an effort to minimize the energy of the dipole, the isolated dislocations would take up the positions illustrated in Figure 48a. In an actual slip band however, the dipole is neither isolated from other dislocations, nor is it in a stress free environment. A more realistic geometry might be that of Figure 48b, where the actual values of the various

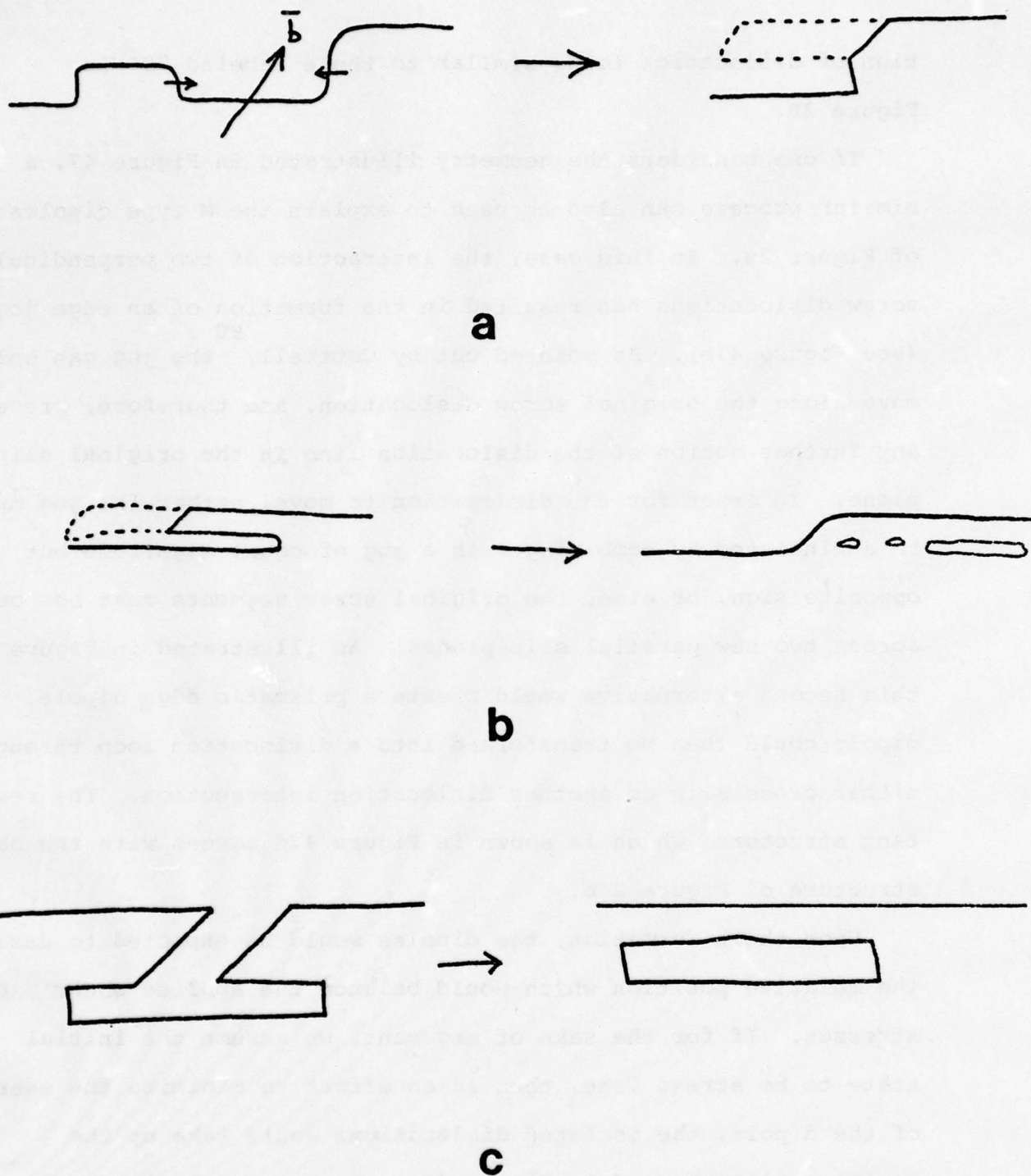


Figure 46. The proposed steps involved in transforming a <112> kinks into sessile loops.

- (a) A schematic illustration of the lateral motion of the kinks.
- (b) The suggested transformation of the dipoles into loops for small separation between the dipoles and the original dislocation line.
- (c) The suggested transformation for a larger separation between the loops and original dislocation line.

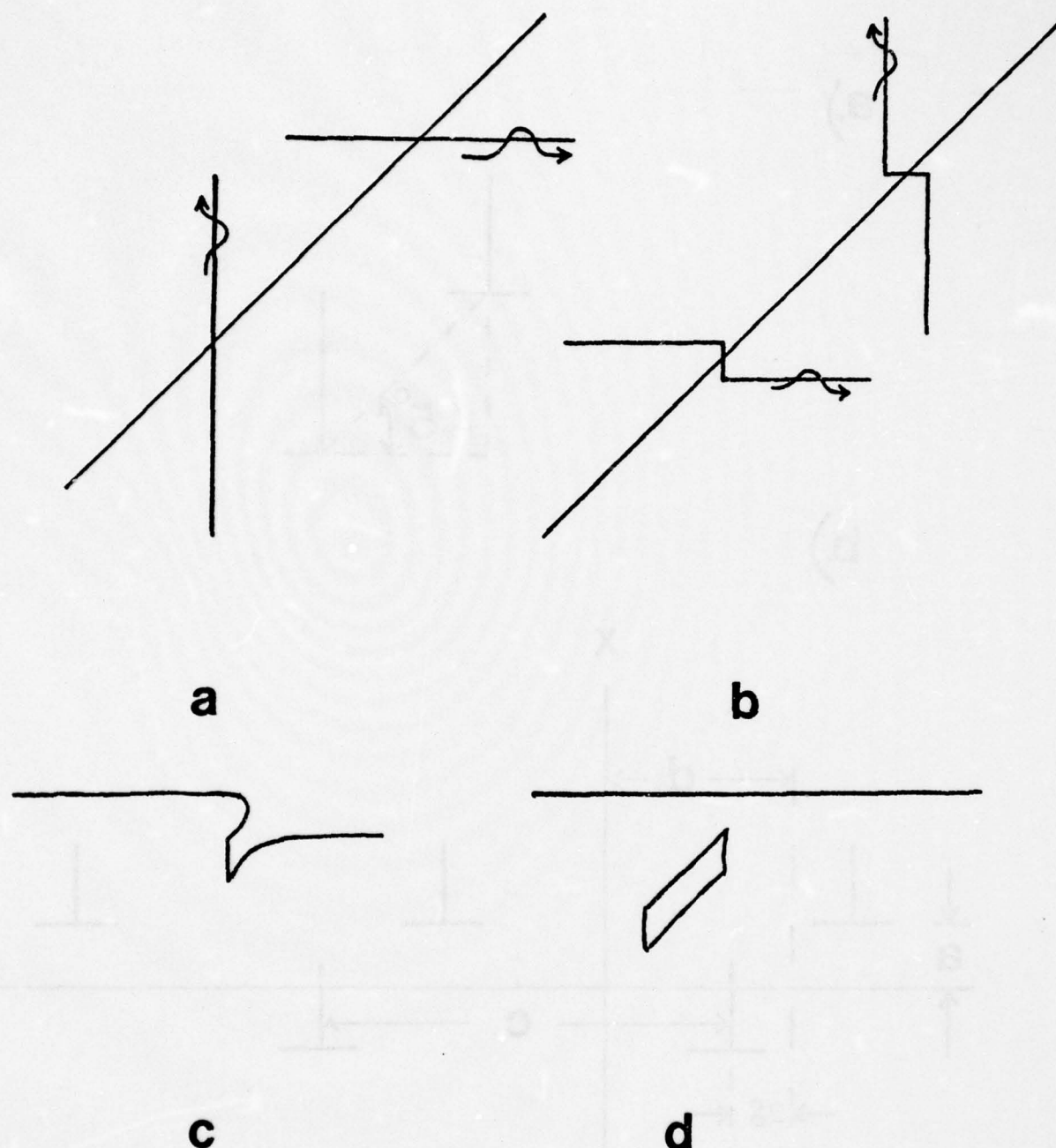
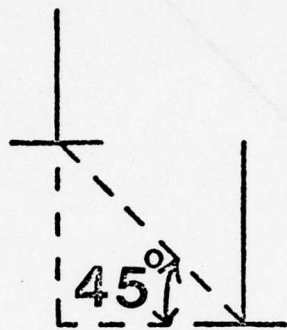


Figure 47. The proposed steps in transforming a screw dislocation into sessile dipoles.

- (a) Two screw dislocations with perpendicular burger vectors.
- (b) The intersection of the screw dislocations resulting in a jogged structure.
- (c) The formation of a dipole resulting from the movement of the screw dislocation on two slip planes.
- (d) The formation of a loop resulting from the separation of the dipole from the original dislocation line.

a.)



b.)

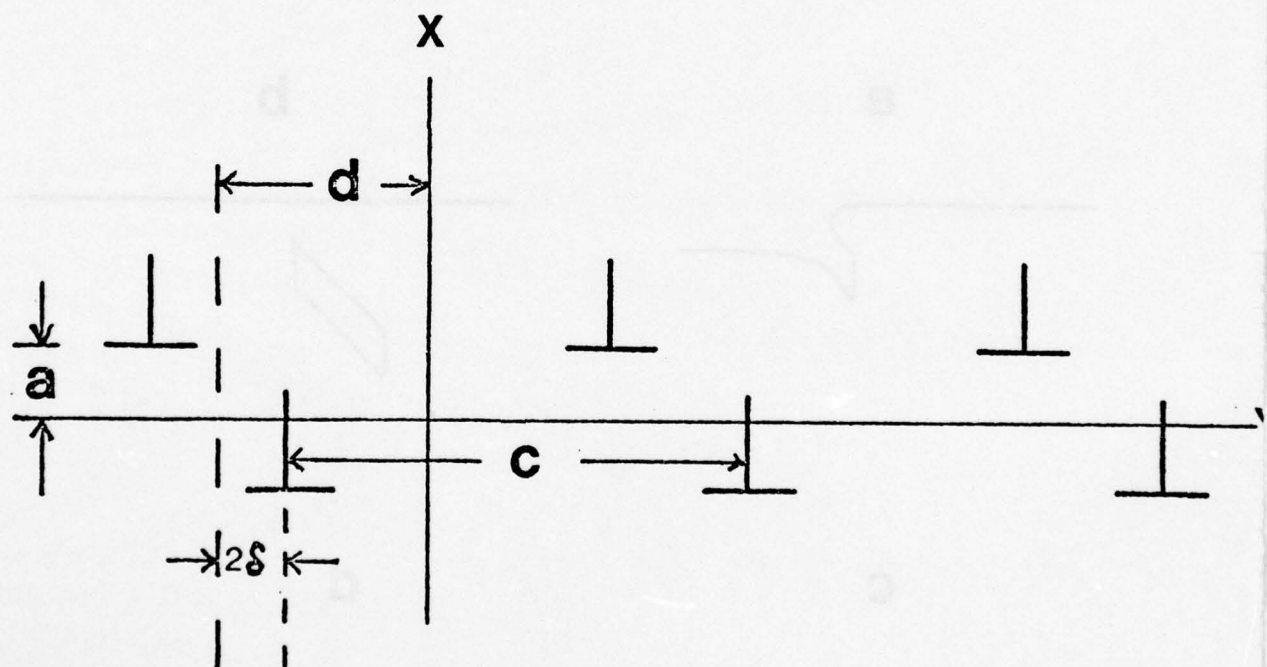


Figure 48. Dislocation dipoles geometries.

- (a) Geometry for an isolated stress free dipole.
- (b) A variable geometry used to fix the possible dipole positions within an infinite array.

orientational parameters are dependent on the local conditions.

91

Using such a configuration, McNeil and Grosskreutz have theoretically analyzed the dilatation of any arbitrary point in the plane containing the mid-points of the dipoles. Their results for various geometries are shown in Figure 49. This figure clearly illustrates that the dipoles exert large dilatational strains, and therefore could make a real contribution to the crack nucleation process. It should also be noted that although the calculations are based on an infinite array of dipoles, the use of a partial summation process (for as few as five dipoles) shows the dilatation to be within a few per cent of the infinite array values.

Following the same methodology, it is possible to evaluate the resultant normal stress of the array. In physical terms, this is the stress which would act to nucleate a cleavage crack on the midpoint plane. In terms of a useful model, it is helpful to correlate the magnitude of this stress with the changes found in the slip band structure due to the fatigue process. As indicated in Figures 18-20, the fatigue process acts to increase the density of dipoles within the slip band. Therefore, if dipole accumulation does lead to a cleavage type crack initiation, then one should be able to correlate an increased dipole density with an increase in the cleavage stress.

In terms of the various orientation parameters shown in Figure 48b, an increased dipole density is most easily interpreted by decreasing the value of  $c$ , the interdipole distance. If all other parameters are fixed, this would manifest itself as

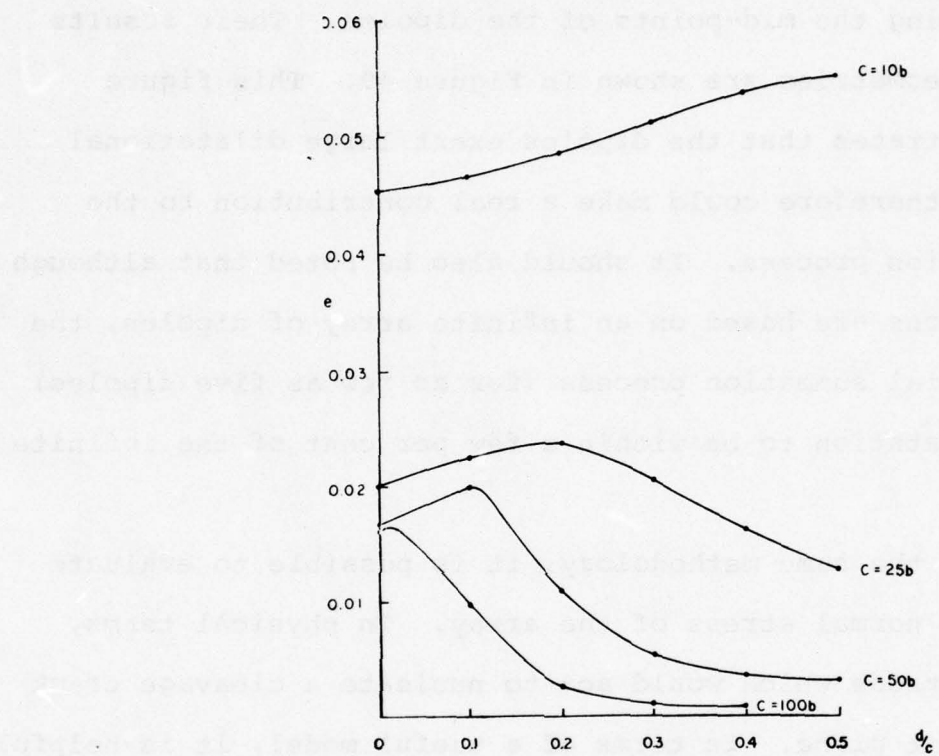


Figure 49

Dilatation across a dislocation dipole array as a function of the relative spacing of the dipoles within the array. (91)

increasing a/c ratios. Figure 50 is, therefore, a plot of the resultant normal stress as a function of the a/c ratio. It should be noted that for a given a/c ratio, a decreasing "a" also reflects as increasing loop density. In both of these cases, the increasing dipole density is accompanied by an increasing cleavage stress.

The data illustrated in Figure 50 is the stress calculated for the point on the midpoint plane directly below a reference dislocation line. If one assumes that a crack will initiate at the point of highest stress, then it becomes necessary to calculate the resultant normal stress for other points along the midpoint plane. Referring to Figure 48b, this is accomplished by varying the location of the reference site (i.e. changing the  $d$  value). Therefore, Figure 51 is a plot of the resultant normal stress for three  $d$  values as a function of geometric arrangement of the dislocations with the individual dipoles. The location of the dislocations is given by  $\Theta = \tan^{-1} \frac{\delta}{a}$  (by Figure 48b,  $2a$  is the vertical separation and  $2\delta$  is the horizontal separation).

The most striking feature of Figure 50 is the shape of the individual curves. For instance, for  $d=0$ , the stress beneath one dislocation line is shown as the other dislocation moves its position due to changes in  $\delta$ . It is evident that the cleavage stress increases as the two dislocations are brought closer together (decreasing  $\delta$ ), and reaches a theoretical maximum where the two dislocations are directly over one another ( $\delta = 0$ ).

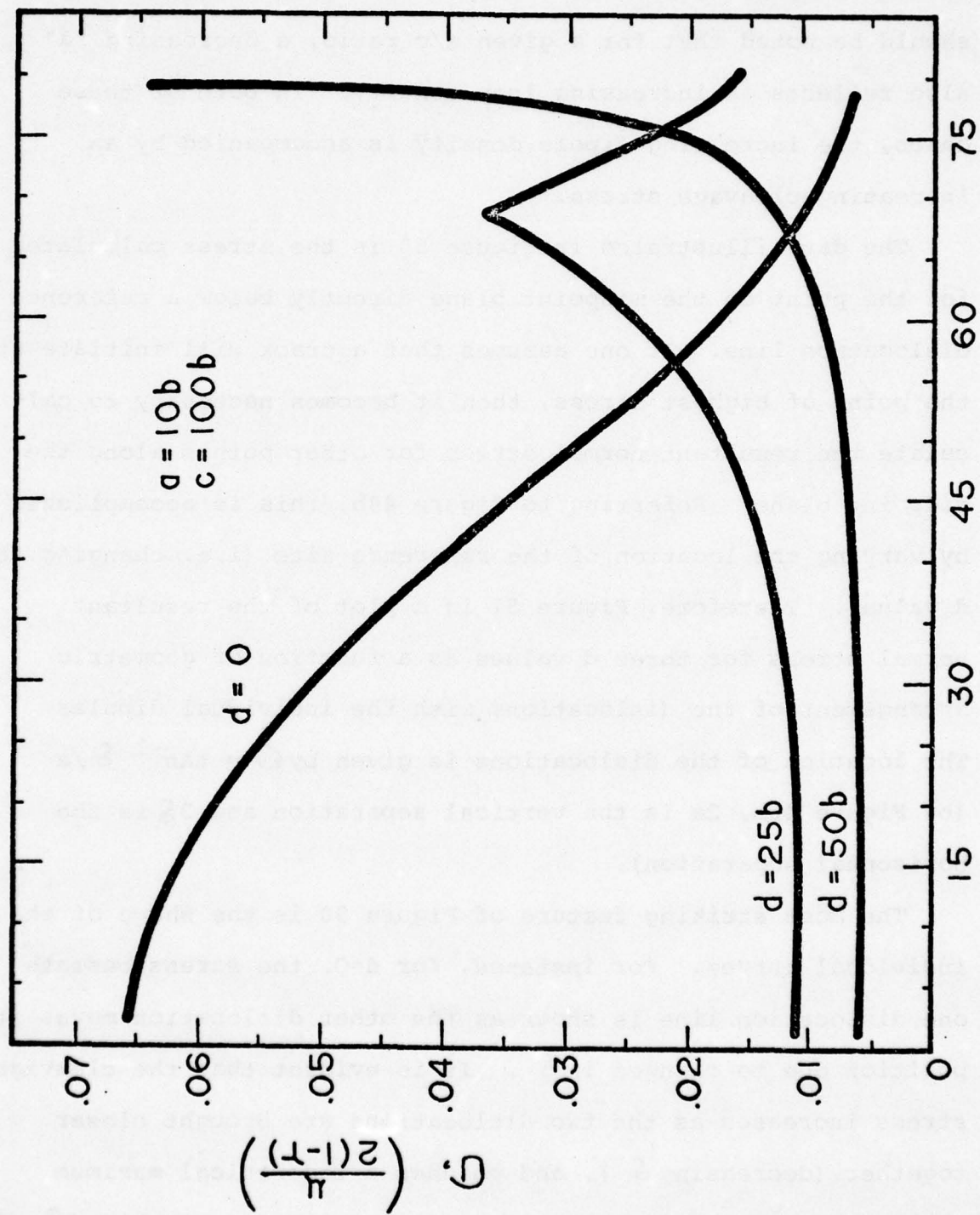


Figure 50. The normal stress on the midpoint plane of a dipole array as a function of the dipole geometry.

$$\Theta = \tan^{-1} d/a$$

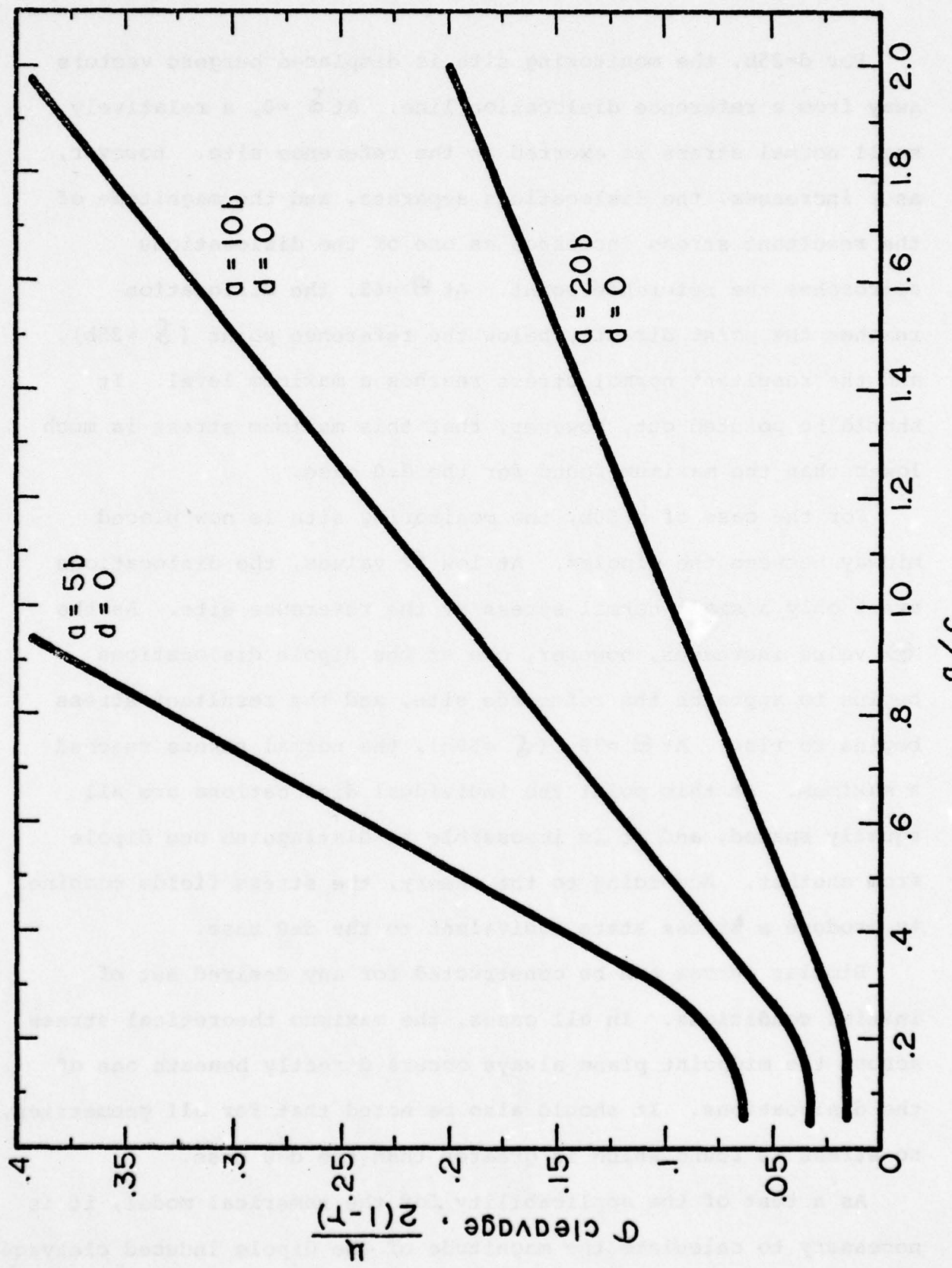


Figure 51. The normal stress of a dipole array for various locations along the midpoint plane as a function of the individual dipole geometry.

For  $d=25b$ , the monitoring site is displaced burgers vectors away from a reference dislocation line. At  $\delta = 0$ , a relatively small normal stress is exerted at the reference site. However, as  $\delta$  increases, the dislocations separate, and the magnitude of the resultant stress increases as one of the dislocations approaches the reference point. At  $\Theta = 68$ , the dislocation reaches the point directly below the reference point ( $\delta = 25b$ ), and the resultant normal stress reaches a maximum level. It should be pointed out, however, that this maximum stress is much lower than the maximum found for the  $d=0$  case.

For the case of  $d=50b$ , the monitoring site is now placed midway between the dipoles. At low  $\Theta$  values, the dislocations exert only a small normal stress at the reference site. As the  $\Theta$  value increases, however, one of the dipole dislocations begins to approach the reference site, and the resultant stress begins to rise. At  $\Theta = 79$ , ( $\delta = 50b$ ), the normal stress reached a maximum. At this point the individual dislocations are all equally spaced, and it is impossible to distinguish one dipole from another. According to the theory, the stress fields combine to produce a stress state equivalent to the  $d=0$  case.

Similar curves can be constructed for any desired set of initial conditions. In all cases, the maximum theoretical stress across the midpoint plane always occurs directly beneath one of the dislocations. It should also be noted that for all geometries, no stress is found which is greater than the  $d=0$  case.

As a test of the applicability for the numerical model, it is necessary to calculate the magnitude of the dipole induced cleavage

stress. After reviewing a number of TEM micrographs of the saturated microstructure with a slip band, the following set of parameters have been selected ( $a=10b$ ,  $\delta = 50b$ ,  $c=500b$ ). These figures appear to be representative, and if anything, they were chosen to be slightly conservative (since McNeil reports  $a=c=5b$  for pure aluminum). When the calculation is performed with  $d=0$  (for the maximum cleavage force across the plane), the model predicts a tensile stress of  $100 \text{ MN/m}^2$ . Although this particular numerical value only applies for the exact geometric array selected, the magnitude of the cleavage stress indicates that the dipole array model does provide a plausible explanation for the low fatigue resistance of these alloys.

In addition to providing a quantitative understanding, the proposed model can also be used to qualitatively interpret the observed fracture morphology. As noted by Feeney et.al. and illustrated in Figures 16,17 and 33, the fracture morphology changes as a function of the stress intensity level. For the load controlled testing mode used in this program, the stress intensity increases as the crack advances away from the free surface. The observed structure can be divided into four separate areas: 1. an initiation region, 2. a mixed mode area, 3. a ductile striation region, and 4. a tensile overload area.

As shown in Figures 17 and 33b, the initiation area is relatively featureless and thought to result from the mechanical cleavage of the metal. The high tensile stresses necessary to cause this type of failure are thought to arise primarily from the high density of dipole loops observed in the dislocation

35                   36                   34  
substructure. As noted by Head, Connors and Grosskreutz, the modulus of the air formed oxide film acts to produce dislocation runout at the free surface. This attractive surface force would act to remove the glissile portions of the dislocation line, 34 but as observed by Grosskreutz, interactions between the existing dislocations act to produce a residual debris structure. It is suggested that the TEM micrographs shown in Figures 18-20 illustrate that the predominate debris feature would be the dipole loop. As the fatigue cycling continued, the dipole density would increase and the accumulated debris levels would act to impede any additional dislocation runout. In a mechanical sense, this would result in the mechanical hardening curve illustrated in Figure 21. Additionally, the surface forces would act to explain how a single specimen could have an appreciable dipole density built up at the surface, and yet, show an interior whose dislocation substructure consisted of entirely of quenched-in helices.

Once the crack has initiated, however, the resultant substructure is a function of the stress intensity. At low stress intensity levels, the crack is known to grow quite slowly, and the substructure is suggested to resemble that near the free surface. This would produce a cleavage-type fracture morphology. However, as the stress intensity increases, the crack is known to propagate at an increased rate. This faster crack propagation implies a fewer number of cycles for any dislocation-dislocation interactions. Therefore, it is suggested that as the stress intensity rises, the substructure should be found to contain fewer

residual dipoles. This would result in a gradual reduction in the dipole produced cleavage stress.

Following the Kelly, et.al., fracture criterion, this reduction in normal stress would result in a shift toward a shear type fracture mode. In the case of the high strength aluminum alloys, this shear mode failure is suggested to be the ductile striation model proposed by Bowles and Broek. This model envisions a (111) type shear as the actual fracture mode with the fracture plane being determined by a geometric addition of all the operating shear planes. Finally, as the crack propagates across the specimens, the net section area can no longer sustain the resultant shear stress. At this point, the specimen fails by tensile overload, and as shown in Figure 42, the morphology clearly indicates a dimple-rupture type failure.

It should be pointed out that this approach necessitates a gradual transition from the cleavage to shear failure mode. Although this transition is difficult to handle from a quantitative standpoint, the fractographic evidence of Figures 16,17 and 33 does provide qualitative agreement. Figure 16 shows the overall fracture morphology characteristic of a polycrystalline fatigue failure. As the fracture extends radially away from the initiation site, there is evidence of additional river line branching. As noted earlier, the greater the degree of branching, the more ductile or shear-like the fracture. Figure 17 is a two-stage carbon replica taken from the transition area. It illustrates mixed morphology characteristic of this region. Finally, the SEM fractograph shown in Figure 33c illustrates the mixed

morphology (river lines and ductile striations) found in single crystal failure.

In concluding this section, the experimental evidence found in this investigation supports the dipole accumulation model of <sup>16</sup> Duquette and Swann as the mechanism of air fatigue failures of the 7000 series aluminum alloys. Additionally, by extending the model beyond the fracture initiation process, it suggests a plausible explanation for the observed fractographic features.

#### B. Aqueous Fatigue

In the preceding discussion, a dipole accumulation model was proposed to explain the air fatigue failures of Al-Zn-Mg alloys. Since the primary objective of this study was a clearer understanding of the corrosion fatigue process in these alloys, the following will explore how this mechanism can interact with the hydrogen available in aqueous environments. It is proposed that this interaction can explain the severe loss of fatigue strength usually encountered under aqueous conditions. Before considering the details of the embrittlement mechanism, it is necessary to review the experimental support for hydrogen as the embrittling species.

If one begins by comparing the polarization curve (Figure 13 with the S-N data shown in Figure 25, a rather striking correlation exists between the magnitude of the cathodic current (hydrogen generation) and the resultant fatigue life. The correlation becomes even stronger if one remembers that the free corrosion rate was found to be of the same order as the current at -1.3v.

This would tend to explain why no additional embrittlement was found at this potential. Apparently, the  $5 \mu\text{a}/\text{cm}^2$  increase in the overall charging rate at  $-1.3\text{v}$  was not large enough to cause a change in the fatigue response. In those cases where the fatigue life did fall, the overall cathodic current was over an order of magnitude larger than the free corrosion rate.

It should be pointed out, however, that the overall cathodic current should not be taken as a quantitative measure of the hydrogen uptake of the specimen. For as was noted in the results section, the higher charging rates resulted in profuse amounts of hydrogen bubbling off the specimen surface. A more quantitative measure of hydrogen uptake is found in the permeation measurements of Gest and Troiano<sup>69</sup> shown in Figure 4.

For example, the permeation levels are constant between the rest potential and the  $-1.3\text{v}$  level. This would indicate that if hydrogen did cause the embrittlement, the mechanical response should be constant over this range. At more cathodic potentials, however, the hydrogen permeation rate begins to rise, and this rise should correspond to a dramatic decrease in the fatigue response. As shown in Figure 25, both of these constraints are supported by this investigation.

Another indication that hydrogen is the embrittling species is found in the stress relaxation data shown in Figures 43-45. These figures clearly illustrate that hydrogen charging can result in a yield drop in this material upon straining. Since it is well accepted that this yielding phenomenon is caused by dislocation break away from a solute or interstitial atmosphere,

these tests qualitatively confirm that a substantial amount of hydrogen enters the lattice during the charging process. The 71 fact that Donavan observed a similar response with a tritium charged aluminum alloy acts to confirm this attractive interaction force between hydrogen and the dislocation substructure.

In addition to providing evidence for hydrogen entry into the lattice, these tests also confirm that the hydrogen is capable of embrittling the alloy. First, the fact that the air specimens were given 24 hour relaxation periods prior to restraining is contrasted with the intergranular failures which occurred during relaxation periods as short as three hours. Secondly, those specimens which failed during the restraining can be divided into two categories, those which failed transgranularly and exhibited a yield point, and those which failed intergranularly and failed to reach their original yield point. This 18 behavior acts to support Swann's observation that a slip band may serve as an alternate diffusion path for the hydrogen.

Before beginning the discussion of the embrittlement mechanism proposed, it is necessary to introduce the concepts developed by 92 Li, Oriani, and Darken. In their thermodynamics of stressed bodies, these authors have shown that the equilibrium interstitial concentration of hydrogen within the stressed body is given by:

$$\ln c/c_0 = \frac{\sigma V_H}{3 kT} \quad (1)$$

where:  $c$  = hydrogen concentration due to an imposed tensile stress

$c_0$  = equilibrium hydrogen concentration under one atmosphere pressure

$\sigma$  = triaxial stress

$\overline{V_H}$  = partial molar volume of hydrogen

K = Boltzman's constant

T = absolute temperature

Therefore, the larger the applied stress, the larger variation between the unstressed (original) hydrogen concentration and the larger, stressed concentration level. If one assumes that the magnitude of this variation becomes a driving force for hydrogen diffusion (i.e. the concentration is directly proportioned to the chemical activity), it can be shown that the higher the applied stress, the lower is the necessary external supply of hydrogen needed to cause embrittlement. Conversely, for a larger external hydrogen supply, a lower applied stress is required to cause failure. Oriani's experimental verification of this approach for steel is shown in Figure 52. The figure plots the hydrogen and deuterium pressure necessary to propagate a stationary crack as a function of the applied stress intensity. The curves indicate that the degree of hydrogen embrittlement is a function of both the available hydrogen level and the localized stress level.

A qualitative agreement with this conclusion is found in Figure 25. This figure shows the S-N response of the Al-Zn-Mg alloy for a number of different polarization levels. In agreement with Oriani's results, the curves show that as the surface hydrogen level is increased (air  $\rightarrow$  free corrosion  $\rightarrow$  -1.75v),

the stress necessary to achieve a given fatigue life is decreased. Additionally, the fractographic evidence tabulated in Figures 26 and 27 suggests that localized hydrogen and stress levels also control the fracture morphology. Figure 26 shows that for a given stress level, the degree of transgranular cracking is related to the polarization (hydrogen) level. Figure 27 shows that for a fixed polarization level, the transgranular morphology is favored by higher stress levels. Although both of these observations are consistent with Oriani's relationship (1), the following discussion attempts to clarify the role of hydrogen in determining the actual fracture morphology.

### 1. Intergranular Failure

As noted earlier, intergranular crack initiation was observed for all specimens except those tested under the combination of high cyclic stresses and high charging rates. In considering the crack initiation phenomenon, it is important to remember that the stresses used in the fatigue portion of the testing program are well below the bulk yield stress. Therefore, although dislocation motion occurs due to micro-yielding, some type of stress intensification is necessary to initiate gross plasticity. The fact that little dislocation movement occurs is supported by the observation of only a low density of helical dislocations in the guage sections of fatigue fractured specimens. This low dislocation density would act to minimize the influence of any dislocation transport mechanism on the intergranular initiation process. Therefore, an alternate, non-dislocation mechanism is proposed to explain this phenomenon.

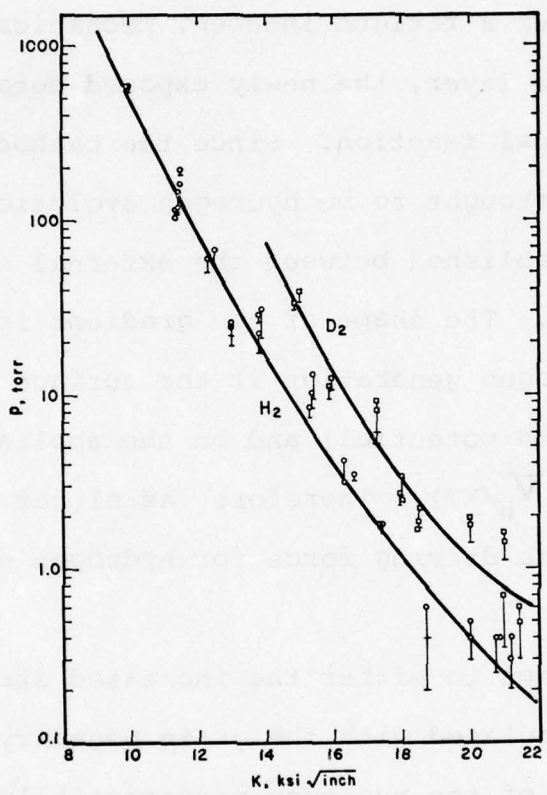


Figure 52

A plot of the hydrogen and deuterium pressure necessary to propagate a stationary crack in 4340 steel. The curves indicate that the degree of hydrogen embrittlement is a function of both the available hydrogen and the localized stress level. (93).

In order for a hydrogen mechanism to be operational, one must first get the hydrogen to the embrittled region. For the case of intergranular fracture, the following sequence is suggested. After a fatigue induced, mechanical rupture of the surface oxide layer, the newly exposed metal undergoes an electrochemical reaction. Since the cathodic portion of this reaction is thought to be hydrogen evolution, a hydrogen gradient is established between the external surface and the specimen interior. The shape of the gradient is dependent on the rate of hydrogen generation at the surface (free corrosion versus applied potential) and on the applied stress level ( $\ln c/c_0 = \sigma \bar{V}_H/kt$ ). Therefore, as either of these quantities increases, the driving force for hydrogen enrichment also increases.

Due perhaps to either the increased strain energy or disorder associated with the grain boundary, it is proposed that the majority of the hydrogen preferentially diffuses along the grain boundary. (This behavior is supported by Swann's mass spectrometry correlations between accelerated hydrogen release and the onset of intergranular cracking). The diffusion process continues until the resultant hydrogen content in the boundaries is large enough to cause decohesion.

At low applied loads, the intergranular crack will continue to propagate by the same mechanism. Since the embrittlement phenomenon is dependent on grain boundary diffusion, the cracking process would be discontinuous; the advance of the crack would be followed by a period of hydrogenation of the

material ahead of the crack. This discontinuous crack growth  
had been observed by Gest<sup>69</sup> for the S.C.C. of 7075-T6. It  
should also be noted that as the crack grows, the resultant  
stress intensity would increase the hydrostatic stress at the  
crack tip. As previously described, this would produce an in-  
creased driving force for the diffusion process, and thereby  
act to intensify the embrittlement process.

Eventually, the stress intensity at the crack tip reaches  
a point where gross plasticity is initiated, and the fracture  
process becomes more complicated due to the proposed inter-  
action of various competing processes. Planar slip produces  
areas of severe strain concentration at those points where slip  
bands intersect grain boundaries (see Figure 18a). This severe  
strain should lower the mechanical strength of the boundaries.  
If this were the only result of plastic deformation, one would  
expect an increased susceptibility to intergranular cracking  
as the local stress intensity rose. However, the various frac-  
tographs indicate the opposite effect, and therefore, suggests  
that the plastic deformation process must either provide a more  
effective transgranular embrittlement process or reduce the  
grain boundary embrittlement process by providing an alternate  
diffusion path for the hydrogen.

Before beginning a discussion of the mechanism of trans-  
granular cracking, it should be mentioned that addition verifi-  
cation of the intergranular embrittlement model can be found in  
the work of other investigators. For example, the mass spectro-  
metry results shown in Figure 3<sup>18</sup> illustrate a direct correlation

between hydrogen evolution and the onset of intergranular fracture. Additionally, the HVEM performed by Montgrain and Swann <sup>18</sup> indicates that failure occurs directly along the grain boundary, with no evidence of associated plasticity or localized corrosion. In addition to supporting the hydrogen embrittlement model, these observations discount the galvanic corrosion and quenched-in inhomogenieties models. Gest and <sup>69</sup> Troiano's correlation of crack growth rate and hydrogen permeation level strongly support hydrogen as the embrittling agent. Finally, the arsenic poisoning experiments of Green <sup>75</sup> and co-workers clearly demonstrates that under the correct conditions, the hydrogen generated in the aqueous corrosion of an aluminum can produce a significant embrittlement of the alloy.

## 2. Transgranular Cracking

Once gross plasticity has commenced, it seems very likely that the fatigue deformation process would produce the dipole structure characteristic of the air fatigue failures. As the earlier discussion indicated, the dipole accumulation process can lead to very large internal cleavage stresses. Therefore, if an embrittled transgranular path could be provided, this stress would greatly enhance the possible transition from intergranular to transgranular cracking.

A possible mechanism for the transgranular embrittlement process has been suggested by Montgrain and Swann. <sup>18</sup> As noted earlier, these investigators have observed that slip band impingement can halt the propagation of an intergranular stress

corrosion crack. Since their mass spectrometry work had indicated that the intergranular failure was the result of high hydrogen levels within the grain boundary, they proposed that the slip band acted to deplete the grain boundary of hydrogen.

Additional support for such a mechanism can be found in the observation of hydrogen induced serrated yielding in various aluminum alloys. This behavior was first reported by <sup>71</sup> Donavan for a tritium charged 5086 specimen. The exact correlation between the tritium release rate and the serrated yielding provides experimental evidence for the dislocation transport mechanism. The fact that similar behavior was noted in the stress relaxation portion of this investigation suggests that this phenomenon may also extend to the 7000 series aluminum alloys. It is suggested, therefore that the embrittled trans-granular path is formed by the dislocation transport of hydrogen into the grain interiors.

Since the transport mechanism must be viewed as part of a dynamic system, it becomes necessary to demonstrate that the kinetics of this phenomenon are consistent with experimental observations. For as the dislocation moves through the matrix, various phenomenon may act to remove the hydrogen from its atmosphere. This action acts to lower the efficiency of the transport process, and in the extreme case, may prevent the accumulation of sufficient hydrogen to cause embrittlement. In general, the dislocation may lose its atmosphere through one of the three general mechanisms: 1) exceeding the critical

velocity for atmosphere drag, 2) annihilation of the dislocation, and 3) interaction with a stable hydrogen sink. Therefore, in each of these areas, one should attempt to define the conditions where an appreciable hydrogen enrichment can occur, and if possible relate these conditions to the various experimental parameters.

As pointed out by Cottrell,<sup>94</sup> the velocity of a dislocation atmosphere couple is given by:

$$v = \frac{D}{KT} \cdot F$$

where D is the diffusion coefficient of the atmosphere species, K is Boltzman's constant, T is the absolute temperature, and F is the force on the couple. Although the localized value of F is dependent on the various internal forces encountered by the dislocation line, it is possible to estimate the upper limit of the force which allows the atmosphere to move with the dislo-

cation line. Following Tien,<sup>95</sup> this force can be taken as the gradient of the hydrogen-dislocation binding energy ( $E_b$ ) over the effective length of the atmosphere. Since Cottrell<sup>94</sup> estimates that the binding energy acts within a distance of 30b, the break away velocity ( $v_c$ ) can be given as:

$$v_c = \frac{D}{KT} \cdot \frac{E_b}{30b}$$

At room temperature, D for unstressed 7075-T6 has been measured as  $2 \times 10^{-9}$  cm<sup>2</sup>/sec,<sup>69</sup> and a reasonable estimate for  $E_b$  can be taken as .3ev.<sup>94</sup> Using these figures, the break away velocity is found to be  $3 \times 10^{-2}$  cm/sec. With this estimate, it is possible to determine the value of  $\epsilon_c$  (the critical

strain rate for dislocation break away). This parameter is easy to monitor experimentally, and it is related to  $v_c$  by:

$$\dot{\epsilon}_c = v_c \cdot b \rho_m$$

where  $\rho_m$  is the mobile dislocation density and  $b$  is the magnitude of the burger's vector.

In order to correlate this equation with experimental evidence, it is necessary to obtain an estimate of the mobile dislocation density as a function of the experimental state of the alloy. In considering corrosion fatigue failures, there are no accurate measurements of the actual mobile dislocation density, therefore, in order to obtain an order of magnitude estimation of the critical strain rate, a few simplifying assumptions will have to be made. First, experimental evidence indicates that a very large dislocation density exists within the plastic zone ahead of a fatigue crack. It is suggested, therefore, that the mobile dislocation density is larger for the propagating crack than in the pre-initiation state of the alloy. Although no precise estimations of the crack tip dislocation density will be made, the discussion will consider the end result of the higher dislocation density. Secondly, for the initiation stage, an order of magnitude estimation will be obtained by using Gilmans relationship between the mobile dislocation density ( $\rho_m$ ) and the plastic strain ( $\epsilon_p$ ). Although this relationship was developed for tensile elongation, it is felt that the relationship will provide a starting point for considering the applicability of the hydrogen transport process.

Gilman found that:

$$\rho_m = M \epsilon_p e^{-\Phi \epsilon_p}$$

where  $M$  is a multiplicative factor (reported by Hordon and Averbach to be  $80 \times 10^9 / \text{cm}^2$  for aluminum), and  $\Phi$  is an attrition or annihilation factor (by curve fitting the tritium release rates reported by Donovan, this factor is estimated to be 55 for aluminum). In applying this equation to the fatigue situation, the peak fatigue strain,  $\epsilon_{f_p}$ , will be used.

In reviewing the fractographic evidence, it was noted that a totally transgranular failure occurred only under the condition of a very high stress and a very high charging rate. The suggested model would imply therefore, that dislocation transport was an important aspect of the initiation process only under those specific conditions. For that reason, the break away strain rate will first be calculated for the case of  $\epsilon_{f_p} = .004$  ( $\sigma = 207 \text{ MN/m}^2 \pm 69 \text{ MN/m}^2$ ). In this case,  $\rho_m$  is found to be  $2.5 \times 10^8 / \text{cm}^2$  and  $\epsilon_c = 1.9 \times 10^{-1} \text{ cm/sec}$ . In order to determine the efficiency of the transport process, it is now necessary to determine the time period for which the  $\epsilon_f < \epsilon_c$ , and use this data to determine the hydrogen transport distance for both dislocation transport and bulk diffusion.

Since the SF-1V applies a sinusoidal cyclic stress at a frequency of 60HZ, the specimen stress can be represented by:

$$\sigma_{\text{peak}} = \sigma_{\text{mean}} + \sigma_{\text{cyclic}} \sin 120\pi t$$

where the  $\sigma$ 's are the various applied stress levels and  $t$  is the time in seconds. If one assumes that within the microstrain

region, the strain is predominately elastic, then the specimen strain rate ( $\dot{\epsilon}_f$ ) is found by dividing the stress equation by the elastic modulus (E), and differentiating it by time. The resultant strain rate is found to be:

$$\dot{\epsilon}_f = 120\pi \epsilon_{\text{cyclic}} \cos 120\pi t$$

where  $\epsilon_{\text{cyclic}}$  is the applied cyclic strain ( $\sigma_{\text{cyclic}}/E$ ).

For the experimental conditions cited earlier (207 MN/m<sup>2</sup>  $\pm$  69 MN/m<sup>2</sup>),  $\dot{\epsilon}_f$  equals  $.377 \cos 120\pi t$  /sec.

By comparing this curve with the calculated break away strain rate of .19/sec. it is found that the dislocation is able to carry its atmosphere for only 17% of the total cycling time. If one assumes that over this time span the average dislocation velocity is  $v_c/2$ , then the hydrogen penetration depth is found to be a product of the average dislocation velocity multiplied by the atmosphere carrying time or  $\left[ \frac{.03}{2} \times .17 \left( \frac{1}{60} \right) \right]$  which equals  $4.25 \times 10^{-5}$  cm/cycle. In comparison, bulk diffusion continues over the entire period, and therefore, its penetration distance is  $(4 \sqrt{Dt} = 4 \sqrt{2 \times 10^{-9} \times \frac{1}{60}}) = 2.31 \times 10^{-5}$  cm/cycle. Since the dislocation transport figures can be used only as order of magnitude estimates, these calculations suggest that the dislocation transport is no more efficient than bulk diffusion. In this case, the hydrogen could diffuse to the grain boundaries at a rate equal to the dislocation transport away from the boundaries. Under these conditions, the proposed models would predict an equal probability for both transgranular and intergranular fracture morphologies. However, an examination

of the experimental evidence suggests that the assumptions used for the dislocation transport calculations may have been too simplistic. For example, the calculated value of  $\dot{\epsilon}_c$  was found to be  $.19 \text{ sec}^{-1}$  and yet, the serrated yielding behavior illustrated in Figures 43 and 44 was obtained with a strain rate of  $.02 \text{ sec}^{-1}$ . This would indicate that the assumed values are at least an order of magnitude larger than the actual case.

This order of magnitude error is probably the result of applying Gilman's mobile density estimates to a precipitation hardened alloy. These estimates were originally made for tensile strains on pure aluminum, and as noted by Kelly and Nicholson,<sup>96</sup> the presence of coherent precipitates acts to raise the initial flow stress of the material to much higher levels than that found in pure metals or solid solution alloys. Therefore, even if one considers the  $.02 \text{ sec}^{-1}$  strain rate as the critical level for dislocation break away, the estimated mobile dislocation density would be of the order of  $2.5 \times 10^7/\text{cm}^2$ . Additionally, one must also remember that the fatigue process also acts to produce a very high density of dislocation debris and sessile defects. These features act to impede dislocation motion, and should further lower the mobile dislocation density.

For the sake of argument, however, let us assume that the critical strain rate for dislocation break away is the experimentally (tensile) observed value of  $.02 \text{ sec}^{-1}$ . This would imply a  $\rho_m$  of  $2.5 \times 10^7/\text{cm}^2$ , but more importantly, it would

drastically lower the time allowable for dislocation transport. By duplicating the hydrogen penetration calculations under these new conditions, the hydrogen can only be transported for 1.7% of the fatigue cycle. This reduces the penetration distance to the order of  $4 \times 10^{-6}$  cm/cycle. Since the bulk diffusion process allows a much greater penetration distance, ( $2.3 \times 10^{-5}$  cm/cycle), the model predicts that initiation morphology is controlled by the bulk diffusion process.

18

As noted earlier, Swann's mass spectrometry data suggests that whenever hydrogen transport is controlled by the bulk diffusion process, the majority of the hydrogen will reside in the grain boundaries. The presence of the hydrogen acts to lower the cohesive strength of the boundary, and thereby, results in an intergranular fracture. Therefore, in the absence of any factor which would alter the mobile dislocation density, the model suggests that the corrosion fatigue process should exhibit an intergranular crack initiation morphology.

As shown in Figures 26 and 27, the majority of the tests did exhibit an intergranular initiation. For these cases, however, as the crack propagated into the specimen, the morphology changed to a transgranular mode. Therefore, if the model is valid, it should be able to explain why the transformation took place. However, before attempting the various calculations, it is necessary to consider the overall effects of introducing a moving crack front into the metal. First of all, it must be remembered that once the crack has

initiated, the area ahead of the crack tip is experiencing plastic deformation. Therefore, the deformation state of the alloy has changed from the microstrain to the macrostrain region. It is anticipated that this change produces at least an order of magnitude increase in the mobile dislocation density, and recent experimental evidence<sup>20,21</sup> indicates that the increase may be even greater. Secondly, as the crack grows, the net section stress will tend to rise. This will be accompanied by an increase in the cyclic strain rate. The magnitude of this shift is expected to remain relatively low (two or three times the original strain rate) during the "true" fatigue propagation stage, and then drastically rise during the tensile overload failure. Finally, it is not expected that the presence of the fatigue crack should greatly affect the other parameters used in these calculations.

With these assumptions, it is now possible to begin a general discussion of the hydrogen transport phenomenon encountered during the propagation process. In order to determine the allowable dislocation transport time, it is again necessary to set  $\dot{\epsilon}_c$  equal to  $\dot{\epsilon}_f$  and solve the following equation:

$$v_c \rho_m b = 120\pi \epsilon_{\text{(cyclic)}} \cos 120\pi t$$

Ideally it would be desirable to obtain an empirical relationship between the applied  $\Delta K$ ,  $\epsilon_{\text{cyclic}}$  and  $\rho_m$ . Unfortunately, no such correlations have been reported. Therefore, the quantitative nature of this section must be limited to investigating the trends present as the crack begins to propagate. As

noted above, it is assumed that the propagating crack will produce an increase in both  $\rho_m$  and  $\epsilon$  cyclic. For the sake of this discussion,  $\epsilon$  cyclic will be assumed to have a fixed value of .0035 (the elastic strain corresponding to a cyclic stress equivalent to 50% of the bulk yield stress). This is a 3.5 fold increase in the value used in the previous calculations and is used to represent an extremely large increase in the cyclic strain rate (i.e. a case most disfavorable to the dislocation transport model). With this factor fixed, one can calculate the penetration depth as a function of the assumed mobile dislocation density. The results of these calculations are shown in Table IV.

These calculations indicate that even for strain rates in excess of  $1 \text{ sec}^{-1}$  it is only necessary to achieve mobile dislocation densities of near  $10^9/\text{cm}^2$  in order to allow hydrogen transport over the complete fatigue cycle. Additionally, if one assumes that the mobile dislocation density is a function of the crack tip stress intensity level, the model suggests that the higher  $\Delta K$  levels should result in a greater degree of transgranular cracking. This fact was experimentally demonstrated in fractographic evidence illustrated in Figure 27. Finally, the table acts to suggest a possible explanation for the totally transgranular failures encountered under the high stress, high polarization conditions. For as noted in Figures 28-31, the totally transgranular cracking is associated with the occurrence of the caustic tunnelling phenomenon. It is suggested that under these conditions, the tunnel will act as a stress

Table IV

$\dot{\epsilon}_{c, \text{max}}$ (sec $^{-1}$ )	$\dot{\epsilon}_{f, \text{max}}$ (sec $^{-1}$ )	% of cycle time where $\dot{\epsilon}_c > \dot{\epsilon}_f$	$d_1$ (dislocation transport distance/cycle) (cm)	$d_D$ (bulk diffusion distance/cycle) (cm)	$d_1/d_D$
$10^7$	$7.5 \times 10^{-3}$	1.3	.18%	$4.5 \times 10^{-7}$	$2.31 \times 10^{-5}$
	$7.5 \times 10^{-2}$	1.3	1.8%	$4.5 \times 10^{-6}$	$2.31 \times 10^{-5}$
$10^8$	$7.5 \times 10^{-1}$	1.3	18%	$4.5 \times 10^{-5}$	$2.31 \times 10^{-5}$
	$1.3$	1.3	100%	$2.5 \times 10^{-4}$	$2.31 \times 10^{-5}$
$10^9$					
$1.76 \times 10^9$					

concentrator and thereby, raise the local dislocation density to the point where the transgranular embrittlement process becomes competitive with the intergranular mode. (A more thorough discussion of the tunnelling process will be provided in a later section of this discussion).

Although this discussion of the dislocation break away phenomenon does offer a great deal of insight into the failure process, the data presented in Figure 26 suggests that the overall embrittlement process is also a function of the hydrogen charging rate. This figure lists the type of fracture morphology observed for fatigue specimens as a function of the applied potential. The results indicate that as the potential becomes more cathodic (i.e. the hydrogen charging rate increases), the morphology shifts toward a totally transgranular failure. According to the proposed model, this would imply that the higher surface concentrations resulted in a more efficient hydrogen transport. A possible explanation for this effect can be found in a recent model proposed by Hirth and Johnson.<sup>99</sup>

The model was proposed to calculate an upper bound for the enrichment process occurring during a tensile test in a hydrogen environment. The model estimates the kinetic effects of the two opposing processes: 1. the dislocation transport of hydrogen from the external source to the internal site, and 2. the bulk diffusion of the hydrogen from the internal site to an external sink. The model assumes that the observed strain rate is the result of internal dislocation annihilation, and that these dislocations are transporting a saturated hydrogen

atmosphere. Under these assumptions, the hydrogen arrival rate per unit time ( $I_1$ ) is given by:

$$I_1 = \frac{\dot{\epsilon} \lambda}{b} \cdot \eta \cdot a$$

where  $\dot{\epsilon}$  = strain rate

$\lambda$  = the two dimensional spacing of the internal sinks

$b$  = burger's vector

$a$  = atom spacing along the dislocation

$\eta$  = number of hydrogen atoms/atom site along the dislocation

The bulk diffusion rate away from the internal sink is viewed as a line source of hydrogen emitting  $I_D$  atoms per unit time into the surrounding material with a planar surface acting as the diffusion sink. In this case, the internal concentration  $C_1$  is related to the sink concentration  $C_0$  by the following equation:

$$\frac{C_1 - C_0}{I_D} = \frac{1}{2\pi D} \cos h^{-1} \left( \frac{L}{r_0} \right)$$

where  $D$  = diffusion coefficient of the hydrogen

$L$  = distance from the internal site to the external sink

$r_0$  = radius of the internal site

Under steady state conditions, the arrival rate ( $I_1$ ) equals the departure rate ( $I_D$ ), and therefore, the resultant internal concentration of hydrogen is given by:

$$C_1 = \frac{\lambda \dot{\epsilon} \eta}{2\pi a b D} \cdot \cosh^{-1} \left( \frac{L}{r_0} \right) + C_0$$

It should be noted, however, that the model was derived for steady state tensile behavior, and therefore, it is felt that numerical solutions to the above equations would not be directly applicable to the corrosion fatigue case of interest in this study. Instead, the resultant equation should only be used to discuss general trends. First of all, it should be noted that the  $\eta$  term may be dependent on the external source concentration. For low charging rates, it is probable that the charging rate would be insufficient to produce a saturated atmosphere around the dislocation. This would reduce the hydrogen along the dislocation line ( $\eta$ ), and result in a lower internal hydrogen level. Secondly, this equation would only apply to the case where  $\dot{\epsilon}_f < \dot{\epsilon}_c$  (i.e. below the break away strain rate). For very high strain rates, the internal hydrogen concentration would be a function of the bulk diffusion rate. Next, the original model was developed for the case of total dislocation annihilations. From an enrichment standpoint, the same general conclusions can be reached if the dislocation were to interact with any stable hydrogen sink with a spacing of  $\lambda$ . In these cases, the internal hydrogen level increases as the sink spacing decreases (i.e. the hydrogen enrichment rises as the sink density increases). Finally, since the  $\cos h^{-1} (L/r)$  is an always positive, increasing function and all the pre-exponential terms are also positive, the equation predicts that the internal hydrogen level will always be greater than the external source concentration. Therefore, if the internal hydrogen level can be taken as a relative measurement of the embrit-

lement process, the model predicts that the degree of transgranular embrittlement should increase with increasing cathodic potentials.

This general behavior is experimentally documented in this investigation. First of all, a comparison between the polarization diagram (Figure 14) and the S-N behavior of the alloy (Figure 25) shows a direct correlation between the overall fatigue life and the degree of cathodic charging (i.e. surface hydrogen concentration). For a given stress level, the fatigue life decreases with increasing hydrogen charging levels. Secondly, the fractographic evidence listed in Figure 26 illustrates a shift towards a more transgranular failure with increasing charging rates. This shift is also consistent with the preceding analysis. As noted earlier, the onset of transgranular cracking is thought to occur whenever the dislocation transport process can provide sufficient hydrogen to embrittle a transgranular path. The Hirth and Johnson model predicts that the efficiency of the transport process will rise as the external hydrogen level is increased. Therefore, for a given stress level, the number of fatigue cycles to reach the critical hydrogen level should decrease with increasing charging levels. This results in the observed larger proportion of transgranular fracture.

In addition to establishing which factors affect the applicability and efficiency of the dislocation transport process, it is also necessary to consider how hydrogen interaction with the alloy results in the observed embrittlement.

As noted earlier, the hydrogen embrittlement process has been observed in other alloy systems, and as a starting point, it seems logical to consider the embrittlement models proposed for these systems. These models can be grouped into three general areas: 1. high pressure gas build up, 2. hydride formation, and 3. lattice separation.

The high pressure hydrogen model was proposed by Broom<sup>29</sup> and Nicholson to explain the corrosion fatigue behavior of precipitation hardened aluminum alloys. The model suggests that the supersaturated hydrogen migrates to various accumulation sites within the metal. At these points, the hydrogen recombines to form pockets of high pressure gas. The internal gas pressure results in a hydrostatic stress around the pocket. When this stress is added to the applied fatigue stress, the gas pocket becomes an ideal nucleus for a propagating crack. The model further suggests that once a crack has nucleated, this process repeats itself within the hydrostatic stress field ahead of the growing crack. Although this process has been thoroughly documented for other metal systems (for example, 100 101 see Thompson or Troiano) the model does not provide an explanation for the observed fractographic features found in this investigation. For example, the various fractographs show no evidence of gas pocket formation. Additionally, the fractograph of the tensile fracture shown in Figure 42 clearly shows the occurrence of a ductile (dimpled rupture) fracture morphology. The high pressure gas model fails to provide any strong arguments to explain the change from this morphology to the cleavage-

like morphology seen in the corrosion fatigue case (see Figure 23,34-36). Therefore, it appears doubtful that the high pressure gas model is appreciable to this system.

Some metals, particularly those belonging to group IVa (Ti, Zr, Hf) and to group Va (V, Nb, Ta), are known to form a metal hydride at relatively low hydrogen concentrations. For most of these reactions, the phase transformation results in a large volume change. This can result in rather severe strains accompanying the hydride formation. When this is coupled with the brittle nature of the hydride phases, the result can lead to a substantial reduction in ductility. Since no evidence of hydride formation was observed, however, it appears unlikely that this model applies to the Al-Mg-Zn system.

The lattice separation model was originally suggested by 101 Troiano to explain the hydrogen embrittlement of steels. The model is quite similar to those used to explain the mechanism behind liquid metal embrittlement. It proposes that the hydrogen interacts with metal to lower surface energy across 102 the cleavage plane. According to Kamdar, this action can be interpreted as a lowering of the idealized cleavage stress

( $\sigma_{TH}$ ) without affecting the theoretical shear stress ( $\tau_{TH}$ ).  
22  
Therefore, according to the Kelly, Tyson, Cottrell criterion discussed earlier, the resultant decrease in the ( $\sigma_{TH}/\tau_{TH}$ ) would enhance the probability of a crystallographic failure.

Kelly, et.al. have suggested that an estimate for  $\sigma_{TH}$  may be obtained from the following:

$$\sigma_{TH} = \left( \frac{E' \gamma}{Y} \right)^{1/2}$$

where  $\gamma$  is the spacing of the crystal planes with surface energy  $\gamma$  and  $E'$  is the value of Young's Modulus across the plane. Gilman has suggested that the surface energy may be calculated as follows:

$$\gamma = \frac{E'}{y} \left( \frac{a}{\pi} \right)^2$$

where  $a$  is the atomic radius in the cleavage plane. Wanhill has combined these equations to show that

$$\sigma_{th} = \left( \frac{\pi}{a} \right) \gamma$$

He also states that since  $a$  is independent of direction in fcc metals, one need only to obtain  $\gamma$  for predictions of the necessary cleavage planes.

Unfortunately, the literature has conflicting values for the surface energy of the various crystal planes. Using Gilman's approach, Wanhill calculates the energies to be

$$\{110\} = .50 \text{ J/m}^2, \{100\} = .64 \text{ J/m}^2, \text{ and } \{111\} = .67 \text{ J/m}^2.$$

Burton and Jura, report just the opposite ranking of  $\{111\}$  2.21J/m<sup>2</sup>.,  $\{100\}$  2.93J/m<sup>2</sup>, and  $\{110\}$  3.03J/m<sup>2</sup>. Since both methods rely upon experimental data, the correct ranking of the planes must await further work. It is interesting to note, however, that neither ranking suggests that the  $\{100\}$  76

plane should be the cleavage plane, and it is this plane which forms the path for the cleavage fracture observed under corrosion fatigue conditions. This apparent discrepancy may be resolved with an undisputed resolution of the actual surface energies. It should also be noted that Wanhill has observed cleavage along  $\{100\}$ ,  $\{111\}$ , and  $\{110\}$  planes,

and, therefore, the anisotropy in  $\gamma$  may be quite small.

In contrast to lattice separation, it is also possible that the observed embrittlement may be due to an interfacial separation process. By its very metallurgical structure, the precipitation hardened alloy has a very large density of particles throughout its structure. If the hydrogen were to act to lower the interfacial surface energy between the precipitate and the matrix, the result could provide a nearly continuous transgranular cleavage path. Additionally, since the precipitate exhibits a habit plane with the matrix, the interfacial fracture process should occur along specific crystallographic planes. It should also be noted that since the precipitates are known to be semi-coherent along the slip plane, it is relatively easy to foresee a possible dislocation precipitate interaction which would act to remove hydrogen from the dislocation as it passed through the particle. Finally, it must be remembered that the hydrogen is attracted to the dislocation in an effort to relieve the associated strain energy. Since the particle is not totally coherent with the matrix, there exists a misfit strain across the various particle-matrix interfaces. It is suggested that in an effort to reduce this strain, the hydrogen might also be attracted to these interfaces, and thereby, act to reduce the cohesive strength across the interface.

Unfortunately, empirical justification of this mechanism is extremely difficult to obtain. First of all, the rather small size of the particles makes it difficult to experiment-

ally observe whether the crack actually propagates along the precipitate interface. Secondly, since at least eight separate crystallographic relationships have been reported for the  $MgZn_2$  particles, it is difficult to correlate the observed cleavage plane with the individual precipitate interfaces.<sup>3</sup> It should be noted, however, that Mondolfo reports that the frequency of each crystallographic relationship is inversely related to its misfit. Of the eight reported habit planes, the  $(100\gamma) \parallel (100Al)$  and  $(001\gamma) \parallel (011A)$  has the lowest interfacial misfit. Therefore, the precipitate with the greatest probability of occurrence provides a potentially embrittled interface which correlates quite well with the observed macroscopic cleavage plane.

This particular mechanism is attractive for these additional reasons. First, as noted earlier, the solubility of hydrogen in pure aluminum is extremely low. The precipitate interface provides a site with a higher degree of disorder than the bulk matrix. Therefore, rather than reside in the matrix where it is not easily accommodated, the precipitate boundary provides an alternate accumulation site. Secondly, the work of Montgrain and Swann<sup>18</sup> clearly indicates that hydrogen is capable of providing interfacial separation, and therefore, this mechanism suggests that the same mechanism might also result in what has been characterized as macroscopic transgranular cleavage.<sup>76</sup> Finally, the liquid-metal embrittlement studies of Wanhill<sup>104</sup> indicate that 7075 type alloys are capable of cleavage on the three low index planes (100, 110, and 111), and the precip-

itate interfacial embrittlement mechanism might explain why the  $\{100\}$  is favored by the corrosion fatigue process.

To summarize the transgranular cracking model, it is suggested that at sufficiently high densities, the fatigue generated dislocations act to produce a hydrogen embrittled transgranular path. In most cases, (except the caustic tunnelling), the necessary mobile dislocation density was not present at the crack initiation stage. Under these conditions, the bulk diffusion of hydrogen resulted in an intergranular crack initiation. As the intergranular crack propagated, however, the resultant increased stress intensity produced a higher level of dislocation motion. Due to an attractive interaction, the dislocations began depleting the grain boundaries of hydrogen, and began transporting the embrittling species to the grain interiors. At some point, the hydrogen levels along the transgranular path will reach a level where this path becomes more embrittled than the grain boundaries. At this point, the crack morphology will begin to transform from predominately intergranular to predominately transgranular. Throughout the transport process, the overall efficiency is believed to be a function of both the local dislocation dynamics ( $\rho_m, \dot{\epsilon}$ , etc.) and the surface hydrogen level.

### 3. Single Crystal Failures

Thus far, the experimental support for the proposed model has been provided by discussing the results obtained on the polycrystalline specimens. As a further verification of the

model, this discussion will attempt to correlate the single crystal behavior with the proposed fracture mechanisms.

In making these correlations, it is tacitly assumed that the removal of the grain boundary structure does not greatly alter the transgranular fracture process. This assumption is supported by the S-N data illustrated in Figure 32. This figure shows the excellent agreement between the relative fatigue response for the polycrystalline and single crystal specimens. As mentioned earlier, the air specimen was tested above the C.R.S.S., and its fracture morphology was found to be consistent with the dipole accumulation model.

As in the case for the polycrystalline specimens, the aqueous fatigue tests were also tested below the stress necessary to initiate gross dislocation motion (in this case, the C.R.S.S.). Once again, if the dislocation transport model is valid, some mechanism must be found to provide a stress concentrator sufficient to produce localized flow. In all but one case, the stress concentration was formed strictly by a localized corrosion process. In the free corrosion case, the crack appeared to emanate from a pit. (Unfortunately, the entire fracture surface was badly corroded, and therefore, exact resolution of the defect was difficult.) In the -1.3v case, the defect was a gently rounded area of what appeared to be preferential caustic attack. In the -1.75v case, two of the three specimens were found to have extensive caustic attack at the initiation site (the third specimen will be discussed in more detail shortly).

In all these cases, the nature of embrittlement depended on both the charging potential and the specific tensile orientation.

For example, Figure 34 illustrates the fracture morphology for specimen #134 (-1.3v and <532> tensile orientation). The low charging potential used on this specimen produced a quasi-cleavage failure near the initiation site, however, as the crack progresses away from its origin, the morphology changes to one of a surface roughening. But as shown in Figure 36, this surface roughening is believed due to the overlap of two river line patterns. In considering the overall fracture morphology of this specimen, it should be noted that the separate river line patterns show an increasing cleavage character as they approach the external surface. This suggests that the conditions used in this test combined to result in a relatively low hydrogen transport level. Since the specimen was oriented near single slip conditions (thereby providing the maximum dislocation penetration per unit strain), the proposed model suggests that the overall transport efficiency be controlled by the low surface hydrogen concentration. In considering the implications of the Hirth and Johnson model discussed earlier, the low efficiency could have resulted from either the transportation of low hydrogen level atmospheres (low  $\eta$ ) or an increased outward diffusion rate resulting from the low surface hydrogen level ( $C_o$ ).

In contrast to that morphology, Figure 34b shows the fracture morphology of specimen #139 (-1.75v, <542> ).

Tested at the higher charging rate, this specimen (of nearly the same orientation as #134) shows much stronger cleavage markings. In fact, the transport efficiency was sufficient to totally embrittle the entire specimen cross section. The strong river lines emanate from a small perimeter of caustic attack, and extend across the entire specimen. In contrast to all other specimens tested, this specimen had no evidence of tensile overload. As one might expect from the proposed model, this specimen suggests that the transport efficiency is maximized for a specimen oriented at near single slip and charged at a very high rate.

As noted earlier, a specimen of a radically different tensile orientation was also tested at -1.75v. Figures 37-41 illustrate various aspects of the fracture process for this <110> tensile aixs specimen. Figures 37 and 40 show the overall topography, and suggest that the transgranular embrittlement of this alloy can occur along more than one crystallographic path. This is supported by the angular shifts illustrated in the metallographic profile of this area shown in Figure 41. Although size constraints prevented positive determination of the exact crystallographic relationships, these figures do provide qualitative evidence for the role of hydrogen in the fracture process.

If one assumes that the resultant hydrogen concentration decreases as a function of the distance into the specimen (as predicted by the Hirth and Johnson model), the character of the fracture surface serves to reflect the degree of embrittlement.

AD-A077 461

RENSSELAER POLYTECHNIC INST TROY N Y DEPT OF MATERIAL--ETC F/G 11/6  
THE CORROSION FATIGUE BEHAVIOR OF A HIGH PURITY AL-ZN-MG-CU ALLOY--ETC(U)  
NOV 79 E F SMITH, D J DUQUETTE

N00014-75-C-0466

NL

UNCLASSIFIED

3 OF 3  
ADA  
077461



END  
DATE  
FILED  
12-79  
DDC

As shown in Figure 39, the severe hydrogen charging rates experienced at the external surface are capable of producing a nearly featureless fracture morphology. This type of topography is characteristic of a brittle failure. The fact that no crack arrest marks can be found on the initial plateau acts to support the fact that this portion of the failure occurred with little associated plasticity. The featureless, initiation morphology is very similar to that noted by Duquette and co-workers<sup>57,85</sup> for the commercial 7075-T6 alloy. In their work, the fatigue crack was found to emanate from the base of a corrosion pit. As noted earlier, the environment inside a propagating pit is quite acidic, and therefore, provides a ready source of hydrogen for the embrittlement process. In both cases, the featureless region is the result of high hydrogen levels and a strong stress concentrator, i.e. either a corrosion pit (Duquette) or caustic tunnels (see Figure 38).

As the crack progressed inward, the hydrogen level decreases and the hydrogen induced separation interacts with the shear mode failure process to produce the more characteristic quasi-cleavage, or river line, type morphology. This behavior also corresponds well to the observed fatigue morphology reported for the commercial alloy. Finally, as the crack out runs the effect of the external environment, the morphology completely loses its cleavage character. This roughened structure leads to tensile overload.

In addition to illustrating the various morphological effects of the hydrogen embrittlement process, this specimen

also acts to confirm the presence of the caustic tunnelling phenomenon. Figures 38 a and b are an SEM fractograph and two-stage carbon replica taken from one portion of the initiation plateau shown in Figure 37. Both figures indicate that this section of the fracture surface once contained a series of long, narrow tunnels running away from the exterior surface. The figures indicate that the tunnels ran both along and into the eventual fracture plane. The square cross section of those running into the fracture plane suggests that the tunnels may be crystallographic in nature. It should be noted that similar defects were also observed in a number of the polycrystalline specimens. (For example, see Figures 28-31). In all cases, the only specimens which exhibited any tendency to tunnel were those polarized to -1.75v.

Since the role of the tunnels appears to be limited to that of a geometric stress concentrator, no systematic study of the process was performed. However, it should be noted that this study appears to provide the first observation of the tunnelling process under cathodic polarization conditions. In other reported cases,<sup>58-62</sup> the tunnelling has been observed to occur under either free corrosion or anodic polarization conditions.

In discussing any mechanisms for tunnel formation, it is usually assumed that the long narrow geometry of the tunnel is the result of a process which acts to inhibit lateral dissolution.<sup>58</sup> Swann suggests that this could be accomplished by either electrochemical plating of a mobile species on the side walls or preferential dissolution of an active species from

the walls. Although these processes can be used to explain the structures found in the metallic systems studied by 58 Swann, it does not explain how the process would occur in non-metallic systems. In these systems, the mechanism is probably chemical rather than electrochemical.

In the specific case of tunnel formation in Al-Zn-Mg-Cu alloy under severe cathodic charging conditions, either mechanism might apply. From an electrochemical standpoint, both Zn and Cu are noble to Al, and therefore, the possibility exists for the operation of either electrochemical mechanism. However, since the tunnelling process was only observed under those conditions which provided an excess of hydroxyl ions at the surface (i.e. potentials where the reduction of water is the predominate cathodic reaction), the amphoteric nature of aluminum makes it possible that the tunnels are the result of a strictly chemical process. In either case, the tunnels do provide a very effective stress concentrator, and as noted in Figure 28, can aid in the transition from an intergranular to transgranular fracture morphology.

### C. Yield Point Experiments

The preceding discussion has considered the observed corrosion fatigue response to be the result of a hydrogen embrittlement model. During the course of that discussion, a model was developed which suggested that the fatigue fracture morphology of the alloy was dependent on both the local hydrogen content and the local stress level. Finally, it attempted to use the model in an effort to correlate the various experimental parameters with the observed behavior. This final portion of the discussion will attempt to extend the proposed hydrogen embrittlement model to explain the results obtained in the various yield point experiments.

As noted in Figures 43-45, the yield point experiments were conducted on the alloy in a number of different metallurgical states. These states ranged from the as-processed material to a precipitation hardened single crystal sample. These specimens represented variations in both the initial dislocation substructure and the precipitate structure.

Before considering the individual cases, it should be pointed out that the results of the cathodically charged, stress relaxation tests can be divided into two general categories: those which failed intergranularly and showed no yield drop, and those which failed transgranularly and exhibited a yield point upon restraining. This correlation suggests that the observed yielding response is dependent on the four major factors which determine the fracture morphology of the alloy: 1. the grain boundary hydrogen concentration, 2. the transgranular hydrogen concentration,

3. the total grain boundary stress (the applied stress plus the slip band impingement stress), and 4. the total transgranular stress (the applied stress plus the dipole induced stress).

As noted by Ryum and Duquette,<sup>89</sup> the tensile deformation mode used in these tests produces primarily long, straight screw dislocations with a relatively low density of dislocation loops. Under these conditions, the resultant dipole stress is very low<sup>16</sup> and can be ignored. However, as noted by Spiedel,<sup>2</sup> the opposite is true for the slip band impingement stress. In the T-6 condition, tensile deformation exhibits an extremely planar character, and the resultant pile-up stresses can be quite appreciable. It should also be noted that in contrast to the fatigue case, there is no stress reversal occurring during the test. For this reason, the total hydrogen transport process must occur upon initial yielding. With these factors in mind, an effort will be made to interpret the observed results on a case by case basis.

As shown in Figure 43a, the as processed material exhibited a slight yield drop for the test conducted in an air environment. Since the material was tested in the as rolled condition, it had not received a precipitate forming heat treatment. The magnitude of the yield drop can then be taken to reflect the binding force between the alloying elements (in solid solution) and the mobile dislocation density.

In considering the polycrystalline, T-6 treated specimens, the specimen has received both a solutionizing (resulting in complete re-crystallization) and an aging heat treatment. This results in

a very low mobile dislocation density, and thereby results in a low break away strain rate. This factor would combine to produce a low transport efficiency of hydrogen away from the grain boundaries. When this is coupled with the expected impingement stresses, the results would favor an intergranular failure mode. As noted in Figure 44, the restraining of a T-6 specimen under these conditions resulted in no observable yield point and an intergranular failure.

In addition to using the as heat treated specimens, a number of tests were attempted with specimens which were cold rolled or fatigued in air after the T-6 treatment. These procedures would greatly increase the initial dislocation density, and it was hoped that this would improve the transport efficiency to the point where a yield point might be observed. However, in addition to raising the dislocation density, these processes also raised the impingement stresses, and in contrast to the fatigue case, the entire transport process must occur upon initial yielding. The resultant transport efficiency was not enough to overcome the grain boundary stress and hydrogen levels, and these tests also resulted in an intergranular failure with no yield drop.

In an effort to remove the grain boundary effects, a stress relaxation and restraining test was also performed on a T-6 heat treated single crystal. As shown in Figure 45, once the grain boundary failure problem is removed, the dislocation transport process is efficient enough to exhibit a yield point drop upon restraining. This result experimentally confirms the ability of the dislocation transport process to operate during the corrosion

fatigue testing of the alloy. It should also be noted that this result implies that the transport process was operational during the polycrystalline relaxation tests, but the resultant yield drop could not be observed because the grain boundaries failed prior to the dislocation break away.

Finally, in the as processed material, TEM examination revealed that this material had a very high initial dislocation density. The dislocation density was arranged in almost a continuous tangle that made resolution of individual dislocation segments extremely difficult. It is important to note that the deformation network was composed of predominantly dislocation tangles, and no evidence of the planar slip bands could be found. In this case, since the dislocations were uniformly distributed in the grain, the grain boundary impingement stress should be low. Also, since the initial dislocation density was so very large, the total amount of hydrogen transported (per unit strain) would be much greater. It should also be noted that since a small yield point was found in the un-charged specimen, the original, solute atmosphere would act to slow the dislocation velocity, and therefore allow more time for hydrogen interaction. All these factors act to favor the transgranular hydrogen transport mechanism, and as shown in Figure 43b, the most dramatic yield points were found when this material was tested under the hydrogen charging conditions.

Summary and Conclusions

This investigation has attempted to provide a basis for understanding the corrosion fatigue process in the high strength aluminum alloy. The experimental evidence indicates that the fatigue response of the metal is a function of the local hydrogen concentration. It has been suggested that the local hydrogen level is controlled by the relative efficiencies of the grain boundary diffusion process and the dislocation transport phenomenon. A semi-quantitative model was used to estimate where the dislocation transport process would be dominant, and a second model suggested an upper limit for the degree of hydrogen enrichment by dislocation transport. Both of these models were consistent with the observed fatigue response, and therefore, were used to interpret the yield point results. Finally, although this investigation indicates that the fatigue response is controlled by a hydrogen embrittlement phenomenon, the experimental evidence does not reveal how the hydrogen causes the lattice decohesion process to occur. This particular question deserves and requires a great deal more attention from the scientific community.

In closing, this investigation suggests the following conclusions:

1. For fatigue failures in laboratory air, the experimental evidence supports the dislocation dipole mechanism proposed<sup>16</sup> by Duquette and Swann to explain the quasi-cleavage fatigue fracture of high strength aluminum alloys.
2. The Al-Mg-Zn alloy system has been shown to suffer hydrogen

embrittlement in an aqueous environment.

3. The degree of embrittlement is found to be directly related to the surface hydrogen level.

4. The experimental observation of a hydrogen induced yield point indicates that the alloy is susceptible to hydrogen enrichment as the result of hydrogen transport in the atmosphere of a mobile dislocation.

5. The hydrogen distribution in the alloy affects the fracture morphology.

6. The actual initiation and propagation morphologies are strongly dependent on both the local stress and the local hydrogen level.

7. The alloy is susceptible to corrosion tunnelling at high cathodic polarization levels.

8. A hydrogen embrittlement mechanism can be used to explain the occurrence of both intergranular and transgranular fracture morphologies. The fracture morphology is determined by the relative efficiency of two competing processes: grain boundary diffusion and hydrogen transport in a dislocation atmosphere.

Suggested Experiments

1. Refine the strain anneal technique to grow larger single crystal specimens. With larger cross-sectional areas, it should be possible to determine the exact crystallographic relationship for the ductile, cleavage, and quasi-cleavage fracture morphologies observed in this investigation.
2. Perform corrosion fatigue experiments under anodic polarization. The hydrogen permeation data of Gest and Troiano suggests that a hydrogen embrittlement mechanism should be operational under these conditions. However, verification of this fact would require correlation between the reported hydrogen levels and the resultant fractographic features and mechanical properties (i.e. yield point, S-N data, etc.).
3. Perform bake out experiments similar to those reported by other <sup>69,85</sup> investigators. This would confirm the reversibility of the embrittlement process for the high purity alloy.
4. Perform more detailed experiments to determine the predictive nature of the quantitative models introduced in this investigation. For example: a. Perform corrosion fatigue tests at various frequencies and correlate the depth of the embrittled zone to the carrying time of the dislocation. b. Perform hydrogen permeation measurements as a function of a constant static stress, and strain rates above and below  $\dot{\epsilon}_c$ . The resultant permeation would reflect the efficiency of the transport process. c. Perform hydrogen permeation on single crystalline and polycrystalline specimens to determine the effects of grain boundary diffusion.

5. Use a wide variation in the heat treating parameters (solutionizing time and temperature, aging time and temperature, quench rate) to provide changes in the precipitate structure of the alloy. These changes should provide information regarding possible interactions of the precipitates with the fracture process.
6. Perform corrosion fatigue experiments in a number of different electrolytes. The electrolytes should be chosen to provide variations in the hydrogen re-combination kinetics, the protective properties of the oxide structure, and intergranular corrosivity.
7. Perform a systematic study of the tunnel corrosion phenomenon, under both anodic and cathodic polarization conditions.

References

1. Epstein, S.G., Aluminum and Its Alloys, Technical Report T-3  
The Aluminum Association, New York, New York, 1973
2. Spiedel, M.O., in Fundamental Aspects of Stress Corrosion Cracking, ed. R. Staehle, NACE, Houston, Texas 1969, p. 561
3. Mondolfo, L.F., Metallurgical Reviews, 16, 110, 1971
4. Dix, E.H., Trans. ASM, 42, 1057, 1950
5. Dix, E.H., Trans. ASM, 35, 130, 1945
6. Hunsicker, H.V., Aluminum, Volume 1, ed. K.vanHorn, ASM, Metals Park, Ohio, 1967, p. 125
7. Schmalzreid, H. and Gerold, W., Z. Metallkrunde, 49, 291, 1958
8. Embury, J.D. and Nicholson, R.B., Acta Met., 13, 403, 1965
9. Unwin, P.N.T., Lorimer, G.W., and Nicholson, R.B., Acta Met., 17, 1363, 1969
10. Embury, J.D. and Nicholson, R.B., Acta Met., 11, 347, 1963
11. Judd, G. and Shastry, C.R., Tech. Report #1, ONR contract #N0014-67A-0117-009, 1970
12. Thomas, G. and Nutting, T., J. Inst. Metals, 88, 81, 1959-60
13. Sedricks, A.J., Slattery, P.W., and Pugh, E.N., Trans. ASM, 62, 815, 1969
14. Laird, C. and Thomas, G., Intern. J. Fracture Mech., 3, 81, 1967
15. Forsyth, P.J.E., Acta Met., 11, 703, 1963
16. Duquette, D.J. and Swann, P.R., Acta Met., 24, 241, 1976
17. DeArdo, A.J. and Townsend, R.D., Met. Trans., 1, 2573, 1970
18. Montgrain, L. and Swann, P.R., in Hydrogen in Metals, ed. Bernstein, I.M. and Thompson, A.W., ASM, 1974, pp. 575-581
19. Stubbington, C.A. and Forsyth, P.J.E., J. Inst. Metals, 90, 347, 1961
20. Grosskreutz, J.C. and Shaw, G.G., Acta Met., 20, 523, 1972
21. Bowles, C.Q. and Broek, D., Intern. J. Fracture Mech., 8, 75, 1972

22. Kelly, A., Tyson, W.R., and Cottrell, A.H., Phil. Mag., 15, 567, 1967
23. Spahn, H., in Corrosion Fatigue, ed. McEvily, A.J. and Staehle, R.W., NACE, Houston, Texas, 1972
24. Jacisin, J. M., Trans. AIME, 239, 821, 1967
25. Bradshaw, F.J. and Wheeler, C., App. Mech. Res., 5, 112, 1966
26. Wadsworth, N.J. and Hutchings, J., Phil. Mag., 3, 1154, 1958
27. Gilbert, P.T., Met. Reviews, 1, 379, 1956
28. Hartman, A., Intern. J. Fracture Mech., 1, 167, 1965
29. Broom, T., and Nicholson, A., J. Inst. Met., 89, 183, 1960-61
30. Wei, R.P. Intern. J. Fracture Mech., 4, 159, 1968
31. Oriani, R.A., and Josephic, P.H., Acta Met., 22, 1065, 1974
32. Barth, C.F. and Troiano, A.J., Corrosion, 28, 259, 1972
33. Spitzig, W.A., Talda, P.M., and Wei, R.P., Engr. Fracture Mech., 1, 155, 1968
34. Grosskreutz, J.C., Surface Sci., 8, 173, 1967
35. Head, A.K., Phil. Mag., 44, 92, 1953
36. Connors, G.H., Intern. J. Eng. Sci., 5, 25, 1967
37. Hartman, A. and Schijve, J., Engr. Fracture Mech., 1, 615, 1970
38. Bradshaw, F.J. and Wheeler, C., Intern. J. Fracture Mech., 5, 255, 1969
39. Hordon, M.J. and Wright, M.A., Trans ASM-AIME, 242, 2011, 1968
40. Pelloux, R.M.N., ASM Trans. Quarterly, 62, 1, 1969
41. Laird, C., and Smith, G.C., Phil. Mag., 8, 1945, 1963
42. Hordon, M.J., Acta Met., 14, 1173, 1966
43. Achter, M.R., Scripta Met., 2, 525, 1968
44. Smith, H.H., Shahinian, P., and Achter, M., Trans. TSM-AIME, 245, 947, 1969
45. Vedder, W. and Vermilyea, D.A., Trans. Faraday Soc., 65, 561 1969

46. Pourbaix, M., Atlas of Electrochemical Equilibria, Pergamon Press, Bristol, 1966 (translated by J. Franklin)
47. Godard, H., Jepson, W., Bothwell, M., and Kane, R., The Corrosion of Light Metals, John Wiley and Sons, New York, New York, 1967
48. Ito, G., Sawayanagi, F., and Shimiza, Y., Trans. Res. Inst. for Metals (Japan), 4, 1, 1962
49. Heine, M.A., Keir, D.S., and Pryor, M.J., J. Electrochem. Soc., 112, 24, 1965
50. Pryor, M.J., and Keir, D.S., J. Electrochem. Soc., 102, 605 1955
51. Wood, G.C., Sutton, W.H., Richardson, J.A., Riley, T., and Malherbe, A.G., Localized Corrosion, ed. Brown, B.F., Kruger, J. and Staehle, R.W., NACE, Houston, Texas, 1974, p. 526
52. Richardson, J.A., and Wood, G.C., Corrosion Sci., 10, 313, 1970
53. Pryor, M.J., Localized Corrosion, op.cit., p.2
54. Sedriks, A.J., Green, J.A.S., and Novak, D.L., Corrosion, 27, 198, 1971
55. Brown, B.F., Fujii, C.T., and Dahlberg, E.P., J. Electrochem. Soc., 116, 218, 1969
56. Johnson, W.K., Br. Corr. J., 6, 200, 1971
57. Corsetti, L. and Duquette, D.J., Met. Trans., 5, 1087, 1974
58. Swann, P.R., Localized Corrosion, op.cit., p.104
59. Dunn, C.G., Bolan, R.B., Alwan, A.S., and Stirling, A.W., J. Electrochem. Soc., 118, 381, 1971
60. Edeleanu, C., J. Inst. Metals, 89, 90, 1960-61
61. Diegle, R.B., J. Electrochem. Soc., 121, 583, 1974
62. Hunter, M.S., J. Electrochem. Soc., 117, 1215, 1970
63. Dix, E.H., Corrosion of Metals, A.S.M. (1946)
64. Dix, E.H., Trans. AIME, 137, 11, 1940
65. Sprowls, D.O. and Brown, R.H. in Fundamental Aspects of Stress Corrosion Cracking, op.cit., p. 466

66. Speidel, M.O., reported in Advances in Corrosion Science and Technology, vol. 2, Plenum Press, New York, London, 1972, p. 115
67. Lifka, B.W., unpublished work reported in ref. 59
68. Helfrich, W.J., Corrosion, 24, 423, 1968
69. Gest, R.J. and Troiano, A.R., Corrosion, 30, 274, 1974
70. Speidel, M.O. in The Theory of Stress Corrosion Cracking in Alloys, Nato Scientific Affairs Division, Brussels, 1971, p. 289
71. Donavan, J.A., Met. Trans., 7, 1677, 1976
72. Berggreen, J. and Kaesche, H., Ph.D. thesis of J. Berggreen, 1973, University of Erlangen, Nurnberg
73. Troiano, A.R., Trans. ASM, 52, 54, 1960
74. Gibala, R., Trans. Met. Soc., AIME, 239, 1574, 1967
75. Green, J.A.S., Hayden, H.W., and Montague, W.G. in Effect of Hydrogen on Behavior of Materials, ed. Bernstein, I.M. and Thompson, A.W., ASM, 1976, p. 200
76. Stubbington, C.A., Metallurgia, 65, 109, 1963
77. Forsyth, P.J.E., Stubbington, C.A., and Clark, D., J. Inst. Metals, 90, 238, 1961-62
78. Stubbington, C.A., and Forsyth, P.J.E., Acta Met., 11, 703, 1963
79. Stubbington, C.A., and Forsyth, P.J.E., Acta Met., 14, 5, 1966
80. Wanhill, Corrosion, 31, 67, 1975
81. Speidel, M.O., Blackburn, M.J., Beck, T.R., and Feeney, J.A., Corrosion Fatigue, op.cit., 324
82. Stolz, R.E. and Pelloux, R.M., Met. Trans., 3, 2433, 1972
83. Stolz, R.E. and Pelloux, R.M., Corrosion, 29, 13, 1973
84. Feeney, J.A., McMillan, J.C. and Wei, R.P., Met. Trans., 1, 1741, 1970
85. Smith, E., Jacko, R., and Duquette, D.J., Effects of Hydrogen on Behavior of Materials, op.cit., p. 213
86. Ateya, B.G. and Pickering, H.W., Hydrogen in Metals, op.cit., p. 206

87. Duquette, D.J., Ph.D. thesis, M.I.T., 1967
88. Oldham, K.B. and Mansfeld, F., Corrosion Sci., 13, 813, 1973  
3
89. Ryum, N., Acta. Met., 17, 829, 1969
90. Cottrell, A.H., Dislocations and Plastic Flow in Crystals, Oxford University Press, 1965, p. 173
91. McNeil, M.B., and Grosskreutz, J.C., Phil. Mag., 12, 1115, 1976
92. Li, J.M.C., Oriani, R.A., and Darken, L.S., Z. Phys. Chem., 49, 271, 1966
93. Oriani, R.A., and Josephie, P.H., Acta Met., 22, 1065, 1974
94. Cottrell, A.H., op.cit., p. 136
95. Tien, J.K., Effect of Hydrogen on the Behavior of Materials, op. cit., p. 309
96. Gilman, J.J., Micromechanics of Flow in Solids, McGraw Hill, New York, 1969, p. 186
97. Hordon, M.J. and Averbach, B.L., Acta Met., 9, 247, 1961
98. Kelly, A. and Nicholson, R.B., Progress in Materials Science, Pergamon Press, p. 151
99. Johnson, H.H. and Hirth, J.P., Materials Science Center, report #2565, November, 1975
100. Thompson, A.W., Effect of Hydrogen on the Behavior of Materials, op.cit., p. 467
101. Troiano, A.R., Trans. ASM, 52, 56, 1960
102. Kamdar, M.H., UCLA-ENG.-7234, April, 1972
103. Gilman, J.J., Fracture, ed. by B.L. Averbach, et.al., The Technology Press of MIT., p. 193, 1959
104. Wanhill, R.J.H., Corrosion, 10, 371, 1974
105. Burton, J.J., and Jura, G., J. Phys. Chem., 71, 1937, 1967
106. Love, A.E.H., A Treatise on the Mathematical Theory of Elasticity, Dover Publications, 1926, p. 102
107. Mangulis, Y., Handbook of Series, Academic Press, 1966, p. 82
108. Spiedel, M.O., Hydrogen in Metals, op.cit., p. 249

Appendix

Calculation of stress across the midpoint plane of a dipole array. (After McNeil and Grosskreutz) 91

Consider an infinite array of edge dislocation dipoles in the x-y plane, all dislocations being infinitely long and parallel to the z axis (a reasonable assumption, since electron microscopy observation indicates that dislocation separation is much less than their lengths). The array will consist of dislocations of Burger's Vectors  $b$  at  $y=a$ ,  $x=d-\delta \pm jc$ , for  $-\infty < j < \infty$  and dislocations with Burger's vector  $-b$  at  $y=-a$ ,  $x=d+\delta \pm jc$ ,  $-\infty < j < \infty$ . This array has been schematically illustrated in Figure 48b.

Under plane strain conditions, the cubic dilatation,  $e$ , can be expressed by:

$$e = \frac{1-\gamma}{2\gamma} (X_x + Y_y) \quad (106)$$

To evaluate this quantity along the midpoint planes of the dipoles, it is necessary to use the stress fields of the dislocations as shown by Cottrell:

$$X_x + Y_y = 2D\alpha \left[ \sum_{j=-\infty}^{\infty} \frac{1}{(d-\delta+jc)^2 + \alpha^2} + \sum_{j=-\infty}^{\infty} \frac{1}{(d+\delta+jc)^2 + \alpha^2} \right]$$

where

$$D = \frac{ub}{2\pi(1-\gamma)}$$

therefore

$$e = \frac{b\alpha}{2\pi(1-\gamma)c^2} \left[ \sum_{j=-\infty}^{\infty} \frac{1}{(j + \frac{d-\delta}{c})^2 + (\frac{a}{c})^2} + \sum_{j=-\infty}^{\infty} \frac{1}{(j + \frac{d+\delta}{c})^2 + (\frac{a}{c})^2} \right]$$

For the strain across the dipole, it is reasonable to assume that the dilatation will be predominantly elastic in character. Therefore, the normal stress across the dipole can be approximated by:

$$\sigma = Ee = \frac{Eb\alpha}{2\pi(1-\gamma)c^2} \left[ \sum_{j=-\infty}^{\infty} \frac{1}{(j + \frac{d-\delta}{c})^2 + (\frac{a}{c})^2} + \sum_{j=-\infty}^{\infty} \frac{1}{(j + \frac{d+\delta}{c})^2 + (\frac{a}{c})^2} \right]$$

The series can be summed in closed form giving:

$$\sigma = \frac{1-2r}{2(1-r)} \cdot \frac{Eb}{c} \left[ \frac{\sinh \frac{2\pi a}{c}}{\cosh \frac{2\pi a}{c} - \cos \frac{2\pi(d-s)}{c}} + \frac{\sinh \frac{2\pi a}{c}}{\cosh \frac{2\pi a}{c} - \cos \frac{2\pi(d+s)}{c}} \right]$$

Assuming the values for the 7000 series aluminum alloys, ( $E=7.27 \times 10^7 \text{ MN/m}^2$  and  $r = 1/3$ ), it is possible to evaluate the stress across the dipole array for any geometric arrangement of the individual dislocations. It should also be noted that a partial summation of the equation with as few as five dipoles yields results within a few per cent of the infinite array.

## UNCLASSIFIED

Security Classification

## DOCUMENT CONTROL DATA - R&amp;D

(Security classification of title, body of abstract and indexing annotation must be entered when the overall report is classified)

1. ORIGINATING ACTIVITY (Corporate author) Rensselaer Polytechnic Institute Materials Engineering Department Troy, New York 12181	2a. REPORT SECURITY CLASSIFICATION Unclassified
	2b. GROUP

## 3. REPORT TITLE

(6) THE CORROSION FATIGUE BEHAVIOR OF A HIGH PURITY Al-Zn-Mg-Cu ALLOY,

## 4. DESCRIPTIVE NOTES (Type of report and inclusive dates)

(9) Technical Report

## 5. AUTHOR(S) (Last name, first name, middle)

Smith, Edward F., III and Duquette

(10) Edward F. Smith, III  
D. J. Duquette

## 6. REPORT DATE

(11) November 1979

## 7a. TOTAL NO. OF PAGES

194

## 7b. NO. OF REFS

108

## 8a. CONTRACT OR GRANT NO.

(15) N00014-75-C-0466  
PROJECT NO.

## 8b. ORIGINATOR'S REPORT NUMBER(S)

(12) 206

## c.

## d.

## 10. AVAILABILITY/LIMITATION NOTICES

Distribution of this document is unlimited.

## 11. SUPPLEMENTARY NOTES

## 12. SPONSORING MILITARY ACTIVITY

OFFICE OF NAVAL RESEARCH

MN/sgm,

13. ABSTRACT The effect of hydrogen on the corrosion fatigue behavior of an Al-5Zn-2.5Mg-1.5Cu alloy was investigated. In the study, a constant mean load (207 MN/m<sup>2</sup>), S-N type test method was used to monitor the fatigue response under air and .5N NaCl environments. In both cases, specific experiments were conducted in an attempt to determine the operating failure mechanism.

In the air fatigue case, all specimens failed in a transgranular mode. The cyclic stress-strain response of the alloy indicated that the alloy hardened as the fatigue process proceeded to the crack initiation stage. TEM examination of the dislocation substructure indicated a large density of dislocation dipoles in the slip bands. These observations are consistent with debris accumulation model suggested by Duquette and Swann.<sup>16</sup> The model proposes that the accumulation of dipoles within the slip band will exert an increasing cleavage stress across the slip plane. By using a conservative estimate of the dipole density (obtained from the TEM micrographs), it is possible to show that the dipole stress may reach levels in excess of 100 MN/m<sup>2</sup>. Since this stress is thought to be additive to the applied stress levels, the model provides a plausible failure mechanism.

In addition to the laboratory air environment, tests were also performed in an aerated, .5N NaCl solution. In comparison to the air fatigue properties, the tests conducted under open circuit conditions (-.750v vs SCE) resulted in a marked decrease in the fatigue response. These failures were characterized by intergranular initiation leading to a transgranular cleavage type propagation mode. It was found that moderate polarization (to -1.3v vs SCE) produced little change in the fatigue response. Additional polarization to -1.75v vs SCE resulted in a

sgm

DD FORM 1 JAN 64 1473

(See attached sheet)

UNCLASSIFIED

Security Classification

302 125

200

Security Classification

14. KEY WORDS	LINK A		LINK B		LINK C	
	ROLE	WT	ROLE	WT	ROLE	WT
Al-Mg-Zn Alloys Fatigue Corrosion Fatigue Crack Initiation Environmental Effects						
INSTRUCTIONS						
1. ORIGINATING ACTIVITY: Enter the name and address of the contractor, subcontractor, grantees, Department of Defense activity or other organization (corporate author) issuing the report.	imposed by security classification, using standard statements such as:					
2a. REPORT SECURITY CLASSIFICATION: Enter the overall security classification of the report. Indicate whether "Restricted Data" is included. Marking is to be in accordance with appropriate security regulations.	(1) "Qualified requesters may obtain copies of this report from DDC."					
2b. GROUP: Automatic downgrading is specified in DoD Directive 5200.10 and Armed Forces Industrial Manual. Enter the group number. Also, when applicable, show that optional markings have been used for Group 3 and Group 4 as authorized.	(2) "Foreign announcement and dissemination of this report by DDC is not authorized."					
3. REPORT TITLE: Enter the complete report title in all capital letters. Titles in all cases should be unclassified. A meaningful title cannot be selected without classification; show title classification in all capitals in parentheses immediately following the title.	(3) "U. S. Government agencies may obtain copies of this report directly from DDC. Other qualified DDC users shall request through _____."					
4. DESCRIPTIVE NOTES: If appropriate, enter the type of report, e.g., interim, progress, summary, annual, or final. Give the inclusive dates when a specific reporting period is covered.	(4) "U. S. military agencies may obtain copies of this report directly from DDC. Other qualified users shall request through _____."					
5. AUTHOR(S): Enter the name(s) of author(s) as shown on or in the report. Enter last name, first name, middle initial. If military, show rank and branch of service. The name of the principal author is an absolute minimum requirement.	(5) "All distribution of this report is controlled. Qualified DDC users shall request through _____."					
6. REPORT DATE: Enter the date of the report as day, month, year; or month, year. If more than one date appears on the report, use date of publication.	If the report has been furnished to the Office of Technical Services, Department of Commerce, for sale to the public, indicate this fact and enter the price, if known.					
7a. TOTAL NUMBER OF PAGES: The total page count should follow normal pagination procedures, i.e., enter the number of pages containing information.	11. SUPPLEMENTARY NOTES: Use for additional explanatory notes.					
7b. NUMBER OF REFERENCES: Enter the total number of references cited in the report.	12. SPONSORING MILITARY ACTIVITY: Enter the name of the departmental project office or laboratory sponsoring (paying for) the research and development. Include address.					
8a. CONTRACT OR GRANT NUMBER: If appropriate, enter the applicable number of the contract or grant under which the report was written.	13. ABSTRACT: Enter an abstract giving a brief and factual summary of the document indicative of the report, even though it may also appear elsewhere in the body of the technical report. If additional space is required, a continuation sheet shall be attached.					
8b, 8c, & 8d. PROJECT NUMBER: Enter the appropriate military department identification, such as project number, subproject number, system numbers, task number, etc.	It is highly desirable that the abstract of classified reports be unclassified. Each paragraph of the abstract shall end with an indication of the military security classification of the information in the paragraph, represented as (TS), (S), (C), or (U).					
9a. ORIGINATOR'S REPORT NUMBER(S): Enter the official report number by which the document will be identified and controlled by the originating activity. This number must be unique to this report.	There is no limitation on the length of the abstract. However, the suggested length is from 150 to 225 words.					
9b. OTHER REPORT NUMBER(S): If the report has been assigned any other report numbers (either by the originator or by the sponsor), also enter this number(s).	14. KEY WORDS: Key words are technically meaningful terms or short phrases that characterize a report and may be used as index entries for cataloging the report. Key words must be selected so that no security classification is required. Identifiers, such as equipment model designation, trade name, military project code name, geographic location, may be used as key words but will be followed by an indication of technical context. The assignment of links, roles, and weights is optional.					
10. AVAILABILITY/LIMITATION NOTICES: Enter any limitations on further dissemination of the report, other than those						

DOCUMENT CONTROL DATA - R&D

Item 13. Abstract (continued)

further decrease in the fatigue strength. A comparison of the free corrosion rate with the electrochemical polarization diagram suggests that the observed embrittlement is linked to an increase in the surface hydrogen level. SEM fractographs also indicate that the degree of transgranular failure increases with both the surface hydrogen level and the applied cyclic stress.

In an effort to determine the hydrogen transport mechanism, a number of modified tensile tests were performed in the hydrogen charging environment (-1.75v vs SCE). The tests consisted of an initial macro yielding of the specimen followed by a stress relaxation period and a subsequent re-yielding. It was found that the specimens which failed transgranularly also demonstrated a serrated yielding behavior during the re-yielding process. This phenomenon indicated that hydrogen could be transported in the solute atmosphere of a dislocation.

These results indicated that the observed fatigue behavior could be explained by a hydrogen embrittlement mechanism. A model is developed which demonstrates quantitative agreement between the observed fracture morphology and the calculated dislocation transport efficiency. For low efficiency conditions, the observed fracture mode is thought to be hydrogen induced grain boundary separation. As the efficiency increases, the grain boundaries are depleted of hydrogen and the crack propagates along the embrittled transgranular path.